Ultra Low Noise Microwave Dielectric Oscillators at 3.8GHz and 10GHz and High Q Tunable Bragg Resonators

Pratik Dilip Deshpande

PhD

University of York
Electronics

November 2015

ABSTRACT

The thesis is divided into three parts. The first part of the thesis describes the design and development of two prototypes of an ultra-low phase noise 3.8GHz dielectric resonator oscillator. The first prototype included vibration measurements with a reasonable phase noise measurements developed for Selex-ES. The phase noise for the first 3.8GHz oscillator is -117 dBc/Hz at 1kHz offset and -150 dBc/Hz at 10kHz offset. The second prototype was the improved modular yet compact oscillator was then developed which demonstrated a significantly improved phase noise performance of -125.6 dBc/Hz at 1kHz offset and -153 dBc/Hz at 10kHz offset which is the lowest noise reported in the literature in this frequency band using a ceramic dielectric resonator.

In the second part of the thesis, a design and measurement of a high Q broad tuning aperiodic Bragg resonator operating at 10GHz is described. The resonator utilises an aperiodic arrangement of non ($\lambda_g/4$) low loss alumina plates ($\mathcal{E}_r$=9.75, loss tangent of ~1 to 2×10^{-5}) mounted in a cylindrical metal waveguide. The insertion loss, S_{21}, varied from -3.9 dB to -6.4 dB while the unloaded Q varies from 81,650 to 61,020 over the tuning range of 100MHz (1%).

In the third part of the thesis, simulation, design and measurement of a low noise Bragg resonator oscillator operating at 10GHz is presented. The oscillators demonstrated a phase noise of -153 dBc/Hz at 10kHz offset and -123 dBc/Hz at 1kHz offset for an unloaded Q of 190,000. To achieve these results extensive optimization of different transistors with different power level and noise figure has taken place.

TABLE OF CONTENTS

LIST OF FIGURES

LIST OF TABLES

ACKNOWLEDGEMENTS

I would like to thank my supervisor, Professor Jeremy Everard for his continuous support and the constructive feedback he has given me during my PhD. I would also like to thank him for proof reading my thesis.

I would like to thanks Selex-ES for funding my PhD and in particular thank Neil Raphael and Robin Collings for help with the vibration measurements and also John Robertson for help with the initial project.

I would like to thank Dr.Simon Bale for his support and encouragement during my research and also for all the long and fruitful discussions on various topics all these years.

I would like to thank the technicians especially Mark Hough, Andy White and Pete Turner for their help of the construction of PCB boards and mechanical enclosures that required for the research.

I would like to take the opportunity to thank my friends to those especially in York; Anna Ladi, Evangelia Karadimou and Tsvetan Burtichelov for all the fun times we shared. I would also take the opportunity to thank my friends Rashmi Patil and Vinnay Mayya for all their unconditional friendship.

Last but not the least; I thank my parents Dilip Deshpande and Deepti Deshpande who supported me in every decision of my life and who have always given me their unconditional love and support. I would also like to thank my sister Preeti N. Joshi and my brother in law Nikhil Joshi for constant support.

DECLARATION

First prototype of the 3.8GHz oscillator: This work was managed within the framework of the ITP SIMCLAIRS program. France, United Kingdom and Sweden mandated the European Defence Agency (EDA) to contract the Project with a Consortium composed of THALES SYSTEMES AEROPORTES France, acting as the Consortium Leader, Selex ES Ltd, THALES UK Ltd and SAAB AB.

This work has not previously been presented for an award at this, or any other, University. I declare that this thesis is the result of my own work. References and acknowledgements to other authors have been given where appropriate. The following publications have resulted as part of this work:

JOURNAL PUBLICATIONS

1. Bale, Simon J.; Hough, Deshpande, Pratik D; Mark; Everard, Jeremy, "Highly tunable X-band Bragg resonator at 10 GHz for oscillator applications" IEEE-UFFC *(Accepted)*

CONFERENCE PUBLICATIONS

1. P. D. Deshpande and J. Everard, "Compact low phase noise 3.8 GHz oscillator," *European Frequency and Time Forum (EFTF), 2014*, Neuchatel, 2014, pp. 203-207. (Best Student Paper).
2. Deshpande, Pratik D; Bale, Simon J.; Hough, Mark; Everard, Jeremy, "Highly tunable X-band Bragg resonator - initial results," *Frequency Control Symposium & the European Frequency and Time Forum (FCS), 2015 Joint Conference of the IEEE International*, vol., no., pp.423,426, 12-16 April 2015.
3. Deshpande, Pratik D; Bale, Simon, J; Everard, Jeremy "Low Phase Noise 10GHz Bragg Resonator Oscillator", 30th European Frequency and Time Forum, York, April 2016 *(Accepted)*

CHAPTER 1

INTRODUCTION

1.1 Background

Oscillators play a very important role in any communication device for example in mobile phones, satellite systems or instrumentations system. For instance, in the receiver chain of a communication system, after the signal is amplified with the help of a low noise amplifier, it is down converted with a mixer and a local oscillator to produce an intermediate frequency which is then used for modulation and demodulation [1]. If the phase noise of this oscillator is large, it might actually mask the required signal which is then a problem during digital processing. Similarly, in the case of a RADAR System, the oscillator performance is very critical where the phase noise that is close to the carrier might partially or completely mask the target signal which is being measured [2] [3] [4]. In the case of a digital system, any noise generated by the oscillator will result in an increased bit error rate of the system, which is a problem during the modulation and demodulations process. Also, the phase noise in a frequency multiplication process gets increased by a factor of $20\log_{10}(N)$ dB [5], where N is the multiplication factor. So for example, if a 1GHz oscillator that has a noise floor of -170 dBc/Hz at large frequency offsets, when

multiplied by a factor of 10 to produce a 10GHz output signal, the system noise floor gets increased by 20dB, resulting in a noise floor of -150 dBc/Hz at 10GHz which is quite high when compared to sapphire dielectric resonator oscillators present in the literature [6]. Hence, in most cases, oscillators set the ultimate performance of the system in any communication device [7].

One of the main characteristic of an oscillator is its frequency stability [8] [9]. This can be divided into long term instability, which is the gradual drift of the frequency due to ageing which changes in the bias point of the amplifier as a result of fluctuations in the operating points. Ageing might also degrade the quality factor of the resonator and hence the phase noise of the oscillator. The other type of instability is referred to be as short term instability that occurs due to noise fluctuations within the oscillator which modulates the amplitude and phase. In many oscillators, the amplitude noise fluctuations are greatly supressed by the active element, since under oscillating conditions, the amplifier operates mainly in the saturation region. Hence, phase noise is the crucial factor which determines the purity of the oscillator. Initially, a model for the feedback oscillator was suggested by Leeson [10] where he states that within the 3dB bandwidth of the resonator, the amplifier phase noise gets multiplied by factor of $(1/\Delta f^2)$ and goes on to show that the phase noise is inversely proportional to the unloaded quality factor of the resonator. Later, Everard proposed a model [11] which incorporated the circulating power, the loaded quality factor and the input and the output impedances of the amplifier and demonstrates that there is an optimal resonator insertion loss to achieve minimum phase noise of the oscillators.

Also, RF systems which are designed in satellite or wireless systems for a particular frequency band unlike a cell phone which is manufactured to work at

multiple frequency bands. Hence to maximize the availability of the frequency spectrum, tunable resonators are mainly used in such systems as local tunable oscillators in front end of the receivers [12]. This is an ideal solution to reduce the hardware costs by incorporating a single local oscillator which can be used at multiple frequency bands. High Q tunable resonators can also be used as filters to suppress any interfering signals or harmonics that can be generated by power amplifiers. The dielectric resonator architecture usually offers high Q factors, controllable temperature coefficient and are less sensitive to vibrations. Their power handling capability ensures low phase noise close and far away from the carrier at microwave frequencies. One of the main criteria for such filters to be used in receiver systems is to have a low insertion loss since the noise figure of such filters might add up in the receiver chain if they are in the front end. They also need to have high Q when used in an oscillator to enhance the performance of the device and remove any harmonics or any spurious frequencies when used as a filter. They need to have a reasonable tuning range with good power handling capability and high linearity at microwave frequencies [12] [13].

1.2 Thesis objective

The main aim of this thesis is to develop compact, low cost, ultra-low noise oscillators and high Q tunable resonators for oscillator applications at microwave frequencies. Ultra-low noise oscillators are implemented by designing, testing and optimising various elements such as amplifiers, electronic phase shifter, coupler and resonator in a feedback topology oscillator at 3.8GHz and 10GHz. High Q tunable resonators are investigated with existing high Q resonators available at 10GHz which can be

tuned for a certain range without severely degrading the quality factor. The main topics of research undertaken in this area are:

- **Ultra-low noise oscillators:**

Amplifiers: Various amplifiers were investigated for high power levels and low noise which exhibit low flicker noise corners for different amplifier topologies which includes amplifiers in single stage, cascaded and amplifiers in a push pull configuration. Residual noise measurements were done on various types of transistors to determine the flicker noise corners.

Phase Shifter: Design of electronic phase shifters which exhibits low insertion loss with a reasonable phase shift for the required frequency of operation was investigated and non-linear effects of the phase shifter at high power levels were also investigated.

Resonator: High Q resonators play a very important role in determining the phase noise of the oscillator and hence simulations, experiments and experiments were conducted in order to optimise the quality factor of the resonator along with the insertion loss to achieve optimum phase noise for the oscillators. Printed circular probes were developed which enabled high Q resonator design in a compact layout.

In addition, investigations into multi section couplers for the 3.8GHz oscillator along with a compact mechanical phase shifter were undertaken. The single layer coupler and the mechanical phase shifter were designed to have a low insertion loss.

Finally, oscillators were built using these optimised elements in a feedback topology to demonstrate the phase noise which were within 3-4dB of the phase noise theory given by Everard [11].

- **Tunable Resonators:** The main objective was to design and construct a high Q tunable resonator with a maximum spurious free tuning range with a low insertion loss which could be used for oscillator applications at 10GHz. Resonator was modelled using ABCD matrix and was simulated in order to predict the tuning range and the unloaded Q of the resonator. Simulations predict a tuning range of 10% without much degradation of Q for Bragg resonators at 10GHz.

1.3 Thesis Structure

The thesis is organised as follows:

Chapter 2 begins with the basics of the theory for a feedback oscillator and phase noise for oscillators. This is followed by an analytical linear phase noise model described by J.K.A.Everard [11] which consists of a set of equations describing the parameters which affect the phase noise in an oscillator. In the final part, a brief introduction on environmental noise which affects the phase noise and a review of the vibration measurements done on the oscillators using a dielectric resonator as the frequency selective element has been discussed.

Chapter 3 presents the design and measurement of a low cost compact 3.8GHz microwave oscillators using a dielectric resonator. In the first part of the chapter, a review of previous oscillators with dielectric resonators and sapphire resonators operating around 4GHz has been presented. This is followed by the design of the feedback topology oscillator which was built for Selex-ES which includes the simulations and measurements of various components used in the feedback oscillator. In the next part, the vibration measurement setup which was used to

perform vibration measurements for this oscillator prototype has been discussed followed by the results and the discussions.

In the final part of the chapter, a prototype was built at the University of York to improve the phase noise of the oscillator; the new improved oscillator was produced in a modular form to enable optimisation of the individual oscillator elements. A new design for the electronic phase shifter has been described for better power handling conditions which improves the linearity of the device. Finally, phase noise of these amplifiers was measured in order to determine the flicker noise corner using a cross correlation residual phase noise measurement system which demonstrated a phase noise floor of -200dBc/Hz recently [14].

Chapter 4 begins with an introduction to tunable resonators followed by a review of various tunable resonators and tuning elements described in the literature. This is followed by a comparison of the best performance that was achieved in this work with that of various other tunable resonators in the literature with tuning range and the unloaded Q as the main criteria in determining the performance. In the next section, the theory of Bragg resonator is discussed which includes the models of the resonator using ABCD matrices. This is followed by the construction of the cavity and various steps and experiments made on the solder temperatures in the process. Finally, measurements and discussions on the tuning range and quality factor that were made on various prototypes built in this research are discussed.

Chapter 5 starts with a brief introduction to the X band oscillators followed by a review of previous X band oscillators that have used various types of resonators such as sapphire and alumina for different modes of operation. In the next part of the chapter, a Bragg resonator which demonstrated an unloaded Q

of 200,000 at 10 GHz was used as the frequency selective element in an oscillator [15]. Two of such resonators were built and optimised to have the correct insertion loss and the loaded Q. This is followed by testing a number of active devices in the oscillator. A number of Silicon germanium (SiGe) and heterojunction bipolar transistor (HBTs) amplifiers have been designed to determine the gain, noise figure (NF), output compression and flicker noise corners. Also, for each given amplifier, the predicted theoretical phase noise at 1kHz and 10kHz has been given. Based on this, the active element for the oscillator was chosen. Different configurations have been used to determine the highest output power and low flicker noise corners. In the final part of the chapter, phase noise measurements have been shown with a comparison with the theory followed by conclusions.

Chapter 6 provides the main conclusions of the research work followed by the future areas of research suggested for each of the topics described in the thesis.

CHAPTER 2

OSCILLATORS AND PHASE NOISE

2.1 Feedback Oscillators

The simplest way to produce an oscillation is by combining an amplifier along with the frequency element such as a resonator to make a feedback oscillator as shown in **Figure 2.1**.

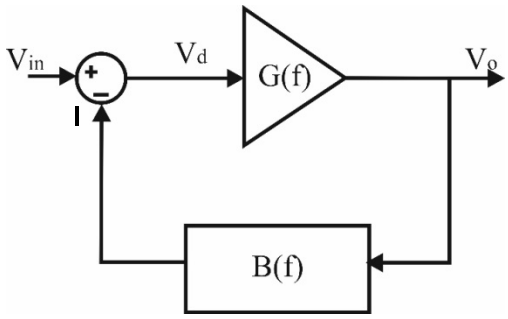

Figure 2.1: Simplified positive feedback oscillator.

Now applying loop voltage equations to the above circuit we get:

$$V_o = G(f)V_d \qquad \textbf{Eq. 2.1}$$

$$V_d = V_{in} - V_o B(f) \qquad \textbf{Eq. 2.2}$$

Rearranging the above equations, the ratio of $\left(\frac{V_o}{V_{in}}\right)$ we get:

$$\left(\frac{V_o}{V_{in}}\right) = \frac{G(f)}{1 - [B(f)G(f)]}$$
$$V_o = \left(\frac{G(f)}{1 - [B(f)G(f)]}\right) V_{in} \qquad \textbf{Eq. 2.3}$$

In order for a stable oscillation to take place, as seen in **Eq. 2.3**, there should be an output voltage even if there is no input present and this can only take place if the loop gain i.e [B(f)G(f)] becomes to unity at a particular frequency which is the Barkhausen criteria [16]:

$$|B(f)G(f)| = 1 \qquad \textbf{Eq. 2.4}$$

$$Arg[B(f)G(f)] = 2\pi N \ \ where\ N = 0,1,2\ldots. \qquad \textbf{Eq. 2.5}$$

The first condition is that, the gain of the amplifier *G(f)* should be sufficient enough to cancel the losses from the feedback element *B(f)* and the open loop phase shift should be an integral of *2πN*. Also, in order for the oscillation to start, thermal noise usually disturbs the initial disturbance in the feedback loop, the loop gain is greater than one and eventually, the gain saturates and the loop gain becomes unity and a more stable oscillation is produced.

2.2 Oscillator characteristics

In an ideal world, the oscillator would produce an output signal where its energy is confined to one single frequency. The frequency spectrum of such a signal is shown in **Figure 2.2** where it consists of one single tone with a single discrete line and infinitely small bandwidth with no harmonics centered at required frequency, f_o. The ideal output voltage can be shown as:

$$V_o = A\cos(2\pi f_o t) \qquad \textbf{Eq. 2.6}$$

Where A is the amplitude and f_o is the operating frequency.

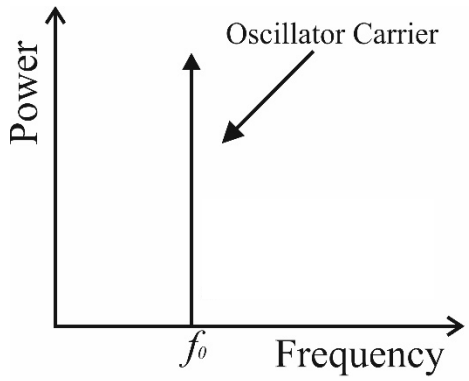

Figure 2.2: Spectrum of an ideal oscillator.

But in real world communication devices, signals are corrupt which means that they are noisy and apart from the desired signal, the spectrum consists of harmonics as shown in **Figure 2.3**. The noise side bands are due to random amplitude and phase fluctuations which occur inside the oscillator loop.

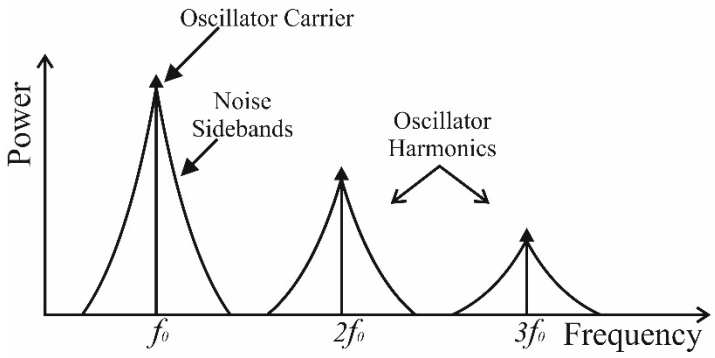

Figure 2.3: Typical spectrum of the oscillator with frequency harmonics.

2.3 Oscillator Phase Noise

The frequency stability of the oscillator is divided into two categories namely long term stability and short term stability [9]. Long term instabilities are slow changes that take place over years and gradually change the frequency of operation due to ageing. Temperature is one of the main causes for long term instability which mainly affects the operating conditions of the oscillator and particularly the resonator which affects the oscillator frequency. Short term instability is mainly due to noisy signals that arise within the system and change the phase and amplitude of the signals. The output of a noisy oscillator signal can be defined as seen in **Eq. 2.7**:

$$V_o(t) = A\big(1 + \alpha(t)\big)[Cos(2\pi f_c t + \phi(t)] \qquad \textbf{Eq. 2.7}$$

Where $\alpha(t)$ is the amplitude fluctuation (AM noise) and $\varphi(t)$ is the phase fluctuations that take place as a function of time (PM noise). However, in an saturating amplifier used in oscillator, the amplitude noise is greatly suppressed by the limiting characteristics of the amplifier and hence $\alpha(t) \rightarrow 0$. Now if we assume $\varphi(t) \ll 1$, then any small change in instantaneous frequency by frequency modulation of the phase term we get **Eq. 2.8** and substituting **Eq. 2.8** in **Eq. 2.7** and using the trigonometric series we get **Eq. 2.9**.

$$\phi(t) = \phi_p sin(2\pi f_m t) \qquad \textbf{Eq. 2.8}$$

$$V_o(t) = A\big[cos(2\pi f_c t).cos\big(\phi_p sin(2\pi f_m t)\big) - sin(2\pi f_c t).sin\big(\phi_p sin(2\pi f_m t)\big)\big] \qquad \textbf{Eq. 2.9}$$

For $x \ll 1$; $cos(x) \simeq 1$ and $sin(x) \simeq x$. Hence the output voltage is given by **Eq. 2.10**.

$$V_o(t) = A\big[cos(2\pi f_c t) - sin(2\pi f_c t).\phi_p sin(2\pi f_m t)\big] \qquad \textbf{Eq. 2.10}$$

Using the trigonometry identity: $\sin\alpha\,.\sin\beta = \frac{1}{2}[\cos(\alpha-\beta)-\cos(\alpha+\beta)]$ and substituting it in **Eq. 2.11**.

$$V_o(t) = A\left[cos(2\pi f_c t) - \frac{\phi_p}{2}cos(2\pi(f_c - f_m)t) - \frac{\phi_p}{2}cos(2\pi(f_c + f_m)t)\right] \quad \textbf{Eq. 2.11}$$

This shows that any small changes in the phase or frequency cause side band modulation at frequencies $f_c \pm f_m$ and these are referred to as the phase noise of an oscillator which is defined as the ratio of the single sideband phase noise power at a given offset in a 1Hz bandwidth to the total carrier power and is usually expressed as dBc/Hz as shown in **Figure 2.4** where P_n is the total power of the carrier plus the power in the sidebands of the oscillator.

$$L(f) = \frac{Single\ sideband\ phase\ noise\ power\ at\ a\ given\ offset\ in\ a\ 1Hz\ bandwidth}{Total\ carrier\ power} \quad \textbf{Eq. 2.12}$$

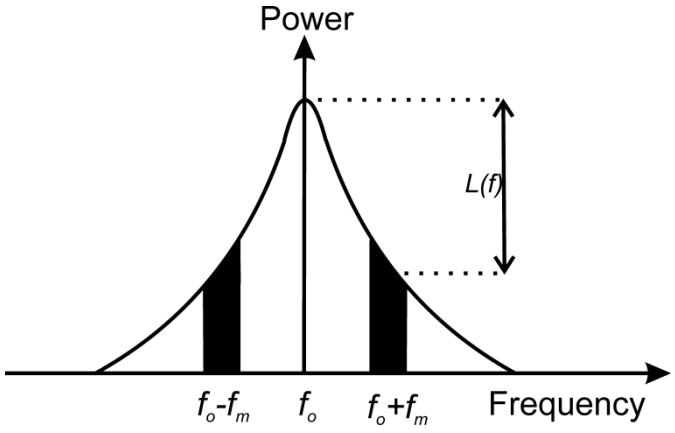

Figure 2.4: Representation of the phase noise diagrammatically.

$$L(f) = \frac{P_n}{P_c} = \frac{\frac{1}{2}\left(\frac{A\phi_p}{2}\right)^2}{\frac{1}{2}(A)^2} = \frac{{\phi_p}^2}{4} = \frac{{\phi_{rms}}^2}{2} = P_\phi(f_m) \quad \textbf{Eq. 2.13}$$

Where $\varphi_{rms}=\varphi(t)_p/\sqrt{2}$ and since the normalized power spectral density $P_\phi(f_m)$ is symmetrical about the carrier frequency, the double side band noise power $S_\phi(f_m)$ is given by **Eq. 2.14** and **Eq. 2.15**:

$$S_\phi(f_m) = 2P_\phi(f_m) \qquad \textbf{Eq. 2.14}$$

$$L(f_m) = \frac{1}{2}S_\phi(f_m) \qquad \textbf{Eq. 2.15}$$

The phase noise of an oscillator can be broadly divided into additive noise in which the noise sidebands are present independent of the carrier such as the white noise and parametric noise where the noise sidebands are proportional to the carrier such as the flicker noise. There are several types of noise which result in phase noise such as thermal noise, shot noise and flicker noise. These are now described below:

2.3.1 Thermal Noise

Thermal noise is due to the thermal vibrations of the charge carriers within a conductor. The RMS thermal noise voltage for a given bandwidth B(Hz) and resistance (Ω) is given by **Eq. 2.16**:

$$e_n = \sqrt{\frac{4hf\ BR}{e^{hf/kT} - 1}} \qquad \textbf{Eq. 2.16}$$

Where k is the Boltzman's constant ($1.38\text{x}10^{-23}$ J/K), h is Planck's constant ($6.626\text{x}10^{-34}$ J/Sec) and T is the ambient temperature. At microwave frequencies, $hf \ll kT$, hence this equation reduces to $\left[e^{hf/kT} - 1\right] = \left(hf/kT\right)$ and hence **Eq. 2.16** reduces to **Eq. 2.17** [17]:

$$e_n = \sqrt{4kTBR(\Delta f)} \qquad \textbf{Eq. 2.17}$$

This can be modelled as a noiseless resistor with a voltage source as shown in **Figure 2.5**. From **Eq. 2.17** it can be seen that the resistance changes with the frequency and hence thermal noise voltage is dependent on the frequency and if the

Δf is infinity, the thermal noise tends to be very large and for smaller bandwidths the noise is low. Also from **Eq. 2.17** it can be seen that, at lower temperatures, the noise generated is low and therefore cooler devices and components generate lower noise.

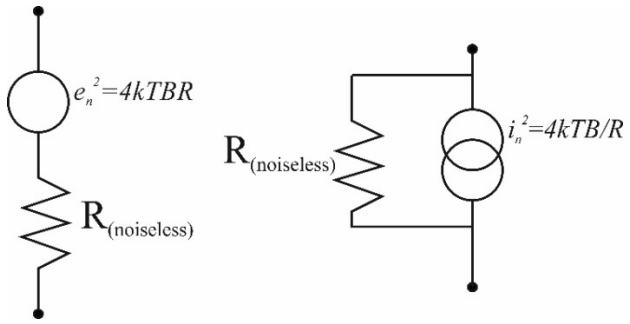

Figure 2.5: Thevenin circuit for a noisy resistor.

The noisy resistor can be modelled into a Thevenin equivalent circuit where the maximum power delivered to the load for a given bandwidth is shown in **Eq. 2.18**:

$$P_n = \left(\frac{e_n}{2R}\right)^2 R = kTB \qquad \textbf{Eq. 2.18}$$

2.3.2 Shot Noise

Shot noise exists when a DC current is applied to a semiconductor device. Current flows randomly in a device and hence this causes random fluctuation of the charge carriers (electrons and holes) and this only exists under a DC current flow unlike the thermal noise [18]. The power density of shot noise is given by **Eq. 2.19**:

$$i_n^2 = 2qI_{DC} \qquad \textbf{Eq. 2.19}$$

Where q is the charge on an electron and I_{DC} is the DC current flowing through the device. In a SiGe BJT device, the primary source of shot noise is I_C and I_B and thermal noise is generated by the base resistor r_b as shown in **Figure 2.6** [19].

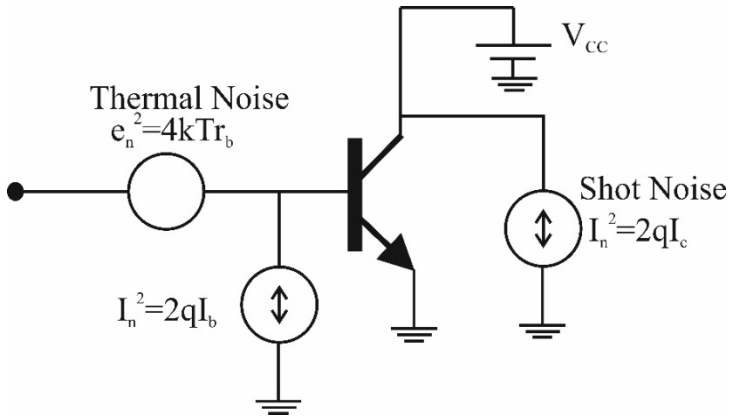

Figure 2.6: Noise model of the silicon bipolar transistor.

2.3.3 Flicker Noise

It was observed that when current passes through a semiconductor device, apart from thermal noise and shot noise, there exists excess noise which is dependent on the frequency which is referred to as flicker noise. It has a spectral density approximately of *(1/f)* at lower frequencies and at higher frequencies the noise is limited by thermal noise as shown in **Figure 2.7**. The origins of this flicker noise are not clearly understood however it is present in all semiconductor devices carrying a current [20]. These noise sources produce residual noise. The point at which the *(1/f)* and the thermal noise floor intersect is usually referred as flicker noise corner (f_c) and this corner frequency is power dependent. Based on measurements made by Hooge [16], the flicker noise power spectral density is given by **Eq. 2.20**:

$$S(f) = \sum_{n=0}^{4} b_{-n} f^{-n} \qquad \textbf{Eq. 2.20}$$

where b_{-n} are constants. The white phase noise is given by **Eq. 2.21**:

$$b_o = \frac{FkT_o}{P_{in}} \qquad \textbf{Eq. 2.21}$$

where b_o is a white phase noise coefficient constant and the *(1/f)* noise is given by $b_{-1}f^{1}$ which is phase flicker coefficient is independent of power but f_c is dependent on power as shown in **Eq. 2.22**.

$$f_c = \frac{b_{-1}P_{in}}{FkT_o} \qquad \textbf{Eq. 2.22}$$

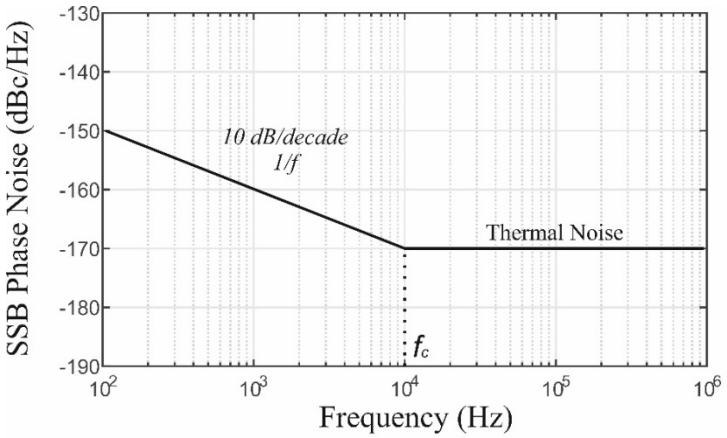

Figure 2.7: Residual phase noise plot of a typical amplifier using a silicon bipolar transistor with a flicker noise corner of 10kHz.

In amplifiers, the flicker noise is up converted onto the carrier and the spectral density of the amplifier noise is given by **Eq. 2.23**:

$$S_a(f) = \frac{FkT_o}{P_{in}}\left(1 + \frac{f_c}{\Delta f}\right) \qquad \textbf{Eq. 2.23}$$

2.3.4 Everard's Phase Noise Model

In this section, a linear theory for the phase noise of the oscillator has been described by J.K.A Everard and is fully presented in [11]. In this theory, a full analytical model for the oscillator has been described with a set of phase noise equations which incorporates all the major factors affecting the phase noise in an oscillator. The equivalent circuit of the oscillator model that can be used to model the phase noise for a feedback oscillator is shown in **Figure 2.8** where the model consists of an amplifier and a series resonator circuit. The input to the amplifier is split into two with equal impedances (R_{IN}), where the first input (V_{IN1}) is used to model the feedback loop whereas the second input (V_{IN2}) is used to model the noise. These inputs are added together and amplified to produce a single output signal, V_{OUT} with an output impedance of R_{OUT}.

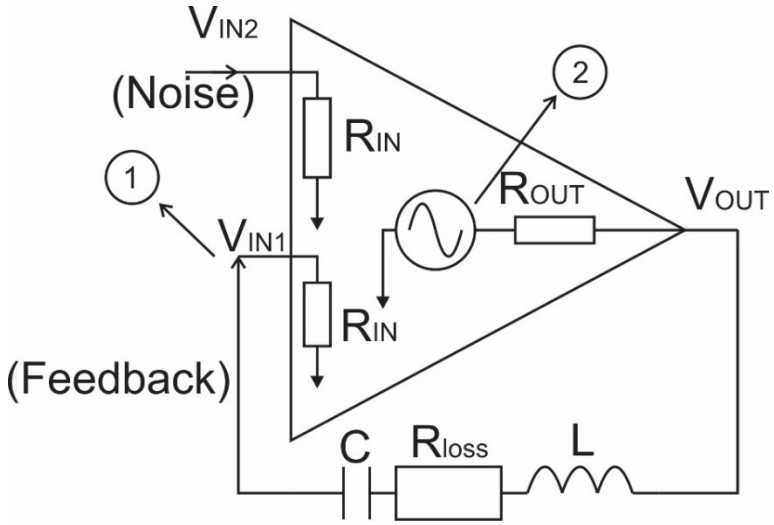

Figure 2.8: Equivalent circuit of the feedback oscillator.

Now the circuit can be analysed with injecting some white noise in the noise input (V_{IN2}) and the voltage transfer function for the model can be written as:

$$V_{OUT} = G(V_{IN1} + V_{IN2}) = G(V_{IN2} + \beta V_{OUT}) \quad \textbf{Eq. 2.24}$$

Eq. 2.24 which can be manipulated to be shown in **Eq. 2.25**.

$$\frac{V_{OUT}}{V_{IN2}} = \frac{G}{1 - (G\beta)} \quad \textbf{Eq. 2.25}$$

Where G is the voltage gain of the amplifier and β is the voltage feedback coefficient given by **Eq. 2.26**:

$$\beta = \frac{R_{IN}}{R_{LOSS} + R_{OUT} + R_{IN} + j(\omega L - 1/\omega C)} \quad \textbf{Eq. 2.26}$$

Now, if we assume ($\Delta\omega = \omega_0 \pm \omega$) and $\Delta\omega \ll \omega_0$ (where $\Delta\omega$ is the offset angular frequency from the centre angular frequency, ω_0), then as **Eq. 2.27**:

$$(\Delta\omega L - 1/\Delta\omega C) \cong \pm 2\Delta\omega L \quad \textbf{Eq. 2.27}$$

The loaded Q (Q_L) is given by **Eq. 2.28** and by rearranging the terms; the voltage transfer function is given by **Eq. 2.29**.

$$Q_L = \omega_O L/(R_{LOSS} + R_{IN} + R_{OUT}) \quad \textbf{Eq. 2.28}$$

$$\beta = \frac{R_{IN}}{(R_{LOSS} + R_{IN} + R_{OUT})\left(1 \pm 2jQ_L\frac{\Delta\omega}{\omega_0}\right)} \quad \textbf{Eq. 2.29}$$

The unloaded Q (Q_0) of the resonator is given by **Eq. 2.30**.

$$Q_O = \frac{\omega_O L}{R_{LOSS}} \quad \textbf{Eq. 2.30}$$

The ratio of the loaded Q and the unloaded Q is given by **Eq. 2.31** which is obtained by using **Eq. 2.28** and **Eq. 2.30**.

$$\left(\frac{Q_L}{Q_O}\right) = \frac{R_{LOSS}}{(R_{OUT} + R_{LOSS} + R_{IN})} \quad \textbf{Eq. 2.31}$$

Eq. 2.31 can be arranged as:

$$\left(1 - \frac{Q_L}{Q_O}\right) = \left(\frac{R_{OUT} + R_{IN}}{R_{OUT} + R_{LOSS} + R_{IN}}\right) \quad \textbf{Eq. 2.32}$$

At resonance, the imaginary parts of the terms in **Eq. 2.26** and **Eq. 2.29** are zero and hence the feedback coefficient at resonance, β_0, between nodes 1 and 2:

$$\beta_0 = \left(\frac{R_{IN}}{R_{OUT} + R_{LOSS} + R_{IN}}\right) = \left(1 - \frac{Q_L}{Q_O}\right)\left(\frac{R_{IN}}{R_{IN} + R_{OUT}}\right) \qquad \textbf{Eq. 2.33}$$

Therefore the resonator response is given by **Eq. 2.34**:

$$\beta = \left(1 - \frac{Q_L}{Q_O}\right)\left(\frac{R_{IN}}{R_{IN} + R_{OUT}}\right)\left(\frac{1}{1 \pm 2jQ_L\frac{\Delta f}{f_o}}\right) \qquad \textbf{Eq. 2.34}$$

Where f_0 is now the centre frequency and Δf is the offset frequency from the carrier now in Hertz. Hence the voltage transfer function is given by **Eq. 2.35** which is obtained by substituting **Eq. 2.34** in **Eq. 2.25**.

$$\frac{V_{OUT}}{V_{IN2}} = \frac{G}{1 - \left(\frac{G\left(1 - \frac{Q_L}{Q_O}\right)\left(\frac{R_{IN}}{R_{IN} + R_{OUT}}\right)}{\left(1 \pm 2jQ_L\frac{\Delta f}{f_o}\right)}\right)} \qquad \textbf{Eq. 2.35}$$

Now at resonance, Δf is zero, $\frac{V_{OUT}}{V_{IN2}}$ is very large and the denominator is approximately equal to zero and since $G\beta_0$=1, we therefore get **Eq. 2.36** which basically means that at resonance, the gain of the amplifier is equal to the loss in the resonator.

$$G = \frac{1}{\left(1 - \frac{Q_L}{Q_O}\right)\left(\frac{R_{IN}}{R_{IN} + R_{OUT}}\right)} \qquad \textbf{Eq. 2.36}$$

Substituting **Eq. 2.36** in **Eq. 2.35** and rearranging we get:

$$\frac{V_{OUT}}{V_{IN2}} = \frac{G}{1 - \frac{1}{\left(1 \pm 2jQ_L\frac{\Delta f}{f_o}\right)}}$$

$$= \frac{1}{\left(1 - \frac{Q_L}{Q_O}\right)\left(\frac{R_{IN}}{R_{IN} + R_{OUT}}\right)\left(1 - \frac{1}{\left(1 \pm 2jQ_L\frac{\Delta f}{f_o}\right)}\right)} \qquad \textbf{Eq. 2.37}$$

For close to carrier noise, $Q_L \frac{\Delta f}{f_o} \ll 1$, the transfer function in **Eq. 2.37** simplifies to:

$$\frac{V_{OUT}}{V_{IN2}} = \left(\frac{G}{\pm 2jQ_L \frac{\Delta f}{f_o}} \right) = \frac{1}{\left(1 - \frac{Q_L}{Q_O}\right)\left(\frac{R_{IN}}{R_{IN} + R_{OUT}}\right)\left(\pm 2jQ_L \frac{\Delta f}{f_o}\right)} \quad \textbf{Eq. 2.38}$$

The oscillator noise is quoted in terms of phase noise *L(f),* which is defined as the ratio of the noise power in a 1Hz bandwidth at an offset Δf from the carrier to the total power in the carrier. Then the phase noise is calculated by converting the voltage transfer function which is proportional to power, which is the power dissipated in the oscillating system and not in the load. The input noise power in a 1Hz bandwidth with a noise figure of F is given by **Eq. 2.39** where kT is the noise power available if the input and the source impedances were equal to R_{IN}.

$$V_{IN}^2(\Delta f) = FKTR_{IN} \quad \textbf{Eq. 2.39}$$

In this case, the noise of interest lies within the bandwidth of the resonator since the sideband noise power reaches the background level by the 3dB point of the resonator and hence the tuned circuit can be represented as a resistor for the close to carrier performance. Now using **Eq. 2.39** and **Eq. 2.38**, an expression for $(V_{OUT})^2 \Delta f$ can be obtained:

$$V_{OUT}^2(\Delta f) = \frac{FkTR_{IN}}{4\,(Q_L)^2 \left(\frac{R_{IN}}{R_{IN} + R_{OUT}}\right)^2 \left(1 - \frac{Q_L}{Q_0}\right)^2} \left(\frac{f_0}{\Delta f}\right)^2 \quad \textbf{Eq. 2.40}$$

Eq. 2.40 can be written in terms of $\frac{Q_L}{Q_0}$ to give:

$$V_{OUT}^2(\Delta f) = \frac{FkTR_{IN}}{4\,(Q_0)^2 \left(\frac{Q_L}{Q_0}\right)^2 \left(\frac{R_{IN}}{R_{IN} + R_{OUT}}\right)^2 \left(1 - \frac{Q_L}{Q_0}\right)^2} \left(\frac{f_0}{\Delta f}\right)^2 \quad \textbf{Eq. 2.41}$$

As the theory described is linear, we can incorporate the non-linearity introduced by the amplifier by modifying the absolute noise in **Eq. 2.41**. Since the amplifier operates in saturation, the amplitude noise of the oscillator gets supressed and the phase noise is halved. If the total output voltage is $V_{OUTMAXRMS}$, then the phase noise is given by:

$$V_{OUT}^2(\Delta f) = \frac{FkTR_{IN}}{8\,(Q_0)^2\left(\frac{Q_L}{Q_0}\right)^2\left(\frac{R_{IN}}{R_{IN}+R_{OUT}}\right)^2\left(1-\frac{Q_L}{Q_0}\right)^2}\left(\frac{f_0}{\Delta f}\right)^2 \qquad \textbf{Eq. 2.42}$$

Now, the phase noise is defined as:

$$L(f) = \left(\frac{V_{OUT}^2(\Delta f)}{V_{OUTMAXRMS}^2}\right) \qquad \textbf{Eq. 2.43}$$

Now substituting **Eq. 2.42** in **Eq. 2.43** we get:

$$L(f) = \frac{FkTR_{IN}}{8\,(Q_0)^2\left(\frac{Q_L}{Q_0}\right)^2\left(\frac{R_{IN}}{R_{IN}+R_{OUT}}\right)^2\left(1-\frac{Q_L}{Q_0}\right)^2 V_{OUTMAXRMS}^2}\left(\frac{f_0}{\Delta f}\right)^2 \qquad \textbf{Eq. 2.44}$$

If we define the power available at the output of the amplifier into a matched load as P_{AVO}, then

$$P_{AVO} = \frac{V_{OUTMAXRMS}^2}{4R_{OUT}} \qquad \textbf{Eq. 2.45}$$

Now substituting this in **Eq. 2.44** we get:

$$L(f) = \frac{FkTR_{IN}}{8\,(Q_0)^2\left(\frac{Q_L}{Q_0}\right)^2\left(\frac{R_{IN}}{R_{IN}+R_{OUT}}\right)^2\left(1-\frac{Q_L}{Q_0}\right)^2 4R_{OUT}\,P_{AVO}}\left(\frac{f_0}{\Delta f}\right)^2 \qquad \textbf{Eq. 2.46}$$

This can be rearranged to give:

$$L(f) = \frac{FkT}{32\,(Q_0)^2\left(\frac{Q_L}{Q_0}\right)^2\left(1-\frac{Q_L}{Q_0}\right)^2 P_{AVO}}\left(\frac{(R_{IN}+R_{OUT})^2}{R_{IN}R_{OUT}}\right)\left(\frac{f_0}{\Delta f}\right)^2 \qquad \textbf{Eq. 2.47}$$

Since, the input and the output impedances are equal; **Eq. 2.47** can be simplified as:

$$L(f) = \frac{FkT}{8\,(Q_0)^2 \left(\frac{Q_L}{Q_0}\right)^2 \left(1-\frac{Q_L}{Q_0}\right)^2 P_{AVO}} \left(\frac{f_0}{\Delta f}\right)^2 \qquad \textbf{Eq. 2.48}$$

And when considering the flicker noise in an amplifier under operating conditions **Eq. 2.48** becomes:

$$L(f) = \frac{FkT}{8\,(Q_0)^2 \left(\frac{Q_L}{Q_0}\right)^2 \left(1-\frac{Q_L}{Q_0}\right)^2 P_{AVO}} \left(\frac{f_0}{\Delta f}\right)^2 \left(1+\frac{f_c}{\Delta f}\right) \qquad \textbf{Eq. 2.49}$$

As seen in **Eq. 2.49**, the phase noise can be improved by increasing the quality factor of the resonator, increasing the power available to the resonator, decreasing the noise figure of the amplifier and by lowering the flicker noise corner of the amplifiers.

Eq. 2.49 can be optimised for minimum phase noise by differentiating it with respect to $\frac{Q_L}{Q_0}$ and then equating it to zero.

$$\frac{dL(f)}{d\left(\frac{Q_L}{Q_0}\right)} = 0 \qquad \textbf{Eq. 2.50}$$

It was shown that the minimum phase noise occurs when $\frac{Q_L}{Q_0}$=0.5 [11] which results **Eq. 2.48** to:

$$L_{MIN}(f) = \frac{2FkT}{(Q_0)^2 P_{AVO}} \left(\frac{f_0}{\Delta f}\right)^2 \qquad \textbf{Eq. 2.51}$$

Eq. 2.49 states that the phase noise of an oscillator can be improved by increasing the power in the amplifier and reducing the noise figure of the amplifier for a given (Q_L/Q_o)=0.5.

The phase noise spectrum of the oscillator mainly consists of $(1/f^3)$, $(1/f^2)$, $(1/f^1)$ and $(1/f^0)$ regions from **Eq. 2.20** as shown in **Figure 2.9**. The $(1/f^3)$ is due to the up

conversion the sustaining amplifiers flicker noise, $(1/f^2)$ is due to multiplication of the amplifier's white noise (leeson effect) and $(1/f^1)$ arises due to the flicker noise of the sustaining amplifier followed by the white noise $(1/f^0)$ at larger frequency offset.

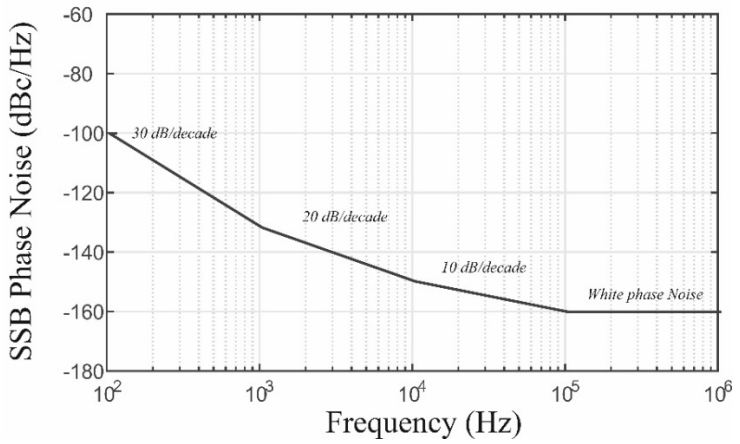

Figure 2.9: Spectrum of an oscillator.

2.4 Environmental Noise

High precision oscillators are used in modern day navigation systems such as cars, helicopters and unmanned aerial vehicles, radars to detect the target. At microwave frequencies, dielectric resonator oscillators are known to have a low phase noise, however when these communication systems are subjected to mild and harsh conditions, any acceleration such as shock or vibrations produced by the environment are picked up by the oscillators degrading their performances. This hence degrades the entire performance of the transmitter or the receiver system which might mask the signal containing useful information [21].

2.4.1 Vibrations Sensitivity of Oscillators

When an oscillator is subjected to vibration, the resonant frequency (f_o) of the oscillator shifts and this change in the frequency (Δf_o) is proportional to the

magnitude of the acceleration and the direction of the acceleration. The peak fractional change in the frequency is given by **Eq. 2.52** and **Eq. 2.53** [22]:

$$f(\vec{a}) = f_0(1 + \vec{\Gamma} \cdot \vec{a}) \qquad \textbf{Eq. 2.52}$$

$$y_{peak} = \frac{\Delta f_o}{f_o} = \vec{\Gamma}.\vec{a} \qquad \textbf{Eq. 2.53}$$

Where $|\vec{\Gamma}|$ is the acceleration sensitivity vector in the *x, y* and *z* directions and $|\vec{a}|$ is the peak applied vibration acceleration vector and the total acceleration sensitivity for a particular frequency in all the directions is given by **Eq. 2.54**:

$$|\overrightarrow{\Gamma_{total}}| = \sqrt{\Gamma_x^2 + \Gamma_y^2 + \Gamma_z^2} \qquad \textbf{Eq. 2.54}$$

The power spectral density is the rms value of the peak fractional frequency is given by **Eq. 2.55**:

$$S_y(f) = \frac{|y_{rms}|^2}{BW} = \left(\frac{\Delta f_{rms}}{f_o}\right)^2 \frac{1}{BW} = \left(\frac{\Delta f_0}{\sqrt{2} f_o}\right)^2 \frac{1}{BW} \qquad \textbf{Eq. 2.55}$$

Eq. 2.55 is related to the power density of the phase fluctuation $S_\varphi(f)$ as **Eq. 2.56**:

$$S_\phi(f) = S_y(f)\left[\frac{f_0}{f}\right]^2 \qquad \textbf{Eq. 2.56}$$

We know that the phase noise is related to the power spectral density by **Eq. 2.15**:

$$L(f) = \frac{1}{2}[S_\phi(f)] \qquad \textbf{Eq. 2.57}$$

And hence the phase noise under vibrations normalising to 1Hz bandwidth is given by **Eq. 2.58**:

$$L(f_v) = \frac{1}{2}\left[S_\phi(f)\right]$$

$$L(f_v) = \frac{1}{2}\left(\frac{\Delta f_0}{\sqrt{2} f_o}\right)^2 \left[\frac{f_0}{f_v}\right]^2 \qquad \textbf{Eq. 2.58}$$

$$L(f_v) = \left(\frac{\vec{\Gamma}.\vec{a}}{2f_v}\, f_0\right)^2$$

When **Eq. 2.58** expressed in dB:

$$L(f_v) = 20log\left(\frac{\vec{\Gamma}.\vec{a}}{2f_v}\, f_0\right) \qquad \textbf{Eq. 2.59}$$

Rearranging **Eq. 2.59** we get:

$$\Gamma_i = \frac{2\,.f_v}{a_i\,.f_0}\; 10^{\left(\frac{L(f_v)}{20}\right)}\,(g^{-1}) \qquad \textbf{Eq. 2.60}$$

The units for $L(f_V)$ is dBc/Hz and for random vibrations, the acceleration is represented by its power spectral density $|\vec{a}| = \sqrt{2PSD}$ (g/$\sqrt{\text{Hz}}$). The spectrum of the oscillators is indicated in an idealized form under vibrations is shown in **Figure 2.10**.

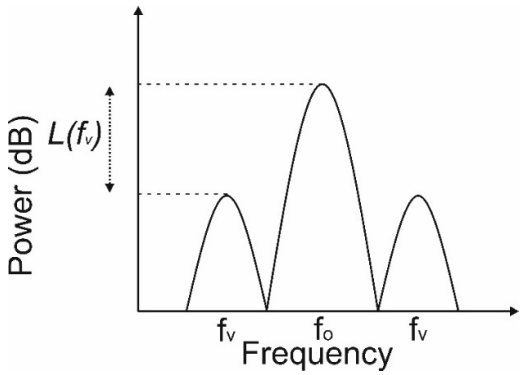

Figure 2.10: Sidebands caused by vibration in an oscillator.

It should be noted that when the oscillator frequency is multiplied by N in **Eq. 2.59**, the phase noise of the sidebands increases by 20log(N) as shown in **Eq. 2.61**.

$$L(f_v) = 20log\left(\frac{\vec{\Gamma}.\vec{a}}{2f_v}\,(Nf_0)\right) \qquad \textbf{Eq. 2.61}$$

Eq. 2.61 suggests that multiplying the carrier frequency by 10 times, the sidebands increase by 20dBc (20log(10)). For example, a 1GHz oscillator when subjected to a $\left|\vec{\Gamma}\right|$ of $1\text{x}10^{-9}$ per g when experiencing an acceleration $|\vec{a}|$ of 10g produces a sidebands of $L(f_V)$=-26dBc at 100Hz vibrations however when the same oscillator is multiplied by 10 times at 10GHz, produces sidebands which are -6.0dBc at 100Hz for the same conditions. The sidebands have increased by a factor of 20log(10)=20dB in this case [23].

In real world environment oscillators placed in navigation systems such as a ship faces up to 0.8 peak acceleration while a propeller aircraft faces up to 0.3-5g rms and the acceleration sensitivity on a helicopter is in the range of 0.1-7 g rms values. In the literature, DROs have been subjected to vibrations, an X band oscillator built at NIST when subjected to 0.5g rms acceleration had a vibration sensitivity of 10^{-7} in Z axis while 10^{-8} in the X and Y axes for a high Q resonator. Further, it was repeated with a low Q resonator, the vibration sensitivity was improved and it was shown that a high Q resonator was more sensitive to vibrations when compared to a low Q since the phase change with frequency of the resonator is steep at the frequency of oscillation and any vibration would modulate the centre frequency and hence change the phase. This would in turn change the quality factor of the resonator and change the phase noise [24]. Stockwell et al. built a sapphire based oscillator at 9GHz which had a vibration sensitivity of $5\text{x}10^{-9}$ in all the three axes when subjected to 0.1g acceleration and believed that a DRO would be in the range of 10^{-9} -10^{-7} [25].

2.5 Cross Correlation Measurement System

Residual noise which is also referred to as multiplicative noise is the noise which gets modulated onto a carrier in a less than perfect (real) 2 port device. Similar to the oscillator noise, it has both AM and PM noise associated with it but mainly the PM noise is of interest since the AM noise is usually very low. A conventional single channel phase noise measurement system is shown in **Figure 2.11** used to measure the PM noise of the DUT. The main purpose of this system is to measure the PM noise by isolating the multiplicative noise produced by the DUT. A very low noise signal source is used as a reference source for the system which is split using a splitter into two separate paths. This drives the DUT and hence drives the signals to the LO and the RF port of the mixer. There is a phase shifter in one of the paths of the signal to set the mixers to be in quadrature and hence the mixer behaves as a phase detector. It is assumed that the phase noise of the source gets correlated at the inputs of the phase detector and therefore gets cancelled and only the noise of the DUT gets measured. Finally, the IF signal gets filtered using a low pass filter and then amplified before being fed into an FFT analyser where the spectral density of the noise at the output of the mixer is measured.

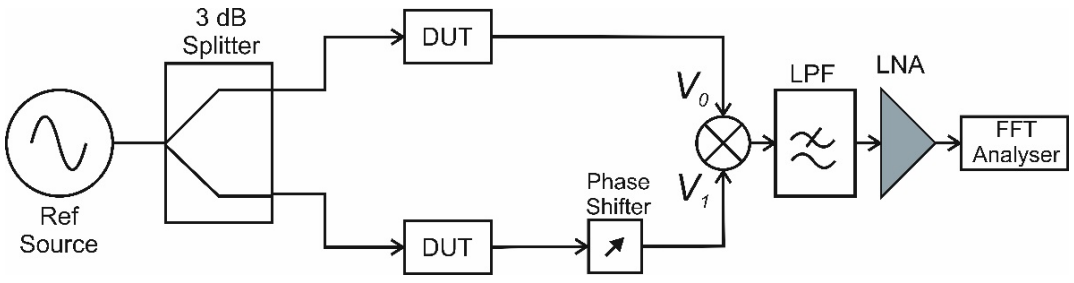

Figure 2.11: Single channel residual phase noise measurement system.

This can be demonstrated as follows, let us assume the V_0 and V_1 are the signals at the LO and the RF port given as shown in **Eq. 2.62** and **Eq. 2.63** [26].

$$V_0(t) = V_L Cos\big(\omega_L t + \varphi(t)\big) \qquad \textbf{Eq. 2.62}$$

$$V_1(t) = V_R Cos(\omega_R t) \qquad \textbf{Eq. 2.63}$$

At the output of the mixer, the IF is given by **Eq. 2.64**:

$$V_{IF}(t) = V_0(t) \text{ x } V_1(t)$$
$$V_{IF}(t) = V_L V_R\, Cos\big(\omega_L t + \varphi(t)\big)\, Cos(\omega_R t) \qquad \textbf{Eq. 2.64}$$

Using the trigonometry identity: $\cos\alpha \,.\cos\beta = \frac{1}{2}[\cos(\alpha+\beta) + \cos(\alpha-\beta)]$ and substituting this in **Eq. 2.64** we get **Eq. 2.65**:

$$V_{IF}(t) = \frac{V_L V_R}{2} \quad \big[Cos\big(\omega_L t + \omega_R t + \varphi(t)\big) + Cos\big(\omega_L t - \omega_R t - \varphi(t)\big)\big] \qquad \textbf{Eq. 2.65}$$

When the mixer operates as a phase detector then the frequencies are equal $\omega_L = \omega_R$, **Eq. 2.65** changes to **Eq. 2.66**.

$$V_{IF}(t) = \frac{V_L V_R}{2} \quad \big[Cos\big(2\omega_L t + \varphi(t)\big) + Cos\big(\varphi(t)\big)\big] \qquad \textbf{Eq. 2.66}$$

The signals are 90^{o} out of phase $\varphi(t) = (N+1)90° + \Delta\varphi(t)$ and this signal passes through the low pass filter, hence the higher frequencies can be filtered out, resulting in **Eq. 2.67**. The other advantage of the mixers being in quadrature mode is that at this point, the mixers are most sensitive to PM fluctuations while least sensitive to AM noise [27]. **Eq. 2.66** now reduces to **Eq. 2.67** using the quadrature condition.

$$V_{IF}(t) = \frac{V_L V_R}{2} \quad \big[Sin\big(\Delta\varphi(t)\big)\big] \qquad \textbf{Eq. 2.67}$$

For small angles$\big(\Delta\varphi(t)\big) \ll 1;\ Sin\big(\Delta\varphi(t)\big) \simeq \big(\Delta\varphi(t)\big)$; using this in **Eq. 2.67** we get:

$$V_{IF}(t) = K_d\, \Delta\varphi(t) \qquad \textbf{Eq. 2.68}$$

Where $K_d = \frac{V_L V_R}{2}$ is the phase detector constant. **Eq. 2.68** leads to a direct linear relationship between the voltage and the phase fluctuations of the input signals. However, the noise from the mixer, filter and the low noise amplifier gets onto the IF and hence to suppress these noises, cross correlation technique is used were by the uncorrelated noise in each arm can be suppressed by a factor of $\sqrt{N}$ where N is the number of correlations as seen in **Figure 2.12** [28].

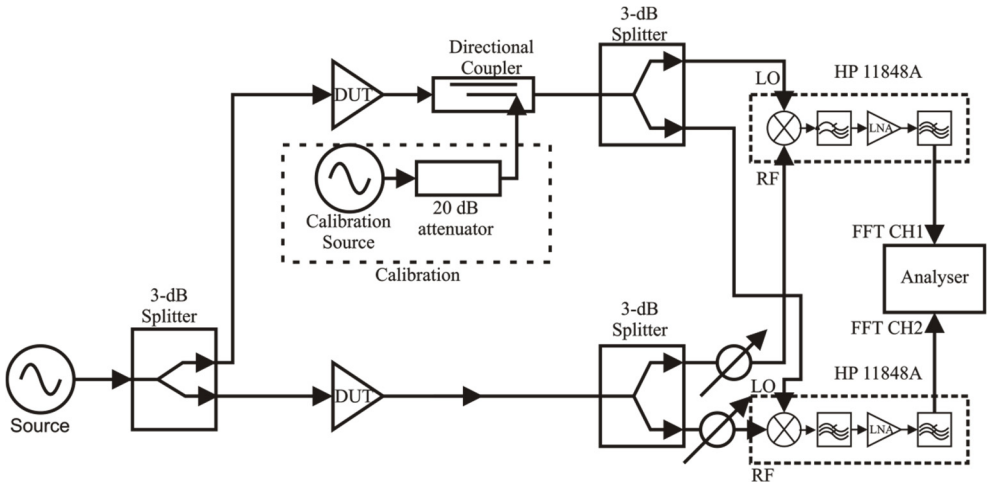

Figure 2.12: Cross Correlation measurement setup using two HP11848A.

Let us assume *x(t)* and *y(t)* are the noisy signals in the time domain present at the output of the phase detectors. *a(t)* and *b(t)* are the uncorrelated noise of the instrument and *c(t)* is the correlated DUT noise in each arm as **Eq. 2.69** and **Eq. 2.70** [29]:

$$x(t) = a(t) + c(t) \underset{FFT}{\longleftrightarrow} X(f) = A(f) + C(f) \qquad \textbf{Eq. 2.69}$$

$$y(t) = b(t) + c(t) \underset{FFT}{\longleftrightarrow} Y(f) = B(f) + C(f) \qquad \textbf{Eq. 2.70}$$

The cross spectrum of these signals is given by **Eq. 2.71**:

$$\overline{S_{XY}} = \frac{1}{N}\sum_{n=1}^{N}[X_n \times Y_n^*] \qquad \textbf{Eq. 2.71}$$

Eq. 2.71 leads to **Eq. 2.72** and **Eq. 2.73**:

$$\overline{S_{XY}} = \frac{1}{N}\sum_{n=1}^{N}[(A_n + C_n) \times (B_n + C_n)^*] \qquad \textbf{Eq. 2.72}$$

$$\overline{S_{XY}} = \frac{1}{N}\sum_{n=1}^{N}[(A_n B_n{}^*) + (A_n C_n{}^*) + (C_n B_n{}^*) + (C_n C_n{}^*)] \qquad \textbf{Eq. 2.73}$$

If we assume there are no correlations between these signals, then all the uncorrelated terms in **Eq. 2.73** is zero and only the correlated noise from the DUT is measured.

CHAPTER 3

3.8GHz DIELECTRIC RESONATOR OSCILLATOR

3.1 Introduction

In this chapter, the design and measurements of 3.8GHz oscillators incorporating dielectric resonators built for Selex-ES with low vibration sensitivity have been described. A high Q resonator and a low noise amplifier are key elements in a low phase noise oscillator. As dielectric resonators usually offer high Q factors, controllable temperature coefficient and low sensitive to vibrations they are used in the oscillators. The maximum quality factor is determined by the loss tangent (tan δ) of the dielectric material. For a dielectric resonator, the product of Qxf is approximately a constant. Dielectric resonators such as Barium Tetratitanate are available with an unloaded quality factor of 60,000 at 2GHz when operating in TE_{01} mode [30] however as we go higher in frequency, sapphire based resonators have higher quality factors when compared to the dielectric resonators but these have higher sensitivity to temperature fluctuations and are also expensive. The other advantage of dielectric resonators is that they are able to sustain powers from a few mill watts to few watts when compared to a crystal resonator. Hence with a high circulating power, it is possible to design oscillators which have better phase noise

compared to that of a crystal oscillator multiplied up to at microwave frequencies. Also, at these microwave frequencies, the performance of the oscillator is highly dependent on the active device used in the oscillator. Silicon Germanium (SiGe) and heterojunction bipolar transistors (HBT) with high f_t which exhibit low flicker corner are usually used as the active device since the phase noise is inversely proportional to the power, it is often useful to have a higher power active device.

Several authors have demonstrated oscillator performance utilising materials such as sapphire and ceramic for resonators from 4-5GHz. Initially, M. Regis et.al. demonstrated a phase noise of -133 dBc/Hz at 1kHz offset for a 4.85GHz oscillator using a SiGE HBT device and a sapphire resonator with a loaded Q of 60,000 [31]. Later, a phase noise of -138 dBc/Hz at 1kHz and by extrapolation close to -165 dBc/Hz at 10kHz offset was measured using a sapphire resonator with an loaded Q of 75,000 at 4.85GHz [32]. A SiGe device (Infineon BFP620F) was used with a ceramic resonator of unloaded Q of 33,000 demonstrated a phase noise of -146 dBc/Hz at 10kHz offset at 4GHz [33]. Sallin, Zhou, Broomfield and Everard demonstrated a phase noise of -135 dBc/Hz at 10kHz using a ceramic dielectric resonator with an unloaded Q of 17,400 at X band [34]. Later, Everard and Theodoropoulos demonstrated a 1.2GHz band using a ceramic resonator with a phase noise of <-173 dBc/Hz [30].

In this chapter, the design and construction of a 3.8GHz low vibration sensitivity, ultra-low phase noise DRO developed for Selex-ES is presented which is based on the feedback topology. The initial oscillators demonstrated a phase noise of -117 dBc/Hz at 1kHz offset and -150 dBc/Hz at 10kHz offset as the oscillator is in the flicker noise region the slope is 30dB per decade. Most of the elements on the PCB boards are printed in order to reduce the vibration sensitivity. The vibration

sensitivity (τ_i) varied from 1.33×10^{-7} to 8.51×10^{-9} per g depending on the axis and the frequency of the vibration. Later in the second prototype developed for University of York, the oscillator demonstrated a significantly improved phase noise performance of -125.6 dBc/Hz at 1kHz offset and -153 dBc/Hz at 10kHz offset which is the lowest noise reported in the literature in this frequency band using a dielectric resonator. The improved performance is mainly due to an increase in the power level and the reduced noise figure. In the following sections the simulations, design and measurement of the individual oscillator elements for both the prototypes are presented.

3.2 Oscillator Elements

The block diagram for the feedback topology oscillator is shown in **Figure 3.1**. All the elements were simulated and optimised individually and then combined to make a compact prototype of the oscillator.

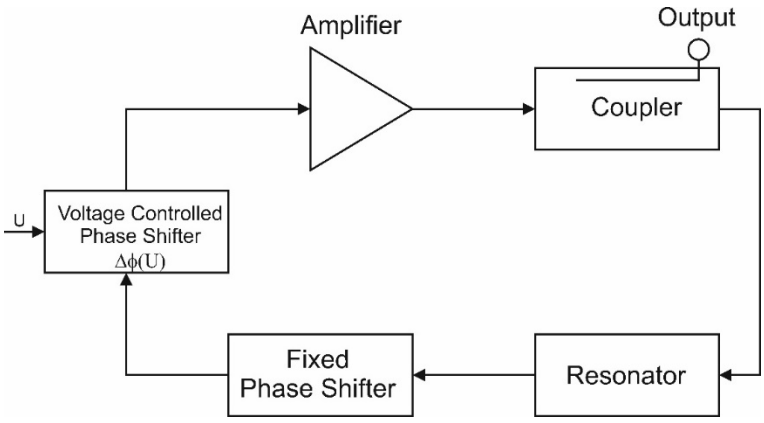

Figure 3.1: Oscillator block diagram using the feedback topology.

The oscillator consists of 5 parts:

1. Amplifier: An amplifier is required to sustain the oscillation. The gain should be sufficient to cancel the insertion loss of the other elements and guarantee oscillation under all operating conditions. A push pull amplifier using SiGe BFP380F transistors with a gain of around 10dB, noise figure (NF) of 4dB and output power of 20dBm has been built.
2. Resonator: The resonator is the frequency selective element in an oscillator and in this instance a dielectric resonator was used which mounted on an alumina tube in order to increase the quality factor and printed transmission lines were used to couple in and out of the resonator. The dielectric resonator had an unloaded Q of around 20,000. The insertion loss *(S_{21})* of the resonator is optimised to be around -6dB to achieve optimum phase noise performance.
3. Electronically Tunable Phase Shifter: A phase shifter is used to tune the loop phase and hence oscillator frequency of the entire circuit. A voltage controlled phase shifter is designed with a low insertion loss which provides a tunable phase shift of about +110° using varactor diodes.
4. Fixed phase shifter: This is used to set the loop phase shift to N × 360° and is made up of printed transmission lines and short lengths of semi-rigid cable.
5. Output Coupler: A printed 10dB multi-section single layer coupler has been designed in order to integrate external devices.

A compact amplifier design which also includes the electronic phase shifter, output coupler and resonator coupling probes was developed on a single high Rogers 3006 substrate with a ε_r=6.5 with a loss tangent (tanδ) of 0.0020. This configuration enables the resonator to be measured separately; however, the amplifier, phase shifter and output coupler have to be measured together and the picture of the oscillator

board is shown in **Figure 3.2**. The design and simulations of the individual elements for the amplifier, phase shifter, output coupler and resonator are now described in the following sections.

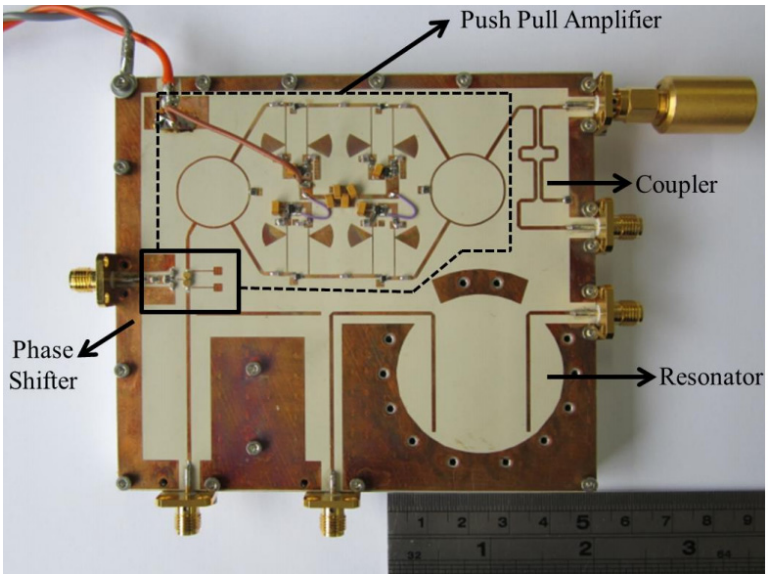

Figure 3.2: Picture of the compact dielectric resonator oscillator with individual elements. The oscillator measures 125×115×40mm.

3.3 Amplifier

The active element used in an oscillator needs to have a low noise figure, high output power and low flicker noise. There are a large number of devices that are available which have low noise figure and high output power at microwave frequencies. GaN and GaAs are suitable to use as an active device since they have high output power and also have low noise figure [35]. However, the flicker noise and phase noise of such devices are up to a few MHz [36] [37] it is undesirable since the flicker noise gets up converted in an oscillator. Hence, SiGe transistors are a suitable choice for transistors

when used in an oscillator. The gain of the amplifier needs to be around 8-10dB inside the oscillator loop to compensate the loss from the resonator which is set to 6dB for minimum phase noise and the losses from the other elements such as the electronic phase shifter, coupler and the cables (maximum of 2dB). Also, the amplifier needs to be unconditionally stable since during oscillation the impedances presented at the input and the output are poorly defined. There are a number of such devices available from different manufactures but the devices selected were the BFR380F and BFP620F which were both SiGe devices from Infineon devices. The BFR380F had a P_1dBm of 17dBm while the BFP620F had a P_1dBm of 15dBm but both these devices had a similar noise figure of 4dB at 4GHz. However, the BFP620F had a gain of about 10dB at 4GHz while the BFR380F had a gain of about 5dB at 4GHz. Hence both of these devices were simulated in order to optimise the gain, noise figure and the output power as these parameters directly affect the phase noise of the oscillator. However, simulations suggest that the BFP620F had a slightly high noise figure of 6dB and a low output power of 14dBm at 3.8GHz when compared to the BFR380F transistors and hence BFR380F was investigated.

The BFR380F is a silicon bipolar transistor from Infineon devices is one such device which has a gain of about 5 dB at 4GHz with a collector current of I_c=40mA and V_{CE}=3Vand the S parameters for the device at 4GHz is shown in **Table 3.1** for I_c=40mA and V_{CE}=3V. The transistor also has an output compression point P_1dBm of 17dBm at 4GHz and hence based on this information, the BFP380F transistor was chosen for the amplifier.

Table 3.1: S Parameters of BFR380F with I_c=40mA and V_{CE}=3V at 4GHz

S parameters	Magnitude	Angle
S_{11}	0.6108	144.9
S_{21}	1.826	50.7
S_{12}	0.2335	62.6
S_{22}	0.2258	-171.3

3.3.1 Single Stage Amplifier using SiGe BFR380F

A single stage amplifier was designed in CE configuration as shown in **Figure 3.5** and the amplifier block consists of a single transistor (BFP380R) from Infineon. An Infineon BCR400W active bias controller is used to bias the microwave transistor which is a low voltage drop device capable of stabilising the bias current of an NPN transistor from 0.2mA to over 200mA and includes temperature compensation elements. The quiescent current is set by R_{EXT}. The bias for the transistors was set to 40mA for a V_{CE} of 4V for the maximum output power. The printed bias tee's are used in order to present high impedance (open circuit) to the RF signal and low impedance at DC. The bias tees consist of a short 85Ω upper element, a radial stub and an 85Ω ($\lambda_g/4$) element. The length of the lines in the radial stubs were optmised using momentum in ADS and the plot of s parameters in shown in **Figure 3.3** which has loss of 0.2dB at operating frequency and **Figure 3.4** shows the smith chart which indicates the open circuit at 3.8GHz. It shows a good 50Ω match at 3.8GHz.

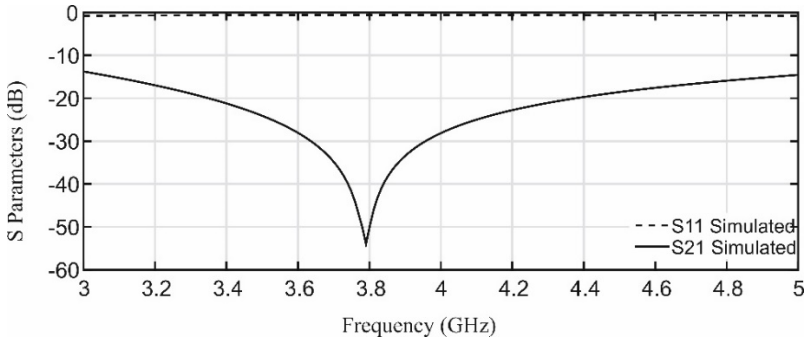

Figure 3.3: Momentum simulation using transmission lines of the radial stubs optimised at 3.8GHz.

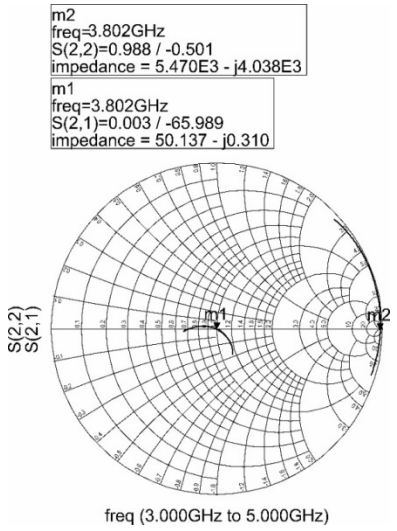

Figure 3.4: Smith chart plot of the radial stubs from 3GHz to 5GHz which shows the open circuit at 3.8GHz.

The amplifier was simulated using Agilent Advance Design Software (ADS) using transmission line models and the models for the transistor and the active bias were imported. Rogers 3006 substrate ($\mathcal{E}_r$=6.5 with a loss tangent (tanδ) of 0.0020, thickness of 0.64mm with a copper cladding of 17µm) was used for simulations and

fabricate the boards in order to keep the boards compact. The simulations suggest that the amplifier had a gain of 5 dB at 3.8GHz as shown in **Figure 3.6**.

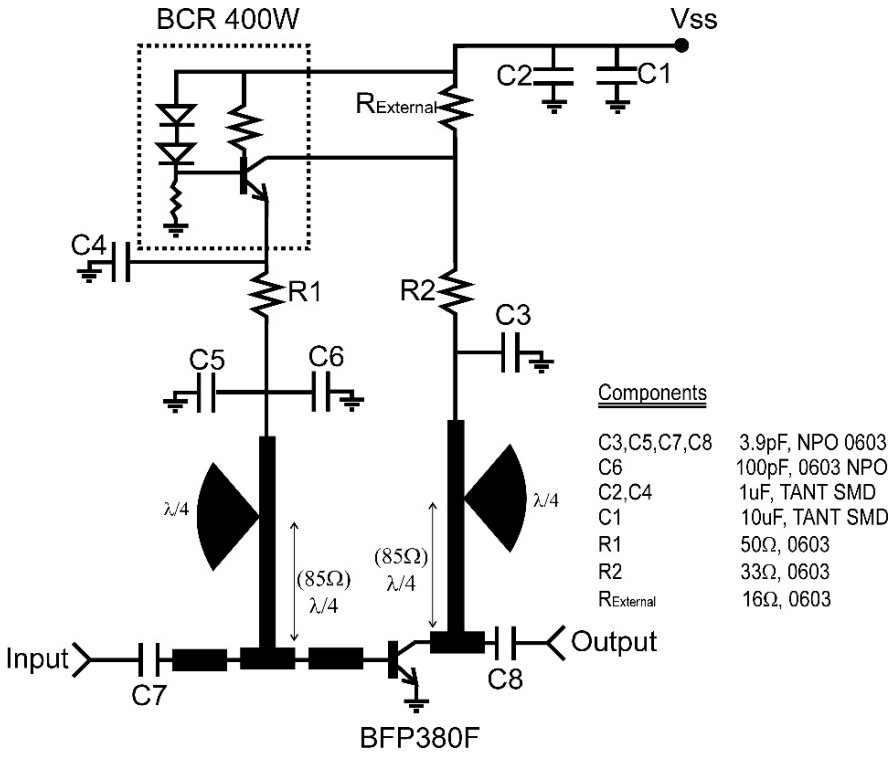

Figure 3.5: Single Stage amplifier using BFP380F for I_c=40mA and a V_{CE} of 4V.

An amplifier can oscillate if the input or the output impedances have a negative real part, i.e if $|\Gamma_{in}|>1$ or $|\Gamma_{out}|>1$. Hence the amplifier was also checked for its stability using **Eq. 3.1** and **Eq. 3.2** which states that the amplifier is unconditional stable if $|\Gamma_{in}|<1$ or $|\Gamma_{out}|<1$ for all passive source and load impedances ($|\Gamma_S|>1$ or $|\Gamma_L|>1$) [38].

$$|\Gamma_{in}| = \left(|S_{11} + \frac{S_{12}S_{21}\Gamma_L}{1 - S_{22}\Gamma_L}|\right) < 1 \qquad \textbf{Eq. 3.1}$$

$$|\Gamma_{out}| = \left(|S_{22} + \frac{S_{12}S_{21}\Gamma_S}{1 - S_{11}\Gamma_S}|\right) < 1 \qquad \textbf{Eq. 3.2}$$

The amplifier was also simulated in Agilent ADS for its stability using the $K-\Delta$ test, which states that a transistor is unconditionally stable if Rollet's condition, K, is greater than unity and the auxiliary condition, $|\Delta|$, is less than unity. As $K>1$ and $|\Delta|<1$ the transistor is unconditionally stable upto 12GHz using **Eq. 3.3** and **Eq. 3.4**.

$$|\Delta| = |S_{11}S_{22} - S_{12}S_{21}| \qquad \textbf{Eq. 3.3}$$

$$K = \frac{1 - |S_{11}|^2 - |S_{22}|^2 + |\Delta|^2}{2|S_{12}S_{21}|} \qquad \textbf{Eq. 3.4}$$

The amplifier was also simulated for its output compression point and noise figure using the PSIPCE model which suggested a noise figure of 5dB and an output compression point of 17dBm at 3.8GHz. The dips at 2.7 GHz and around 6 GHz are due to the radial stubs which present an open circuit to the RF circuit and an open circuit to the DC end of the circuit.

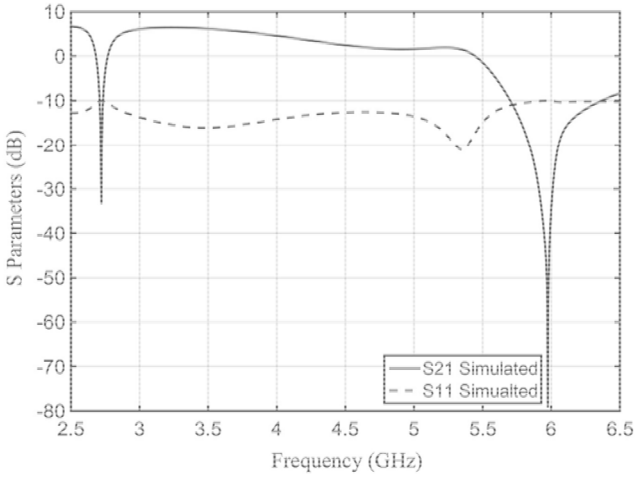

Figure 3.6: Simulated frequency response for a single stage amplifier using the SiGe BFP380F transistors.

3.3.2 Push Pull Amplifier

The simulated gain of the amplifier was about 5dB at 3.8GHz; hence it was decided to use two amplifiers in series to have a potential combined gain of 10dB at 3.8GHz ignoring the losses from the couplers. The amplifiers were then combined using the Rat Race couplers in the Push Pull configuration. In this configuration, the amplifier consists of two similar transistors with similar CE amplifier topology which have equal gain, 1-dB compression points and noise figure connected in series. Then, each arm is then connected and a rat race coupler was used with balanced (180°) outputs as shown in **Figure 3.7**. The advantage of using a rat race coupler in a Push Pull configuration is that it provides a 3dB increase in the output power [38] however, simulations suggested no reduction to the overall noise figure. If Na is the noise figure of the individual cell, then the overall noise figure was found to be (Na+Na)/2 for the push pull amplifier.

Table 3.2: Widths and lenghts using the Rogers3006 boards with ε_r=6.5 and loss tangent (tanδ) of 0.0020 at 3.8GHz

Transmission Line Impedance	Width	Length ($\lambda_g/4$)
50Ω	0.88 mm	8.7 mm
70.71Ω (Rat Race Couplers)	0.42 mm	
85Ω (Bias Tee)	0.255 mm	9.01 mm

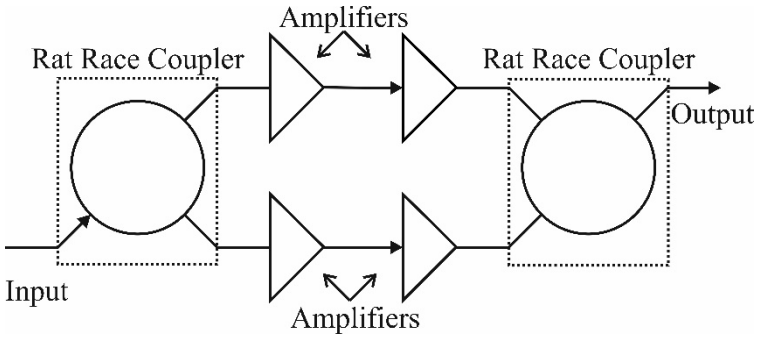

Figure 3.7: Push Pull Amplifier Block Diagram.

The single stage amplifiers were simulated in Momentum ADS to have a more accurate model of the single stage and then imported back in the schematic in order to run an ADS co-simulation with the transistors models. The Push Pull amplifier was simulated for its gain, noise figure and output compression point (P_1 dBm). The gain was simulated to be 10.1dB at 3.8GHz with a noise figure (NF) of 5.1dB as shown **Figure 3.8** and **Figure 3.9**. Also, the output compression point (P_1 dBm) of the amplifier was simulated to be 20dBm.

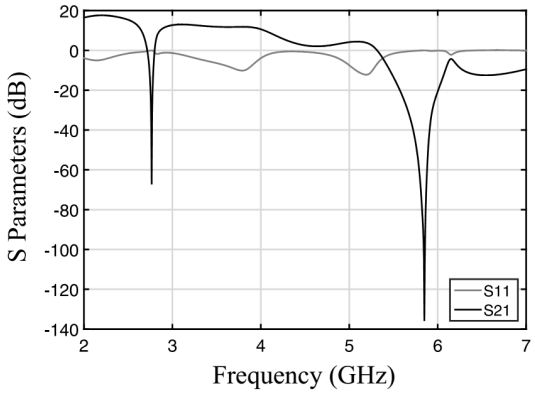

Figure 3.8: Simulated S Parameter response for a Push Pull Amplifier using the Rat Race couplers in Momentum ADS.

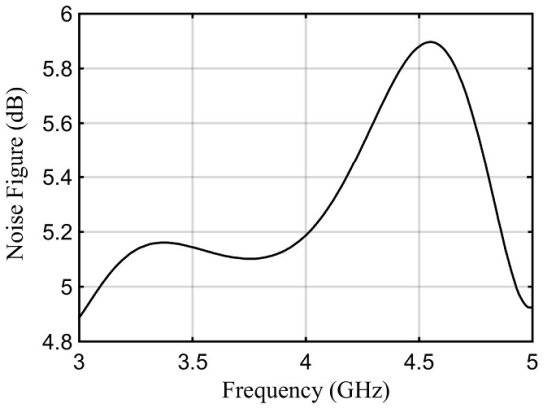

Figure 3.9: Simulated noise figure using the PSPICE model imported in ADS.

In the present configuration, the electronic phase shifter, amplifier and the coupler response had to be measured together due to the PCB design. The combined measured frequency response is shown in **Figure 3.10**. This demonstrates a gain of 9.8dB at 3.8GHz.

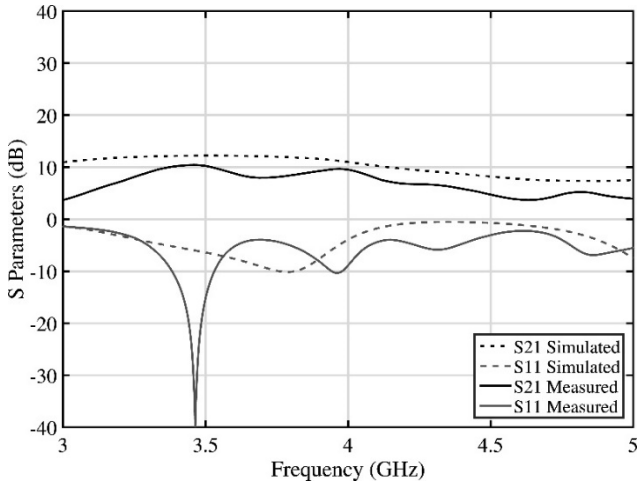

Figure 3.10: Comparison of the simulations and measurements of the Amplifier + Coupler + Electronic Phase Shifter.

Next the noise figure was measured using an HP8970B noise figure meter using the double side band method [39]. This instrument only operates up to 1.6GHz

so it is necessary to use a mixer. The HP346B noise source operates up to 18GHz. The noise meter is set to measure the noise figure at an IF frequency of 10MHz so this system measures the noise figure of the amplifier at +10MHz around the signal generator as shown in **Figure 3.11**. As long as the amplifier performance is constant over this 20MHz spacing then a correct reading can be obtained. The signals are down converted using a Minicircuits mixer ZEM-4300. The device is calibrated from the noise meter to the mixer as the mixer has a loss associated with it. The LO signal is provided by a signal generator with a 17dBm output power level via a 10dB attenuator. The mixer LO power is therefore +7dBm. A noise figure (NF) of 4dB was measured at 3.8GHz.

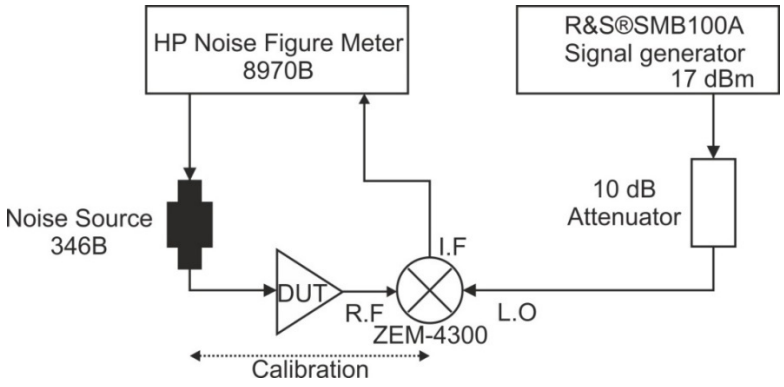

Figure 3.11: Noise Figure Measurement setup for the 3.8GHz amplifier.

Finally, the output 1dB compression point was measured using the setup shown in **Figure 3.12**. A directional coupler is used at the input of the amplifier to measure the input power available to the amplifier. Also, a 10dB attenuator is used at the output of the amplifier in order to protect the power meter. The P_1dBm point was measured to be 20dBm.

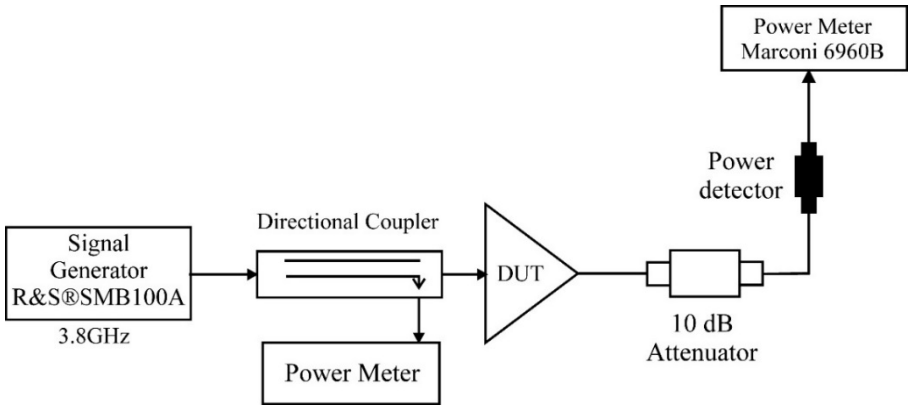

Figure 3.12: Power measurement setup for the 3.8GHz amplifiers using Marconi power meter 6960B.

3.4 Dielectric Resonator

Resonator is the frequency selective element, which is used in a feedback configuration to establish the correct oscillation frequency. Dielectric resonators are a suitable choice in an oscillator since they offer high Q factors, controllable temperature coefficient and a high power handling capability at microwave frequencies compared to crystal resonators and hence ensures low phase noise close and far away from the carrier. Dielectric materials with a $\mathcal{E}_r$ ranging from 20-90 with a high Q is usually used as resonator and have a constant Q x f bandwidth. For example, commercially available DRs which have a $\mathcal{E}_r$ of 30 have an unloaded Q of 60,000 at 2GHz and a Q of 30,000 at 4GHz and so on. A common mode used in a dielectric resonator is the $TE_{01\delta}$ mode where δ is the mode number [38] and the electric and magnetic field intensity for this mode is shown in **Figure 3.13** simulated using CST Microwave Studio™ where the arrows represent the intensity and the direction of the electric and the magnetic field of a dielectric puck. Most of the electric and the magnetic energy are stored in the dielectric cylinder and the

remaining energy is distributed in the air surrounding the puck. Looking at the field pattern, the electric filed is almost zero at the centre of the dielectric resonator and the maximum occurs around at ¾th radius away from the centre of the resonator and the magnetic field is the strongest at the centre. Hence, a cylindrical plug can be removed from the centre without disturbing any field as shown in **Figure 3.14**. Coupling to the $TE_{01\delta}$ mode is accomplished with the help of transmission lines placed near to the dielectric puck using the magnetic field or with the help of a small dipole to couple onto the electric field [40].

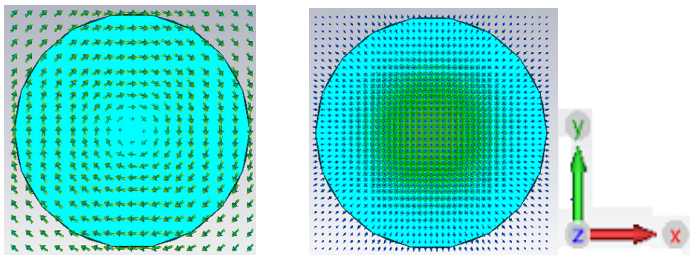

Figure 3.13: Electric and Magnetic fields for a solid resonator puck for TE_{01} using CST at 3.8GHz.

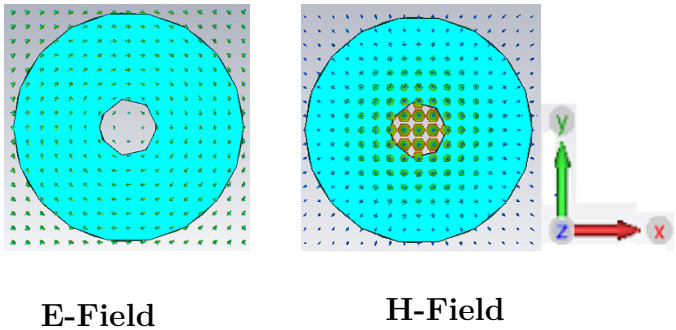

Figure 3.14: Electric and Magnetic fields for a new tubular resonator puck for TE_{01} using CST at 3.8GHz.

The dimensions of the dielectric puck determine the resonance frequency [40] and for a given radius *'a'* and height *'l'*, for a TE_{01} the resonant frequency is given by:

$$f_r(TE_{mnp}) = \frac{1}{2\pi\sqrt{\mu\epsilon}}\sqrt{\left(\frac{\chi'_{mn}}{a}\right)^2 + \left(\frac{p\pi}{l}\right)^2} \qquad \textbf{Eq. 3.5}$$

Where χ'_{mn} represents the n^{th} zero of the derivative of the Bessel function of the first kind of order m and in the case of the TE_{01} mode the value of χ'_{mn} is 3.8318. The dielectric resonator which were used were made from Barium Tetratitanate which has a dielectric constant ($\mathcal{E}_r$) of 30 and an unloaded Q of 30,000 at 4GHz. At 3.8GHz, the values of *'a'* is 8.01mm and *'l'* was 6.68mm for a $\mathcal{E}_r$ of 30 calculated using **Eq. 3.5**. The dielectric puck was mounted on a short alumina spacer and then bonded to the aluminum base using a two-part epoxy as shown in **Figure 3.15**. The total structure could then be fitted and bolted into the base of the box. This allowed easy replacement and modification of the resonator. The main reason for the alumina spacer to be used was to increase the quality factor. As a high Q material is brought close to a lossy material (in this case Rogers 3006 substrate) and the base aluminium metal plate, the Q of the resonator significantly reduces from 9000 to 1000.

Figure 3.15: The dielectric puck was mounted on a short alumina spacer and then bonded to the aluminum base using two-part epoxy.

Printed transmission lines were used to couple energy in and out of the cavity since the entire structure needed to be less vibration sensitivity. When transmission lines are used to couple energy, the lateral distance between the dielectric resonator and the transmission line determines the amount of coupling and in order to minimise the radiation loss, the DR is usually enclosed in a metallic enclosure. For an open circuit transmission line, the current maximum occurs at a distance ($\lambda_g/4$) away from the open circuit end and current minimum occurs at ($\lambda_g/2$) away from the end. For a Rogers 3006 substrate, the ($\lambda_g/4$) point is 6.723mm and ($\lambda_g/2$) point is 13.44mm away from the open circuit end which means that minimum insertion loss has to occur at 6.7mm away from the open circuit end and maximum current occurs at 13.44mm which leads to better coupling and hence high Q. Also, increasing the separation between the transmission lines effectively increases the insertion loss since the magnetic field is weaker at greater distances and based on the simulation the optimum spacing was found to be 21.6mm between the transmission lines.

3.4.1 Simulations and Measurements

CST Microwave Studio was used to simulate the frequency response of the dielectric resonator. The initial lengths of the transmission lines were set to 28mm while the spacing between the printed transmission lines was 21.6mm and frequency domain solver with hexahedral mesh was used for simulations. To begin with, the simulation was carried out for a span of 5GHz but when no lower frequency modes were seen below 3.8GHz, the frequency span was reduced to ±100MHz to get a more accurate measurement of the insertion loss and the loaded Q. A number of probe simulations and experiments were conducted on a set of transmission lines to set the right insertion loss and loaded Q *(Q_L)* to achieve a low phase noise for the oscillator. The

top view, perspective and the dielectric resonator along with its enclosure is shown in **Figure 3.16** for the straight micro strip coupling probes for the resonator.

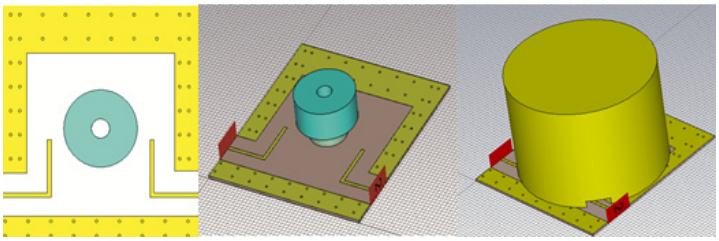

Figure 3.16: CST model of the resonator using straight transmission lines.

The dielectric puck is represented by dark blue colour while the alumina support underneath is represented by light blue as seen in centre of **Figure 3.16**. The PCB copper cladding is in yellow along with the transmission lines (extreme left) while the aluminium cavity is also in yellow (extreme right in the **Figure 3.16**).

The lengths of the transmission lines were reduced by 1mm at a time and the resonator was simulated for its insertion loss *(S_{21})* and loaded Q *(Q_L)*. The frequency response of the resonator for various lengths of the transmission lines is shown in **Figure 3.17**. As the length of the transmission lines is reduced, the coupling between the magnetic fields between the microstrip lines and the dielectric resonator changes and hence the insertion loss and the loaded Q. The change of frequency is believed to be an artifact of the simulator and was not observed during the experiments.

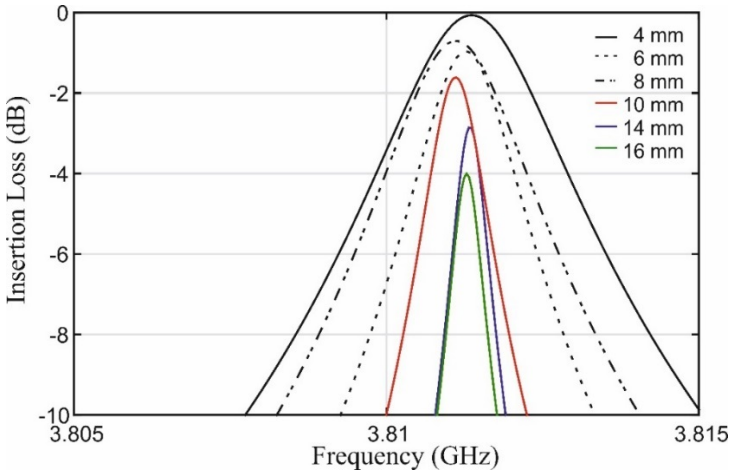

Figure 3.17: Variation of Insertion Loss and Loaded Q vs length of the straight coupling transmission lines simulated using CST.

In order to verify the simulations, PCB boards using Rogers 3006 were fabricated where the initial straight micro strip coupling probes were 28mm long and 21.6mm apart as shown in **Figure 3.18**. The measurement demonstrated that the insertion loss was (S_{21}) was -1.414 dB with a loaded Q, Q_L of 1766 for a 28mm length line. The insertion loss was optimised by cutting away the lines 1mm at a time whilst measuring the insertion loss and the loaded Q of the resonator. It should be noted that reduction in length by 1mm might not have been accurate enough as the reduction was done with the help of scalpel. The insertion loss was noted down for each measurement. The calibration was done at the start at 3.813 GHz and the same calibration was recalled every time. The unloaded Q, Q_0 is calculated using:

$$Q_0 = \left(\frac{Q_L}{1 - |S_{21}|}\right) \qquad \textbf{Eq. 3.6}$$

Two useful probe lengths for the oscillators were:

1. 12 mm in length, where S_{21} was -4.252 dB and Q_L was 7675 and hence Q_0 was calculated to be 19,829.

2. 11 mm in length, where S_{21} was -6.6 dB and Q_L was 10,495. Q_0 was calculated to be 19,669 using **Eq. 3.6**.

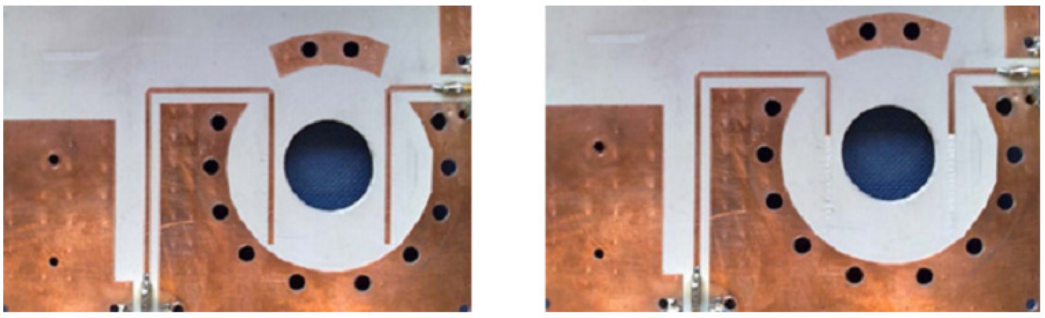

Figure 3.18: Experiment to set the right insertion loss and the loaded Q using the straight micro Strip lines for the resonator.

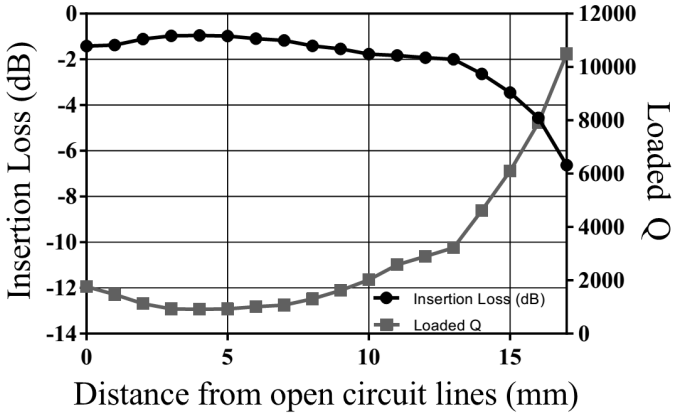

Figure 3.19: Plot of Insertion Loss/Loaded Q vs length of the straight coupling transmission lines.

It can be seen that at ($\lambda_g/4$) which is 6.7mm, where a current maximum exists and where the optimum coupling should be achieved. The data indicates that the minimum insertion loss occurs at 4.3mm and this is in agreement with the theory as shown in **Figure 3.19**. The **Table 3.3** shows the comparison of the simulation and

the experiment loaded Q *(Q_L)* for the distance from the open circuit lines. The measurement error is 5% to 10% from that of simulations.

Table 3.3: Comparison of the loaded Q for the simulations and measurements.

Distance from the open circuit lines (mm)	**Loaded Q (Simulations)**	**Loaded Q (Measurements)**
0	1654	1766
4	1010	913
8	1310	1307
12	2910	2898
14	4480	4620
16	8265	7675

Since the maximum unloaded Q was obtained at 16mm, the lengths were not reduced further and were used for the final prototype of the oscillators. **Figure 3.20** shows the response of the resonator with a 6GHz span with a reduced length of 16mm with no lower order modes observed in the resonator. The required TE_{011} mode can be observed with an insertion loss *(S_{21})* of -20.53 dB since there is not enough number of points. The span was then reduced to 10MHz in order to get an accurate measurement of the insertion loss *(S_{21})* and loaded Q *(Q_L)*. The response of the resonator with the reduced span which demonstrated an insertion loss of -4.2 dB with a loaded Q of 7,675 is shown in **Figure 3.21**. The unloaded Q was then calculated to be 19,829 using **Eq. 3.6**.

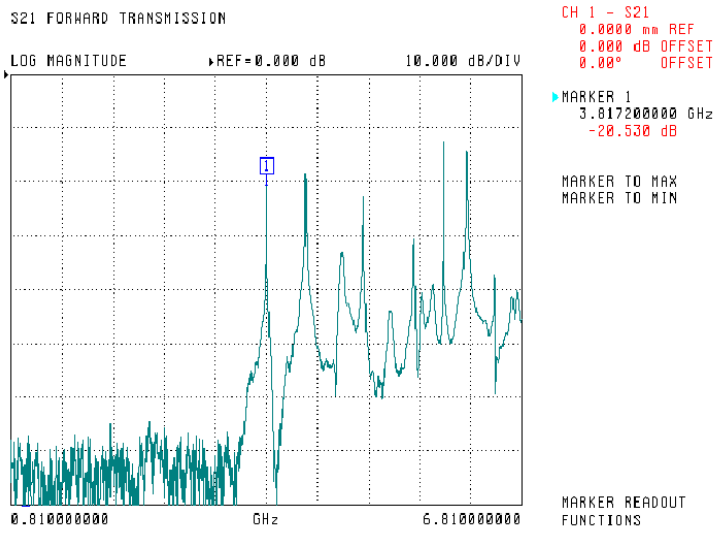

Figure 3.20: Resonator response with a 6 GHz span where the TE_{01} mode can be seen at the centre of the plot.

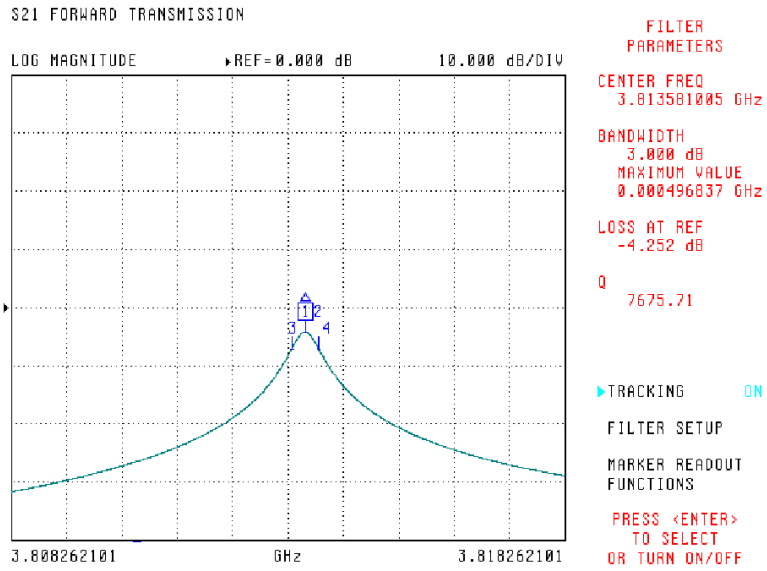

Figure 3.21: Measured Insertion Loss (S_{21}) of -4.252dB and Loaded Q, (Q_L) of 7675 for a span of 10MHz for the 3.8GHz dielectric resonator.

3.5 Voltage Controlled Phase Shifter

In a dielectric resonator oscillator (DRO), the frequency of operation is fixed and determined by the resonator. The frequency of oscillation can be changed externally by mechanical tuning of the resonator where the magnetic field distribution is changed around the resonator by moving a metallic object close to the dielectric material. However, continuous tuning cannot be achieved since the quality factor degrades which degrades the phase noise performance of the oscillator. Frequency tuning can also be achieved by using an electronic phase shifter network incorporating varactor diodes inside the oscillation loop to produce a voltage controlled oscillator (VCO). By varying the capacitance of the varactor using a DC voltage, the resonance is moved and the frequency is changed and the oscillator would still operate as long as the total phase shift is Nx360°. The change in the phase shift in an oscillator changes the loaded Q of the resonator which is proportional to $d\phi/d\omega$. This also changes the resonator insertion loss which alters the amplifier gain and hence the circulating power in the loop. All these alterations degrade the phase noise of the oscillator and the research group at University of York has shown, both theoretical and experimentally, that the phase noise performance degrades with a $\mathrm{Cos}^4\phi$ relationship. This type of network produces 6dB degradation in phase noise at the 3dB points of the resonator (±45°) at which point the oscillator is tuned to $\pm f_0/2Q_L$. Typically to maintain low phase noise at all tuning points the oscillator is tuned to ±20° [11] [41]. Hence the electronic phase shifter needs to have a low insertion loss in the given tuning range in order to reduce the total noise figure of the system. It also needs to have a desirable phase shift in the tuning range but also have linear properties with respect to power and the control voltage. Also, since the varactor diodes are nonlinear semiconductor devices, they

should exhibit low residual phase noise since it would have effect on the overall performance of the oscillator.

3.5.1 Topology and Design

There are a number of ways to design an electronic phase shift using varactor diodes and the most common way is to design as in case of a reflection type phase shifter (RTPS). The total phase shift using this topology is usually +360° but they usually have a high insertion loss with respect to the change in the bias voltage which is undesirable in case of an oscillator [42] [43] [44]. Hence to maintain a low insertion loss in the pass band, a phase shifter presented in [45] was used which consisted of a 5^{th} order high pass Butterworth filter where the capacitors were replaced with varactor diodes. The choice of the cut off frequency determines the insertion loss and the phase shift. In case of a low cut off frequency, the parasitics of the varactors increases and hence the insertion loss and therefore minimum phase shift is achieved. In case of the high cut off frequency, this might be close to the frequency of operation, as we change the control voltage, the cut off frequency moves towards the operational frequency causing higher insertion loss. Hence the cut off frequency was set to Kxf where K was set to 0.6 from previous optimization and f is the frequency of oscillation [45].

The basic circuit for the phase shifter consists of a high pass filter based on a 5^{th} order Butterworth filter prototype with the two series capacitors replaced with varactor diodes and the capacitance is changed with the control voltage. The three shunt inductors are replaced with short lengths of high impedance transmission line for high frequency circuits. This circuit also enables varactor control from a voltage source. There are four stages in the design of the phase shifter:

a. Obtain the low pass filter prototype values.

b. Convert these values to a high pass topology.

c. De-normalize for the desired cut off frequency and impedance.

d. Convert the inductance to micro strip line equivalents.

The component values for the low pass prototype for a normalised 5th order Butterworth filter are: C1 & C2 = 0.618F; C3 = 2F; L1 & L2 = 1.618H and the schematic is shown in **Figure 3.22**.

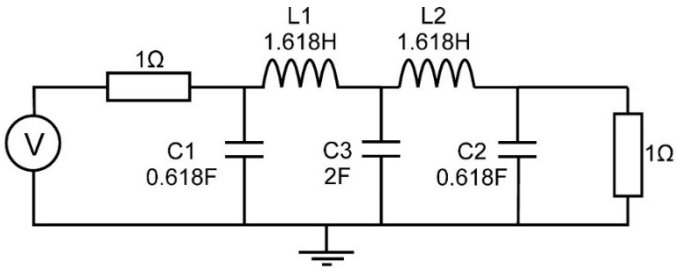

Figure 3.22: Low Pass Prototype for a 5th order Butterworth filter.

These low pass filter prototype values can now be de-normalised and converted to a high pass filter suing **Eq. 3.7** and **Eq. 3.8**.

$$C'_k = \frac{1}{Z_o \, L_k \, \omega_c} \qquad \textbf{Eq. 3.7}$$

$$L'_k = \frac{Z_o}{C_k \omega_c} \qquad \textbf{Eq. 3.8}$$

So for Z_0=50Ω, and for a cut off frequency, f_C of 2.4GHz which is ~0.6 of the operating frequency for optimum performance and the high pass prototype is shown in **Figure 3.23** calculated using **Eq. 3.9**, **Eq. 3.10** and **Eq. 3.11**.

$$L_1 = L_2 = \frac{Z_o}{C_k \omega_c} = \frac{50}{(2\pi \times 2.4 \times 10^9 \times 0.618)} = 5.36\, nH \qquad \textbf{Eq. 3.9}$$

$$L_3 = \frac{Z_o}{C_k \omega_c} = \frac{50}{(2\pi \times 2.4 \times 10^9 \times 2)} = 1.65\, nH \qquad \textbf{Eq. 3.10}$$

$$C_1 = C_2 = \frac{1}{Z_o\, L_k\, \omega_c} = \frac{1}{50\,(2\pi \times\ 2.4 \times\ 10^9 \times\ 1.618)} = 0.819\, pF \qquad \textbf{Eq. 3.11}$$

The high pass prototype for the 5th order prototype is shown in **Figure 3.23**.

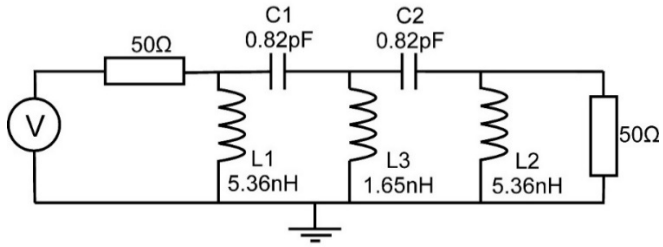

Figure 3.23: High pass 5th order Butterworth schematic for a cut off frequency of 2.28GHz.

As we are operating over a narrow tuning range, it is possible to replace the inductor with a high impedance line (Z_0) then we can obtain the equivalent length of line for the required inductance. This is the impedance for a transmission line terminated in a short circuit and is given by **Eq. 3.12**. Also, the capacitors are replaced by varactor diodes and as the reverse bias voltage applied to the diodes is increased, capacitance varies from $C_{MAXIMUM}$ to $C_{MINIMUM}$ and hence changing the phase shift.

$$j\omega L = jZ_0 tan(\beta l) \qquad \textbf{Eq. 3.12}$$

The high impedance for the inductor was chosen to be 85Ω as the width of the transmission line was easy to fabricate in house using Rogers 3006 substrate. For Z_0=85Ω and f=3.8GHz and L3=1.65 nH and the length of the transmission line was l=2.52mm and similarly L1 & L2=5.36nH, l=5.602mm was calculated using **Eq.**

3.12. The component values for the voltage controlled phase shifter are shown in **Table 3.4** for a cut off frequency of 2.28GHz. It should be noted that the length of the transmission line for the inductors was calculated at frequency of oscillation and not at the cut off frequency.

Table 3.4: Voltage controlled phase shifter values for a cut off frequency of 2.28GHz.

Component	Low Pass prototype	High Pass Equivalent	Micro-strip Length
L1 , L2	0.618F	5.36nH	5.602mm
C1 , C2	1.618H	0.82pF	-
L3	2.000F	1.65nH	2.520mm

Based on this design a varactor diode needs to be selected with a centre capacitance around 0.82pF. In this instance the MA46H series of varactor diodes from MA-COM were investigated and the MA46H070 was chosen. Unfortunately, there was no SPICE model available for these varactors and therefore one was developed as shown in **Figure 4.2**. The package has a parasitic capacitance of C_p = 0.15 pF, inductance of L_s =0.5nH from the data sheet. The capacitance C_v is calculated based on **Eq. 3.13**.

$$C_v = \frac{C_j}{\left(1 + \frac{V_r}{V_{JC}}\right)^{\gamma}} \qquad \textbf{Eq. 3.13}$$

Where the exponent γ was given to be around 0.75 in the datasheet, V_{JC} was taken as 0.7V and C_j (2.2pf) was calculated from the information that the diode has a value of 0.7pf at 4V. The diode series resistance ($r_s = 1.4\Omega$) was calculated from a Q of 4500 at 50MHz.

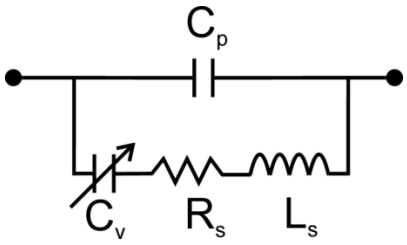

Figure 3.24: Equivalent model of the MA46H070 varactor diodes.

Based on this information, the varactor capacitance was modelled by simulating the S parameters. The bias voltage was varied and the capacitance was calculated using Z_C=-$j/\omega C$. The simulated and the values form the data sheet for the MA46H070 capacitance vs voltage graph (calculated at 1MHz) is shown in **Figure 3.25** for 0.1V-20V.

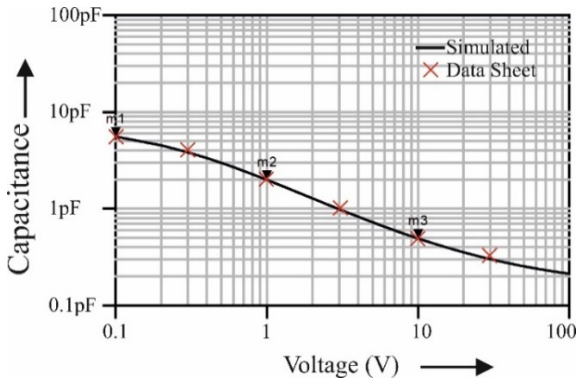

Figure 3.25: Comparison of the Capacitance Vs Voltage for MH46HO70 varactor diodes.

The schematic of the phase shifter incorporating the transmission line models for the inductors and the MH46HO70 varactor diodes is shown in **Figure 3.26**. The lengths of the transmission lines for the inductors were optmised using momentum in ADS and imported in ADS to run a co-simulation along with the model for the varactor.

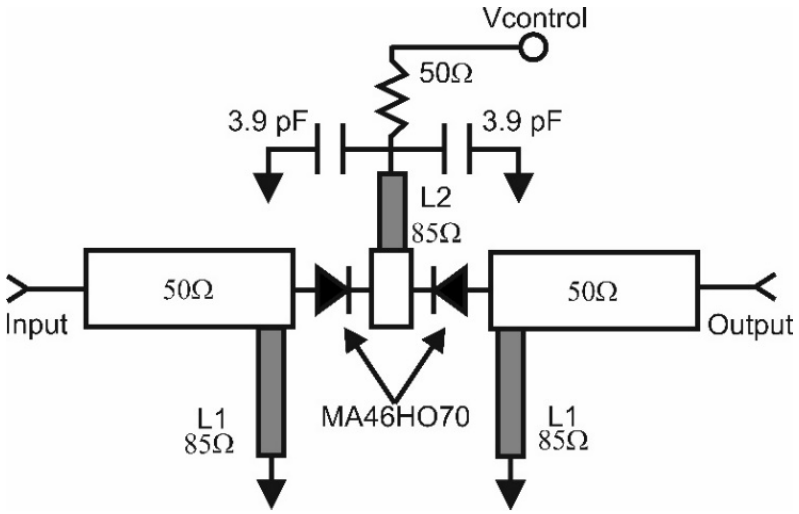

Figure 3.26: Schematic of the electronic phase shifter incorporating the transmission line models for the inductors and the MH46HO70 varactor diodes.

The entire phase shifter was simulated using the transmission line models for the inductors and the models for the varactor didoes using Agilent ADS for its S parameters and the frequency response is shown in **Figure 3.27** . The insertion loss *(S_{21})* is 0.2dB at 3.8GHz with a cut off frequency of 2.28GHz. The voltage on the varactor diodes was at 4V since the capacitance from the simulation was close to 0.88pF. Next, the insertion loss vs bias voltage shows the variation of the phase with respect to the bias voltage shown in **Figure 3.28**. It can be seen that it provides a tuning range of about 50° from 5V to 20V. The simulated insertion loss *(S_{21})* is 0.2dB for the same voltage range.

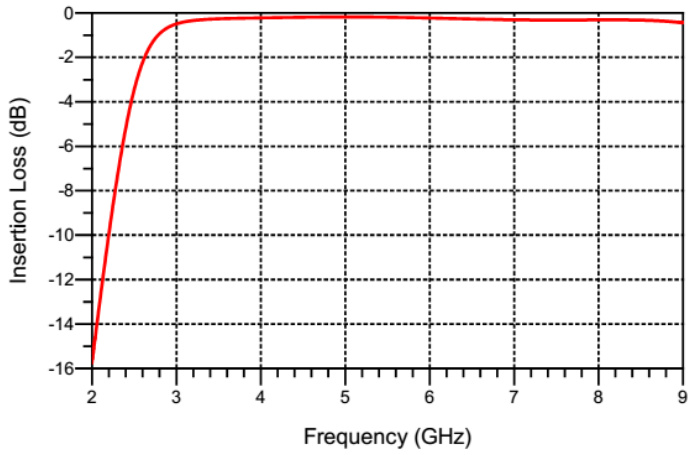

Figure 3.27: Simulated S Parameters for the phase shifter for a 5th order filter using varactor diode model and inductors replaced by transmission lines.

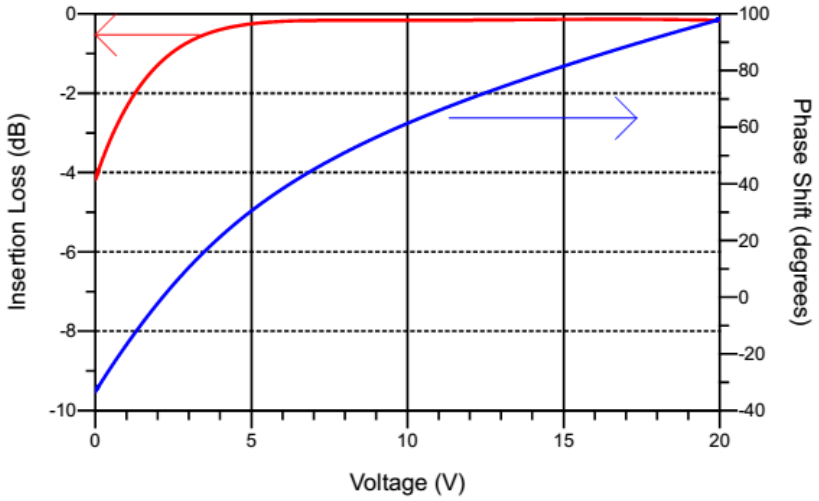

Figure 3.28: Simulation of the Insertion loss & Phase Response vs Bias Voltage using MH46HO70 varactor diodes.

In this current configuration, the electronic phase shifter is directly connected to the input of the push pull amplifier and coupler combination so a direct measurement is not possible. In order to obtain the response of the phase shifter, the measurement of the electronic phase shifter, amplifier and the coupler has to be

performed. The gain of the Amplifier which includes the Phase Shifter + Coupler vs Bias Voltage is shown in **Figure 3.29**. The gain varies by 1.2 dB for 5-20V where as there is a linear change in the phase shift from 5-20V providing 60° of phase shift. This measurement is similar to the simulated result shown in **Figure 3.28**. Measurements are accomplished using a network analyser to display the magnitude and phase of the forward transmission scattering parameter, (S_{21}) where variable DC power supply is used to provide the bias voltage. Note that in the second prototype described in section 3.9, all the elements of the oscillator including the phase shifter can be measured separately.

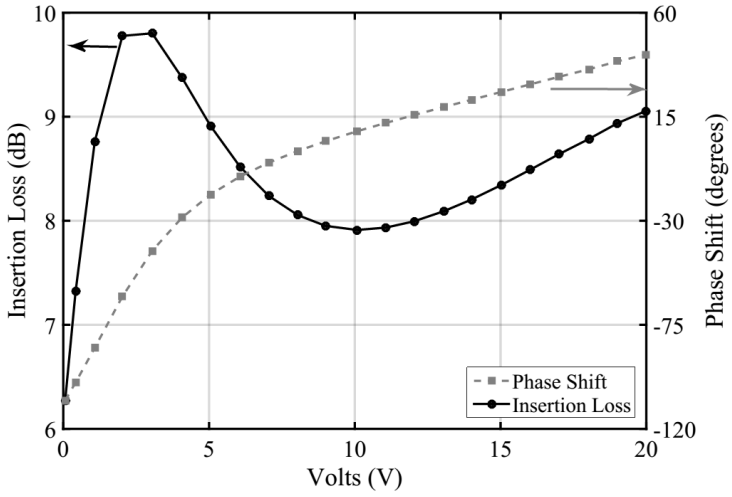

Figure 3.29: Amplifier+ Phase Shifter+ Coupler Gain and the Phase Response Vs Bias Voltage.

3.6 Multi Section Single Layer Coupler

A coupler was designed in order to integrate the oscillator to any external device. Power can be coupled from one transmission line to another which is in close

proximity due to the interaction of the electromagnetic fields. However, at microwave frequencies it is currently not possible to design a single section with a coupling of 10dB as the gaps between the lines would be too small with the current fabrication techniques at the University of York (current tolerance of 50 μm). The gap has to be around $30\mu m$ to achieve a coupling of 10dB at 3.8GHz. A multi section coupler has therefore been designed using the techniques described in [46].

In this design as seen in **Figure 3.30** the coupler consists of parallel lines which are ($\lambda_g/4$) in length are used. These two single parallel lines have a slightly lower coupling ratio and hence higher impedances. If these coupled lines are connected directly to each other no coupling is achieved since the total phase shift is 90° and they are out of phase. Hence they are connected with a 50Ω line which is also ($\lambda_g/4$) in length which adds the signals in phase and higher coupling can be achieved.

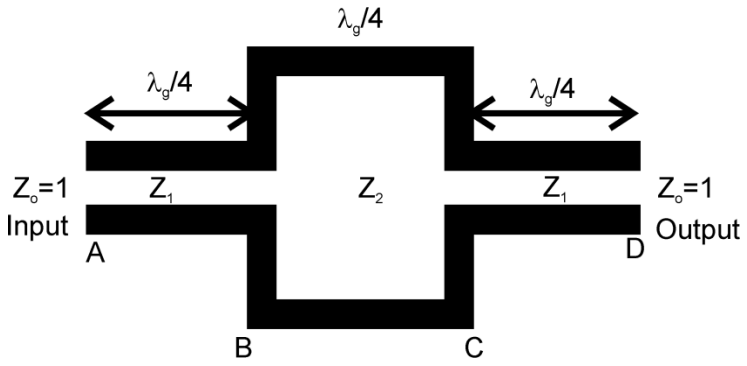

Figure 3.30: Multi Section single layer 10-dB directional coupler.

The various impedances of the directional coupler terminated at Z_0=1Ω (normalised) is shown in **Figure 3.30**. The coupling ratio is determined as follows: At point D, the total impedance seen by the circuit (Z_D) is its characteristic impedance which is 1Ω. At point C, which is ($\lambda_g/4$) away from the D, the impedance (Z_C) seen by the circuit is (Z_1^2). Now at point B, the impedance (Z_B) which is again

($\lambda_g/4$) from C, is (Z_2^2/Z_1^2) and finally at A. $Z_A = (Z_1^2)/(Z_2^2/Z_1^2) = (Z_1^4/Z_2^2)$. Hence the total reflection coefficient (Γ_{in}) is:

$$C_1 = \Gamma_{in} = \frac{Z_1^4 - 1}{Z_1^4 + 1} \qquad \textbf{Eq. 3.14}$$

$$z_1 = \left(\frac{1 + C}{1 - C}\right)^{\frac{1}{4}} \qquad \textbf{Eq. 3.15}$$

$$C = \frac{Z_1^2 - 1}{Z_1^2 + 1} \qquad \textbf{Eq. 3.16}$$

For a 10 dB coupler, c=-10dB therefore $C=10^{-10/20}=0.316$. Using **Eq. 3.15** we get $Z_1=1.177\Omega$ and substituting this in **Eq. 3.16** we get a coupling ratio of 0.16 which is -15.8dB coupling and then de-normalising we get a impedance of $Z_1=Z_3=58.88\Omega$.

The design was simulated and optimised for its correct electrical lengths using Momentum in Agilent ADS for various impedance transmission lines. The design consists of a cascade of two quarter wave coupled lines (with a coupling of -15.8dB) with a quarter wave delay line between them. This is illustrated in **Figure 3.31**. The first and the third sections (which are used for coupling) have an impedance of 58.88Ω and the middle section is 50Ω impedance. This centre section is used to set the correct phase shift and is not used for coupling.

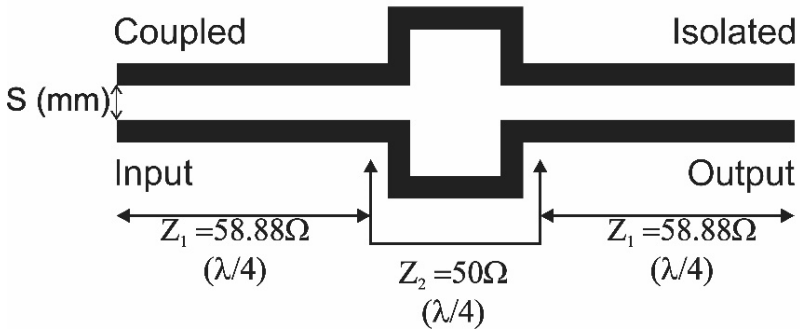

Figure 3.31: Impedances for the multi section 10dB directional coupler.

It was found that the spacing is very critical and small changes affect the bandwidth and the coupling ratio of the coupler as shown in **Figure 3.32** for various spacing of 0.35mm, 0.45mm and 0.5mm. The optimum spacing between the lines was found to be 0.45mm using Momentum. All the sections are ($\lambda_g/4$) in length. The simulations suggested a -10.3dB coupling and a loss of 0.6dB at the through port 3.8GHz for a spacing of 0.45mm and also as the spacing between the lines changes, the coupling starts to decrease faster.

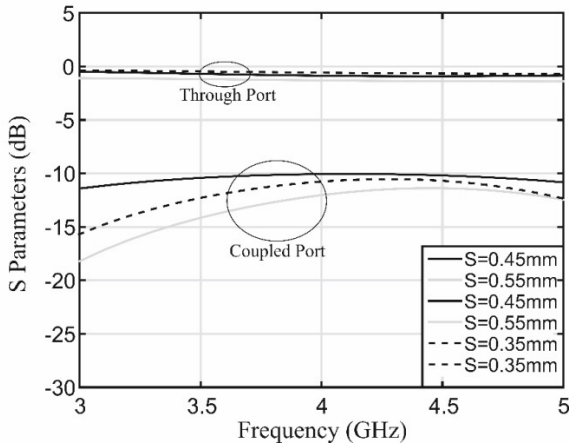

Figure 3.32: Momentum simulation of the 10 dB multi section direction coupler for spacing of 0.35, 0.45 and 0.5 mm.

Table 3.5 shows the final dimensions of the lines before and after optimisation using Momentum in ADS.

Table 3.5: Initial and final dimensions of the multi-section Coupler

Transmission line Impedance	Width (mm)	Length ($\lambda_g/4$) (mm)
58.88Ω	0.63	Initial value: 8.12 Optimised value: 8.86
50Ω	0.88	8.73

The coupler is directly connected to the output of the push pull amplifier and phase shifter combination so a direct measurement is not possible and hence to obtain the response of the coupler alone two measurements are required. The left hand response **Figure 3.33** is the measured response of the Phase Shifter + Amplifier + Coupler taken at the output port and the measured response of the Phase Shifter + Amplifier + Coupler from the Coupled Port is shown on the right hand side in **Figure 3.33**. The difference demonstrates a coupling of approximately 10dB, as expected.

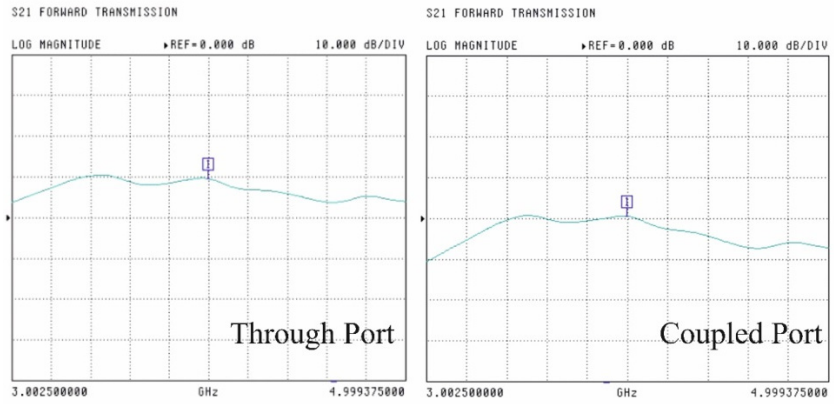

Figure 3.33 Measured Phase Shifter + Amplifier + Coupler responses from 3-5GHz.

The first DRO mounted on the baseplate was enclosed in a screened metal box to remove spurious signals and the second oscillator was fully enclosed in its own box and the pictures of the DRO's are shown in **Figure 3.34** and **Figure 3.35**.

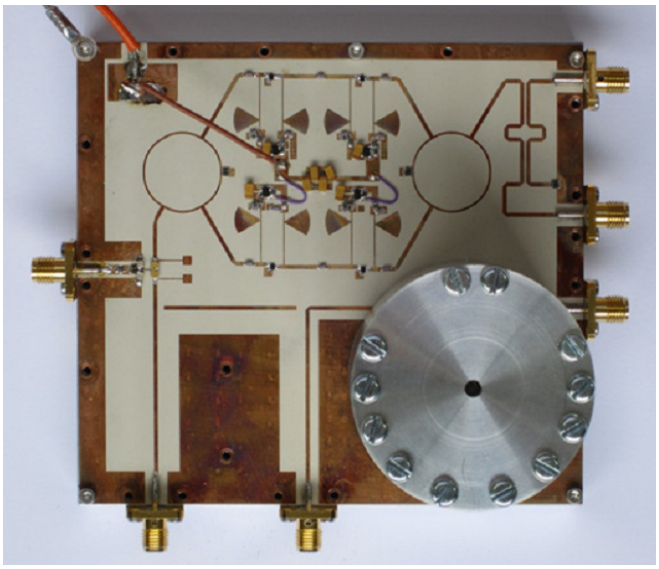

Figure 3.34: Oscillator 1 mounted on the baseplate with a separate resonator enclosure.

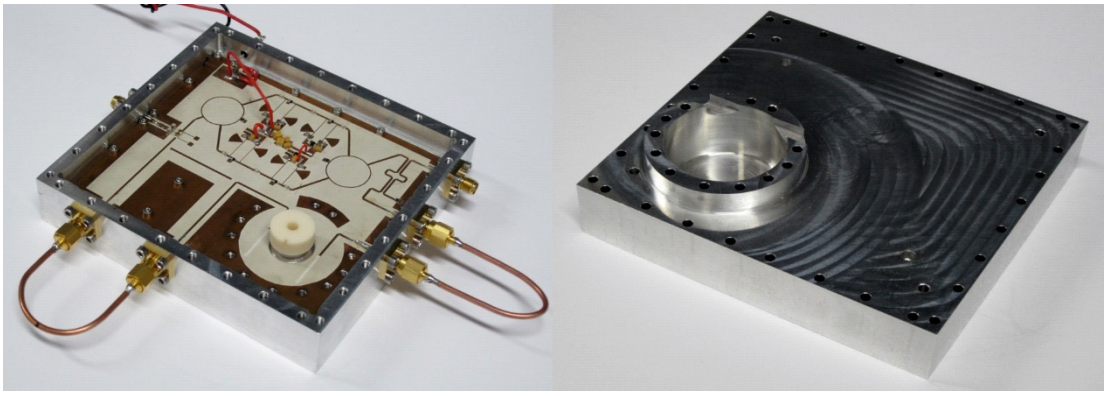

Figure 3.35: Oscillator 2 which measures 125×115×40mm is completely enclosed in its box.

3.7 Phase Noise Measurements

The phase noise of these oscillators is significantly lower than any commercial phase noise measurement systems. It is therefore necessary to mix two oscillators and

measure a low frequency beat signal and hence the two oscillators, DRO1 and DRO2 are mixed using a mixer; ZEM-4300MH as shown in **Figure 3.36**. This produces a down converted signal of 3.5MHz. The phase noise of this signal was measured using a Symmetricom 5120A opt 01 phase noise analyser. Two isolators were initially used for the measurements but later they were removed and the same results were obtained. A low pass filter (DC- 11MHz) was used to remove the higher order harmonics at the input of the Symmetricom 5120A.

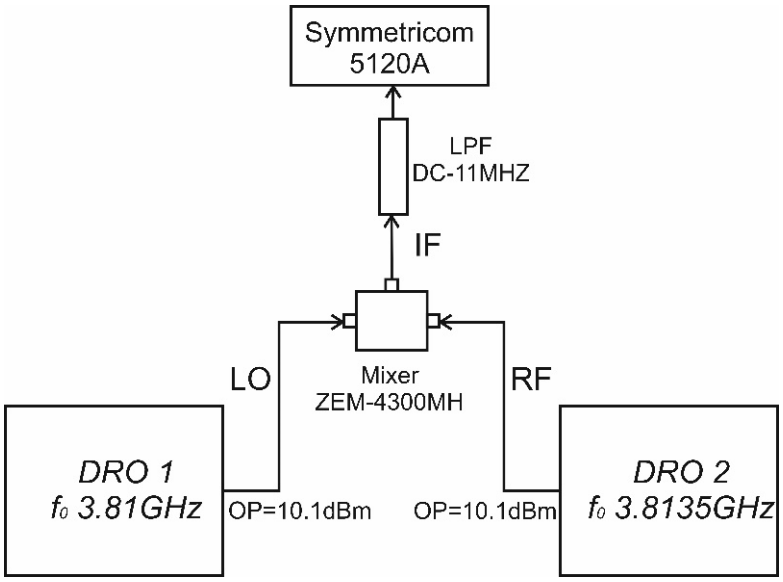

Figure 3.36: Phase Noise Measurement System used to measure the phase noise of the oscillators.

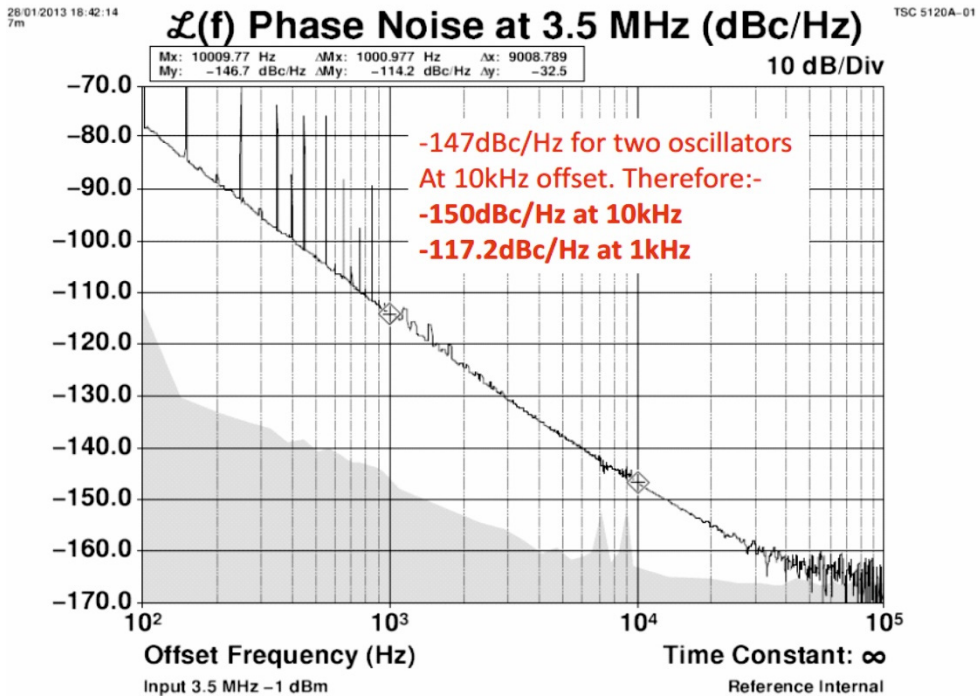

Figure 3.37: Phase Noise Measurement Plot of the 3.8GHz oscillators which demonstrate a phase noise of -150dBc/Hz at 10kHz offset.

The phase noise measurement plot displayed in **Figure 3.37** is 3dB lower. This is because two identical oscillators have been mixed together in order to produce the result and hence it therefore necessary to subtract 3dB from the measured value. The spurs at the lower frequency can be removed by operating the bias, the supply voltages using bias boxes and batteries. The theoretical phase noise of an oscillator is calculated using **Eq. 3.17** and the parameters values used for the calculation of the theoretical phase noise of the oscillator:

T: The room temperature in Kelvin T = 293 K

F_A*:* The Noise Figure of the amplifier, phase shifter and the coupler, measured to be 4 dB.

Q_L: loaded Q of the resonator = 7675

Q_0: Un-loaded Q of the resonator = 19,829

P_{AVO}: Power available at the resonator = 20dBm

f_o: frequency of oscillation, 3.81GHz.

f_c: Flicker Frequency, assumed to be 10kHz.

Δf: Offset frequency

$$L(f) = 20\log_{10}\left[\frac{F_1 kT}{2C_0P_1} + \frac{F_A kT\left(1+\frac{f_c}{f}\right)}{2P_{AVO}}\left[\frac{1}{\left(1-\frac{Q_L}{Q_0}\right)^2}\right] + \frac{F_A kT}{8(Q_0)^2\left(\frac{Q_L}{Q_0}\right)^2\left(1-\frac{Q_L}{Q_0}\right)^2 P_{AVO}}\left(\frac{f_0}{f}\right)^2\left(1+\frac{f_c}{f}\right)\right] \quad \textbf{Eq. 3.17}$$

Table 3.6: Compassion of the theory with that of measurement of the oscillators at 3.8GHz for a noise figure of 4dB and a flicker noise corner assumed to be 10kHz or higher.

Offset	Theory	Measurement
1kHz	-128.8 dBc/Hz	-117.2 dBc/Hz
10kHz	-156.8 dBc/Hz	-150.0 dBc/Hz

Table 3.6 shows the comparison of the theoretical phase noise with that of the measurements assuming the flicker noise corner of 10kHz and noise figure of 4dB which includes the cables, phase shifter and the coupler. The measurements are 8-10dB worse when compared to that of the theory. The degradation in phase noise may be explained as a result of increase in the noise figure when the amplifier is under saturation. Hence residual phase noise measurements would be needed in order

to measure the noise figure when the amplifier is under saturation and also the flicker noise corner. In the present design, the amplifier, electronic phase shifter and the output coupler are connected together and hence it is not possible to measure the flicker corner frequency and the noise figure under large signal conditions. So a new prototype was built (explained in section 3.9) where all the individual elements of the oscillator can be built and measured independently.

Finally, measurements were performed for the Frequency tuning vs Bias voltage where the amplifier supply was kept at V_{CC} of 6 V as seen in **Figure 3.38**. This measurement demonstrates the frequency tuning range which can be obtained using the voltage controlled phase shifter. The voltage controlled phase shifter was adjusted in 1 volt increments and the frequency of the new peak recorded. The phase shift tuning is nonlinear with respect to the tuning voltage and hence as we change voltage on the phase shifter, the insertion loss and the loaded Q changes which in turn changes the circulating power in the loop non-linearly degrading the phase noise of the oscillators. In the new prototype, a better power handling capability (explained in section 3.9.3) was built in order to reduce the non-linearity.

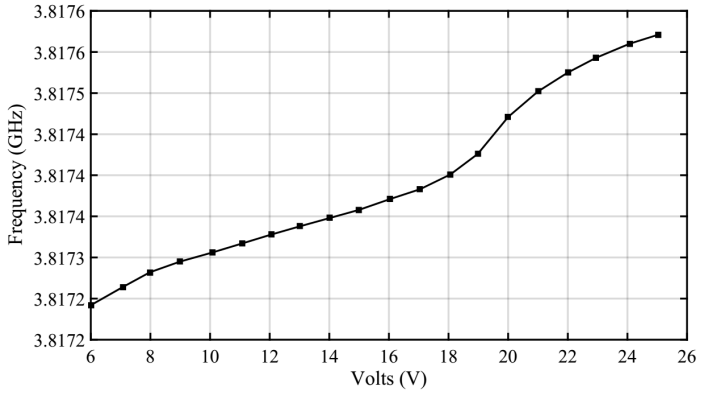

Figure 3.38: Tuning Frequency vs Bias Voltage for the 3.8GHz oscillator.

3.8 Vibration Measurements

One of the main aims of this initial work was to measure the vibration sensitivity *(Γ_i)* of the dielectric resonator oscillator to understand how the phase noise of the oscillator degrades with vibrations. In order to measure the sensitivity, the oscillator needs to be characterized while subjected to vibrations. The basic measurement setup needed to have a mechanical actuator or a shaker in order to induce vibrations and an accelerometer to sense these vibrations. The final set of vibration measurements for different vibration profiles were performed at Selex-ES which had sophisticated vibration measurement systems. However, to obtain initial estimates of the vibration sensitivity some initial measurements were performed at University of York.

3.8.1 Initial Vibration Measurements at University of York

First, it was necessary to develop excitation methods to induce vibrations. Two methods were used. DC vibration motors which are commonly used in mobile phones for vibrations were available which produce sinusoidal vibrations at around 120Hz with a peak g around 0.5g. The oscillator is mounted on a plate supported by pieces of string. The vibration motor is placed under the metal plate and the accelerometer is bonded to the oscillator. The second method was a loudspeaker cone. A signal generator was used to vary the frequency and the amplitude of the oscillations. The frequency of oscillation was set to 120Hz so as to compare the results with the DC motor but with a different peak acceleration *'a_i'*. The oscillator was made to rest on the top of the loud speaker and the accelerometer was mounted on the side of the oscillator. The measurement system for both the setups is shown in **Figure 3.39**.

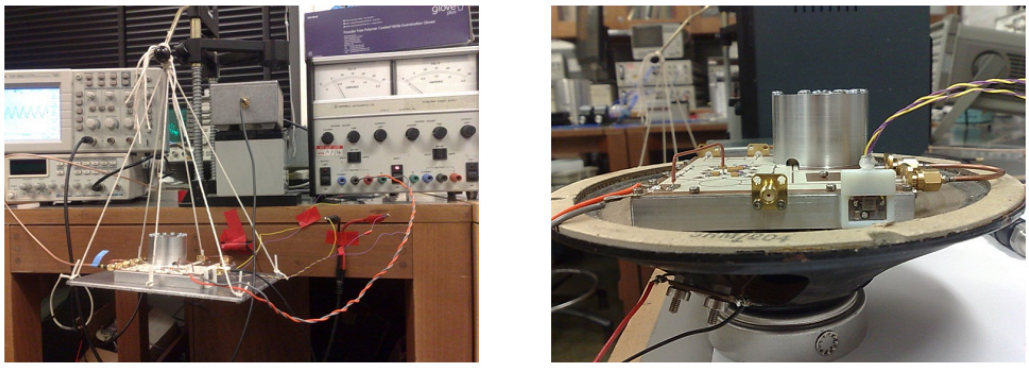

Figure 3.39: Spot frequency vibration measurement setup for the 3.8GHz oscillators using DC motors and loud speakers.

Next, in order to sense the peak acceleration which is exhibited on the oscillators, it was necessary to obtain some accelerometers. The ADXL-203CE from Analog Devices was used which is a dual-axis accelerometer which can measure acceleration up to ±1.7g from DC to 3 kHz. This can operate from 3 to 5 V. The total current consumption is 1.1mA. According to the data sheet, the vibration sensitivity is 1000mV/g at 5V and 560mV/g at 3V [47]. A CR-2032 Li-ion battery (3V) was used to power the accelerometer. The accelerometer was mounted on a small PCB measuring about 15mm square as shown in **Figure 3.40**. One advantage of these sensors is that they can be calibrated directly at DC by measuring the voltage change in each axis by turning them upside down. The change in voltage is equal to 2g. Care was taken that lights and other electronic devices were switched off in the room to remove any unwanted pickups.

The vibration sensitivity (Γ_i) for a given peak acceleration a_i in the X axis is calculated by **Eq. 3.18**:

$$\Gamma_i = \frac{2f_v}{a_i f_0} 10^{\left(\frac{L(f_v)}{20}\right)} \Gamma_i \qquad \textbf{Eq. 3.18}$$

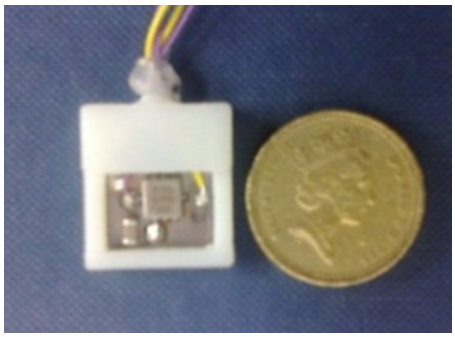

Figure 3.40: Photograph of the dual axes accelerometer ADXL-203CE used for measuring the peak acceleration.

A DC Vibration Motor was used to produce vibrations at 120Hz. The side bands were measured to be $L(f_v)$=-23.3 dBc and the accelerometer output voltage was 240mV therefore *'a_i'* is 240/560 = 0.42g. Therefore, the vibration sensitivity for the DC motor was 1.164 x 10^{-8} g^{-1} in the X axis. For a second measurement a loud speaker was used, again at 120Hz, as the exciter. The side bands were measured to be $L(f_v)$=-33.3 dBc, the *'a_i'* measured was to be 0.14g as seen in **Figure 3.41**. Therefore, the vibration sensitivity is 1.092 x 10^{-8} g^{-1} in the X axis.

Figure 3.41: Sidebands seen on a spectrum analyser due to vibrations at 120Hz for a_i=0.14g.

3.8.2 Final Vibration Measurements at Selex-ES

Next for more accurate measurements for various vibration profiles, measurements were performed at Selex-ES. The Oscillator was rigidly mounted on a vibration table with accelerometers. Next a set of spot frequency vibrations at various frequencies and random vibration profile was used on the oscillators to measure the vibration sensitivity. Precautions have to be taken care of when measuring the acceleration sensitivity of the DUT as mentioned by Hati el al. [21]. The oscillators were rigidly mounted on the vibration table in order to avoid any mechanical resonance from the box and since there were cables which connected the oscillators to the phase noise instrument and power leads associated with the experiment, all the cables were secured to the ground to dampen any effects of the vibrations. Also, there were no other components attached on the vibration table apart from the accelerometers. Before the start of the vibration measurements, a phase noise measurement was done under the vibration measurement setup in order to verify the phase noise measurement results with that of the ones done at University of York.

3.8.2.1 Spot frequency

The dielectric resonator oscillator which was enclosed in its own box was used for the spot frequency vibrations which were similar to the measurements performed at University of York; however, the measurements at Selex-ES were performed for all the axes. Sine wave vibrations were applied at three different frequencies 100Hz, 500Hz and 1500Hz at an intensity of $a_i = 0.2$g and the measurement setup is shown in **Figure 3.42**. The induced sideband levels, $L(f_v)$, were then measured as shown in **Figure 3.43** and based on this the vibration sensitivity was calculated at these fixed frequencies for all the three axes using **Eq. 3.18**.

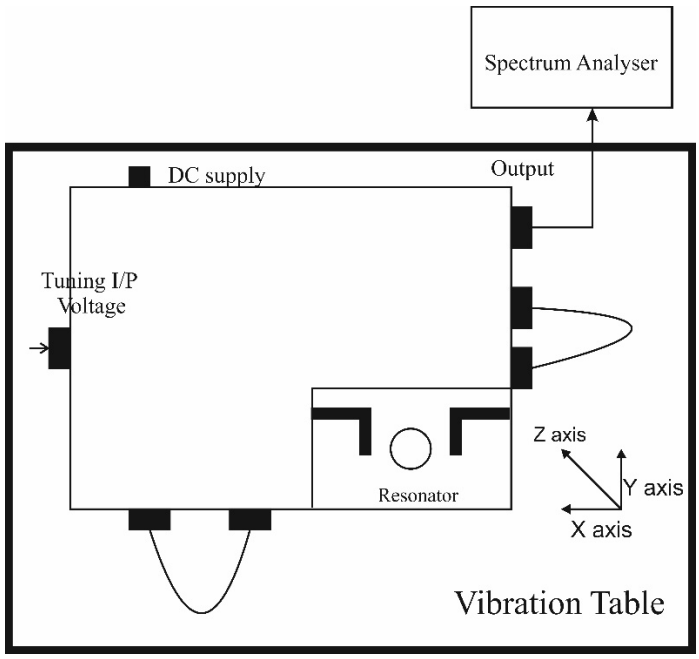

Figure 3.42: Measurement setup for the spot frequency profile at 100Hz, 500Hz and 1500Hz at an intensity of $a_i = 0.2$g.

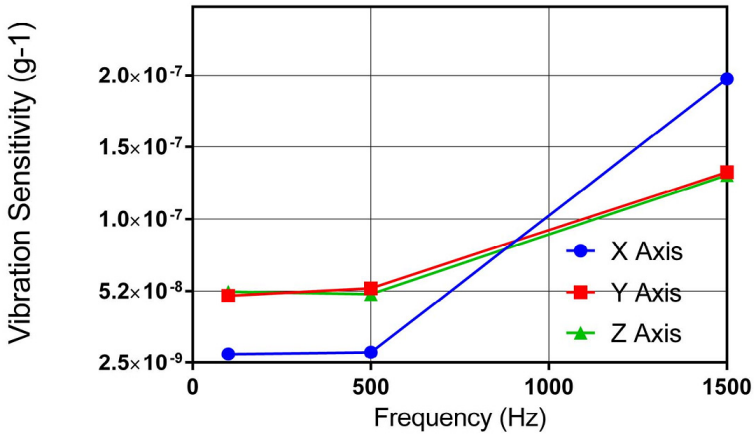

Figure 3.43: Vibration Sensitivity in X, Y, Z axes at 100Hz, 500Hz, and 1.5kHz.

At lower frequency, the Y and the Z axis have larger vibration sensitivity compared to that of the X axis. This may be due to a number of factors.

Firstly, the semi-rigid cables which are used in the oscillator are not ideal. Ideally, most of the components should be printed on the PCB in order to reduce any effects of vibrations on the oscillator. Secondly, the resonator was mounted on an aluminium base in order to improve the quality factor and hence improve the performance of the oscillator. It can be also seen that, the measurements performed at York (120Hz) were similar in vibration sensitivity measurements performed at Selex-ES (100Hz) on the X axis. The FSUP spectrum analyser plots showing the induced sideband levels $L(f_v)$ caused by vibration on the X, Y and the Z axis are shown in Appendix A.1. It has to be noted that correlation of these spot frequency measurements needs more investigation.

Table 3.7: Vibration Sensitivity for all the 3 axes at 0.2g at 100Hz, 500Hz and 1.5kHz

X Axis :

f	g	$L(f_v)$	Γ_i (g^{-1})
100 Hz	0.2	-29.80 dBc	8.51×10^{-9}
500 Hz	0.2	-42.64 dBc	9.70×10^{-9}
1500 Hz	0.2	-25.88 dBc	2.00×10^{-7}

Y Axis :

f	g	$L(f_v)$	Γ_i (g^{-1})
100 Hz	0.2	-14.56 dBc	4.92×10^{-8}
500 Hz	0.2	-27.66 dBc	5.44×10^{-8}
1500 Hz	0.2	-29.26 dBc	1.35×10^{-7}

Z Axis:

f	g	$L(f_v)$	Γ_i (g^{-1})
100 Hz	0.2	-14 dBc	5.2×10^{-8}
500 Hz	0.2	-28.33 dBc	5.04×10^{-8}
1500 Hz	0.2	-29.44 dBc	1.33×10^{-7}

3.8.2.2 Random Vibration Profile

DRO 1 was mounted on the vibration table and the output was connected to the Mixer ZEM-4300MH. DRO 2 was mounted away from the table in a screened box and the output was connected to the LO port of the mixer. Both signals were then down converted to 3.5MHz. A low pass filter was used to remove the higher harmonics. A Rohde & Schwarz FSUP was used to measure the side bands as well as the phase noise measurements. A Symmetricom 5120A opt 01 was also used to verify the phase noise measurements with those from the FSUP. Batteries were used to reduce the lower frequency spurs. Care was taken when performing the vibration measurements. The oscillator was rigidly mounted on the vibration table with an accelerometer and no other components were mounted on the vibration table. The semi rigid cables which were used in the oscillators were set to the correct torque. Also, the cables which were used to connect to the output of the oscillators to the Symmetricom 5120A and the FSUP were secured to the floor to reduce the tension on the cables. The vibration axes of the oscillator are defined showing the relationship between X, Y and Z axes to the resonator mounting as shown in **Figure 3.44**.

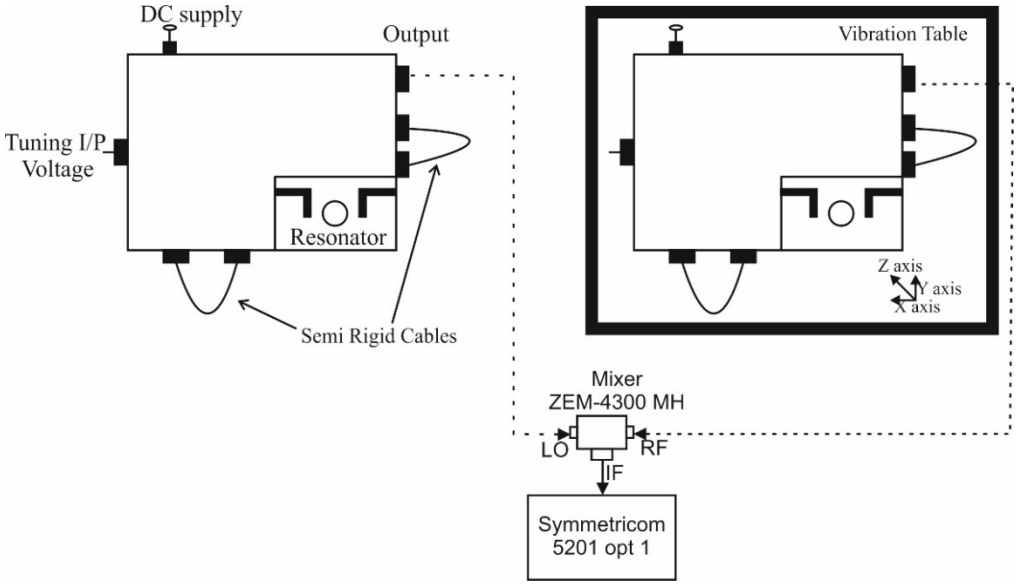

Figure 3.44: Vibration Measurement phase noise setup with the reference of vibrations axes.

A second test applied a random vibration profile *(10Hz–2kHz)* with a total vibration of 0.7g rms on all the 3 axes. A phase noise measurement was carried out during this test. A random vibration profile of acceleration 0.7g (rms) is used for 10Hz ≤ f_v ≤ 2000 Hz as shown in **Figure 3.45**. It shows the variation in the close to carrier noise for three different axes with that of the phase noise with no vibrations. At 1kHz, the phase noise varies from -112.56 dBc/Hz with no vibrations to -64.11 dBc/Hz in the X axis, -51.08 dBc/Hz in Y Axis and -51.16 dBc/Hz in the Z axis for 0.7g rms. Far away from carrier around 50kHz the phase noise of the Y and Z plots merge with reference signal.

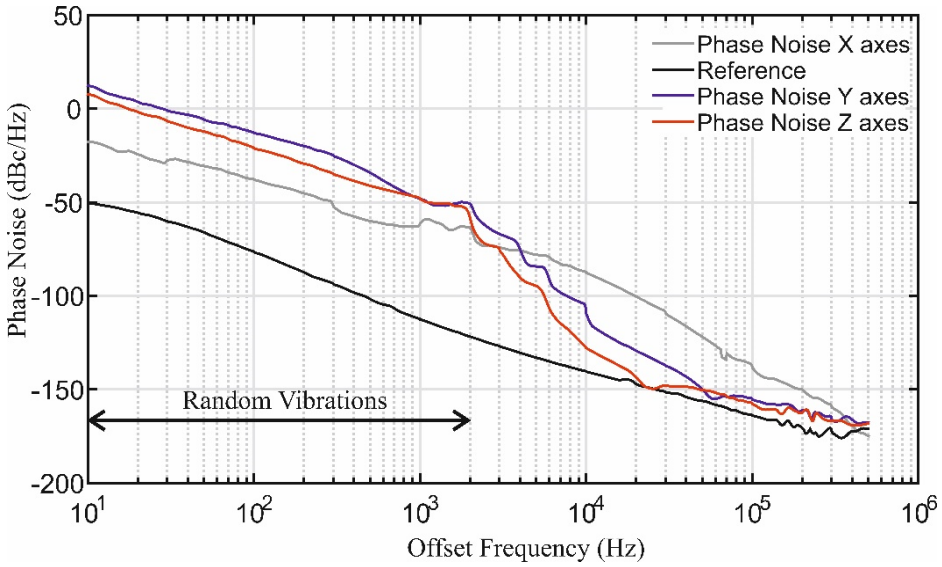

Figure 3.45: Comparison of the Phase Noise Plots for different axes for random vibration profile with 0.7g rms.

The bottom curve shows the noise floor of the oscillators measured under no vibrations. There are a number of reasons for the vibration sensitivity to be in order of 10^{-7}. The vibration effects may due to the semi rigid cables which were used to get the phase shift right around the loop and secondly due to mounting of the resonator on spacer in order to increase the quality factor. The sensitivity can further be improved by having a single board with the right phase shift around the loop. It is believed that the vibration sensitivity on these oscillators can be further improved by placing the puck directly on the PCB board but this comes at an expense of the phase noise performance. However, when the puck is directly mounted on the PCB board, the simulated Q is reduces to 1600 from 7675 and the phase noise of the oscillators degrades to -134.4 dBc/Hz at 10kHz offset.

3.9 New Improved Oscillator Prototype

A 6dB improvement in the phase noise is potentially possible if the noise figure is reduced and the output power is increased in the oscillator. Hence a new oscillator was built using the same feedback topology as shown in **Figure 3.46** to improve the phase noise performance. The new prototype of the oscillator was built in such a way that the individual elements can be built and measured separately and then linked directly with each other to form the oscillator. A mechanical phase shifter was included in the new prototype to make it more compact and reduce the noise figure and to remove the semi rigid cables. PCB boards were fabricated using Rogers 3006 ($\mathcal{E}$r=6.50, tanδ= 0.0020) for the amplifier, coupler, resonator and the mechanical phase shifter while Rogers 4003C ($\mathcal{E}_r$=3.55, tanδ=0.0027) [48] [49]was used for the electronic phase shifter due to limitation of the width of the transmission lines during the manufacturing process of the PCB boards as shown in **Figure 3.47**.

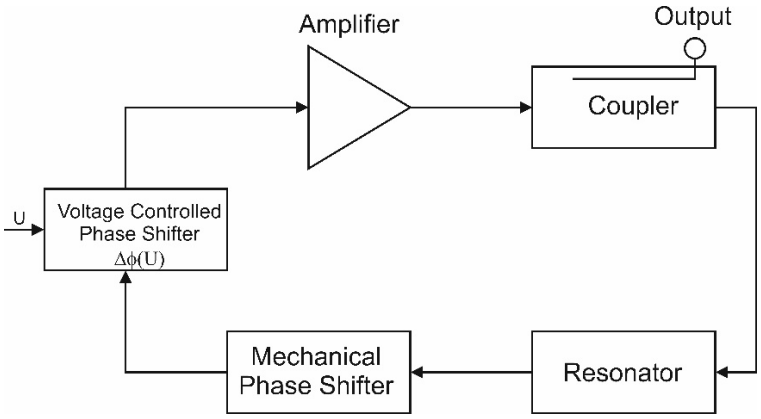

Figure 3.46: Modular 3.8GHz oscillator with an incorporated mechanical phase shifter.

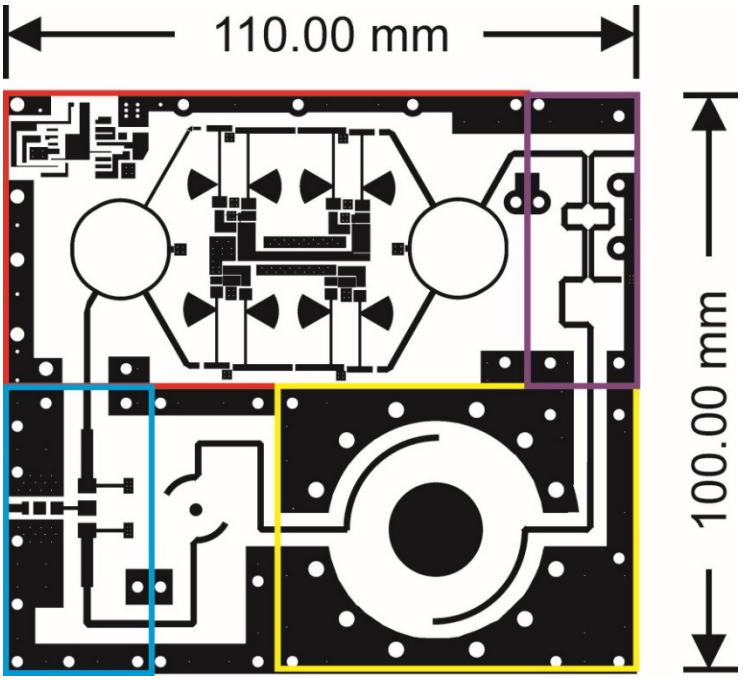

Figure 3.47: Modular yet compact 3.8GHz Oscillator Board incorporating the mechanical phase shifter.

3.9.1 Push Pull Amplifier

The design of the Push Pull Amplifier is similar to the one mentioned in section **3.3** using the SiGe BFP380F transistors from Infineon. The amplifier was simulated for its gain, noise figure and the output power compression point. The Push Pull amplifier demonstrated a gain of 10.2dB with an input return loss of -11.2 dB at 3.8GHz. The comparison of the gain and the input return loss for the simulated amplifier with that of the measurements is shown in **Figure 3.48**. The noise figure was measured to be 4dB at 3.8GHz using the double side band technique.

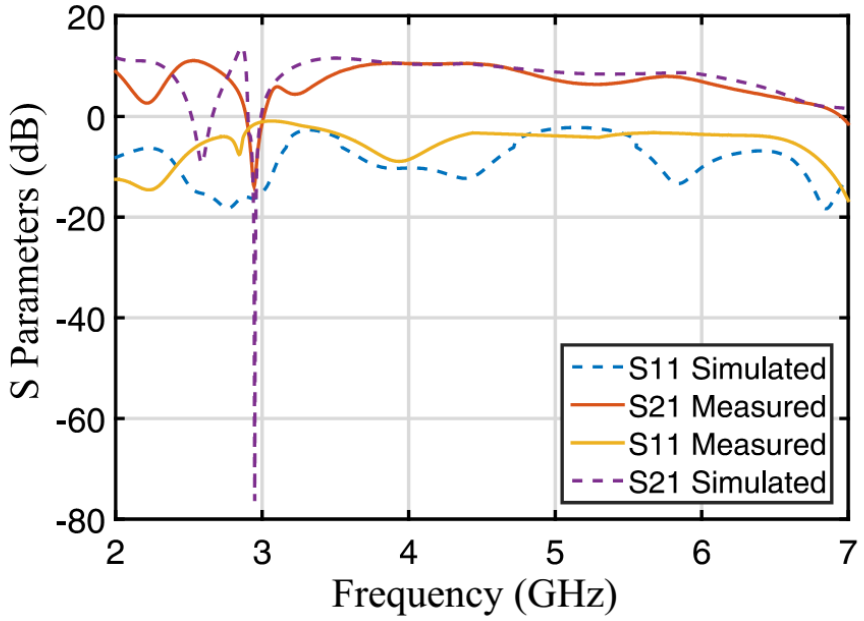

Figure 3.48: Comparison of the simulated and the measured S parameters of the Push pull amplifier.

Next, the output compression point was measured using the setup shown in **Figure 3.49**. A signal generator at 3.8GHz was used at the input followed by a directional coupler in order to accurately measure the input power. An attenuator was used at the output to protect the power meter. **Figure 3.50** shows the comparison of the simulation and the measurement of the P_1dBm compression point. The output compression point was measured to be at 20.1 dBm which was in agreement with the simulated of 20 dBm at 3.8GHz using the harmonic balance simulation using the SPICE model for the transistor in ADS.

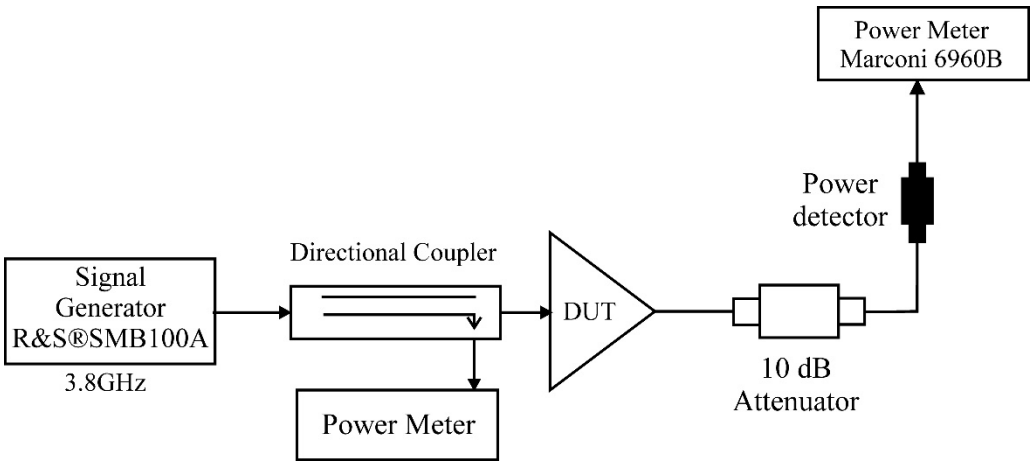

Figure 3.49: Power Measurement Setup for the Push Pull Amplifier using the SiGe BFP380F transistors.

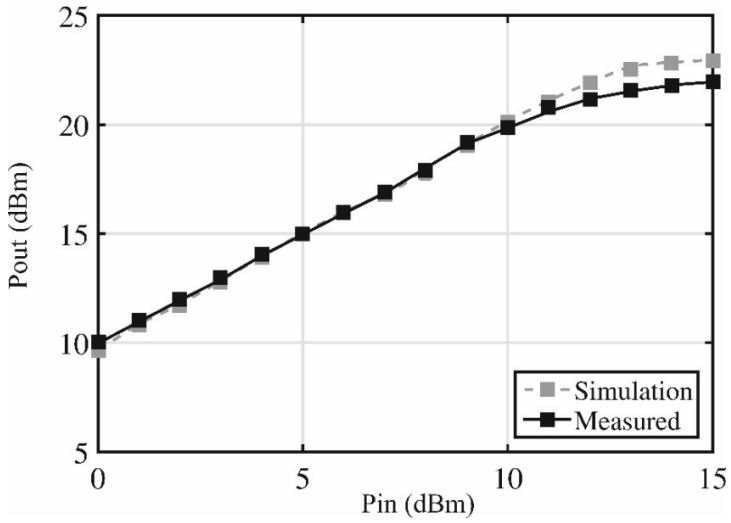

Figure 3.50: Simulated and the measured 1-dB compression point for the Push Pull amplifier.

3.9.2 Dielectric Resonator

Since the dielectric puck used in the previous prototype was bonded on an aluminium base and bolted from the below, it could be swapped easily and hence the same dielectric puck could be used. A new structure using symmetrical transmission lines was simulated using CST Microwave Studio. The top view, perspective and the dielectric resonator along with its enclosure is shown in **Figure 3.51**.

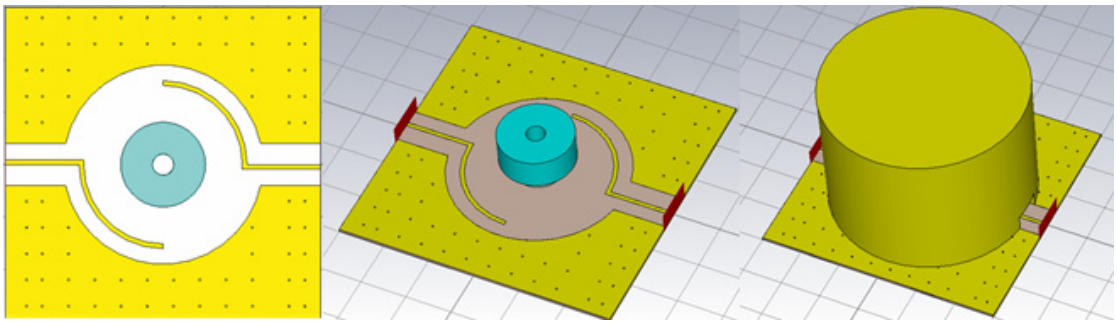

Figure 3.51: CST model of the Symmetrical Curved transmission lines.

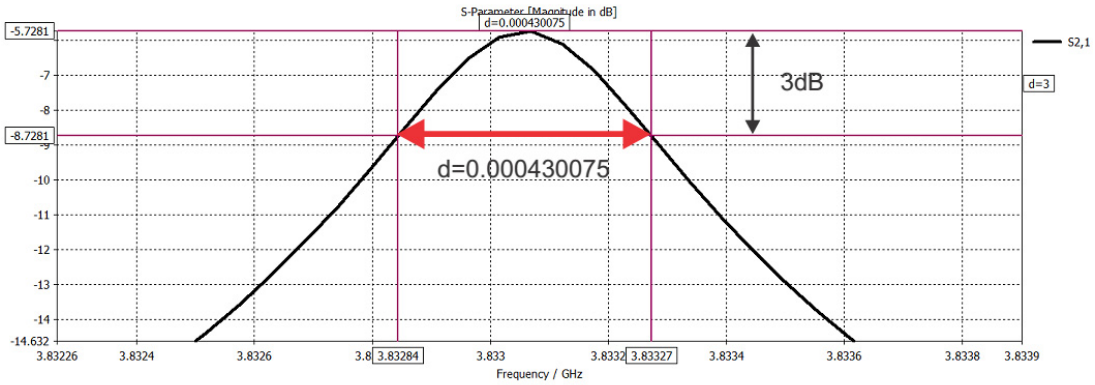

Figure 3.52: Simulated response of the resonator with an insertion loss (S_{21}) of -5.7 dB and 3-dB band width of 0.43kHz resulting in a (Q_L) of 8,860 usingCST.

The insertion loss was simulated to be -5.7 dB with a simulated loaded Q of 8860 as shown in **Figure 3.52**. A new board was fabricated where the transmission lines were symmetrical and hence a new enclosure was also built for the same as shown in **Figure 3.53**. Also, to achieve fine tuning, a screw was inserted on the top of the enclosure in order to change the magnetic fields inside the resonator and hence the frequency. The insertion loss for a span of 6 GHz is shown in **Figure 3.54**. The required TE_{011} mode can be seen along with unwanted higher frequency spurs. Also, there are no lower order modes and the insertion loss at 3.81GHz is -21.28 dB since there is not enough number of points. The closest spur is at a frequency of around 575MHz higher than the TE_{01} mode.

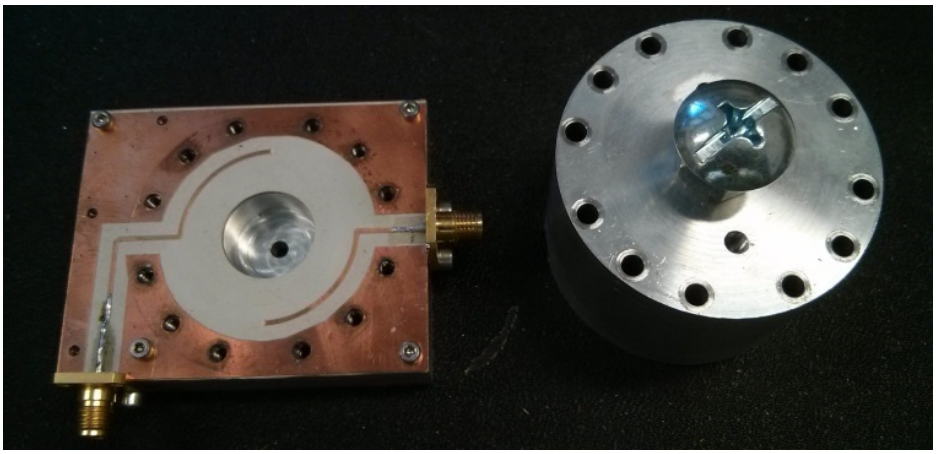

Figure 3.53: Symmetrical probes for the resonator along with the enclosure for 3.8GHz dielectric resonator.

The span was reduced to 10MHz and the insertion loss and the loaded Q was recorded. The insertion loss is -6.7dB and the loaded Q was measured to be 10,570 shown in **Figure 3.55** which results in an unloaded Q of 19,660 calculated using **Eq. 3.6**.

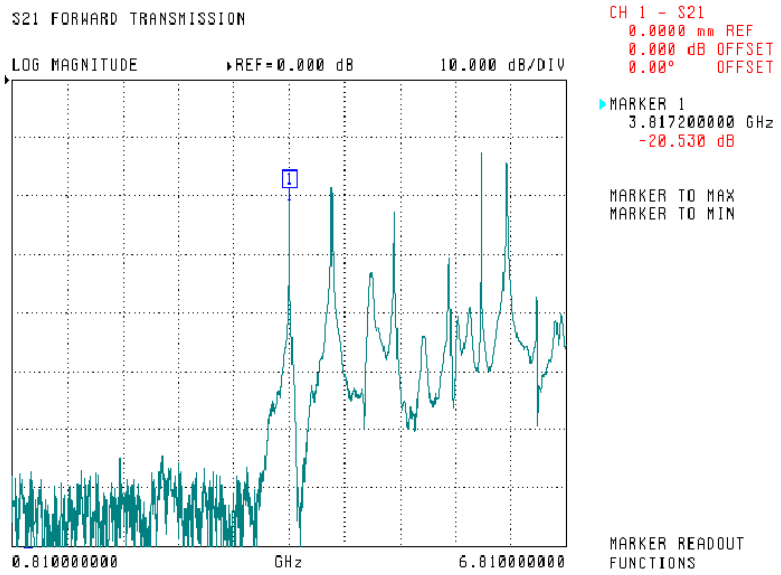

Figure 3.54: Measured insertion loss of the resonator for a span of 6GHz.

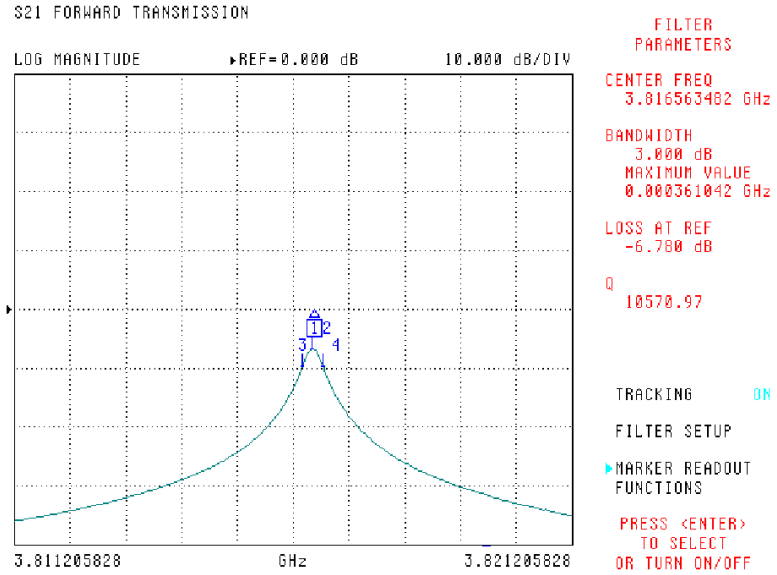

Figure 3.55: Measured insertion loss of the resonator for a span of 10MHz with a loaded Q of 10,570.

3.9.3 New Improved Electronic Phase Shifter

The phase shifter developed in the previous prototype exhibited nonlinear effects during frequency tuning at certain DC voltages as seen in **Figure 3.38** and hence a harmonic balance simulator was used in Agilent ADS to predict the non-linearity of the modelled MH46HO70 varactor diodes with respect to the input power for various bias voltages. Simulations suggested no non linearity up to 23dBm at all DC voltages, since the maximum power which was possible at the input of the electronic phase shifter was 20dBm. The device appears to be linear with respect to the power levels at any certain DC voltage. From the literature it is known that at certain RF voltages the varactor diodes exhibits negative conductance at a subharmonic frequency. This negative conductance cancels any losses in the circuit which results in a subharmonic frequency between the diode capacitance and the inductance of the circuit [50] [51]. As the voltage across the diodes is halved by reducing the system impedance from 50Ω to 25Ω the negative conductance needs higher input power to occur.

Hence a new 25Ω phase shifter was developed based on the 5^{th} order high pass filter prototype using the same procedure as the original phase shifter described in section **3.5**. A quarter wave transformer was used to transform the system impedance of 50Ω into 25Ω and because of this the voltage across the diodes was halved, the capactiance doubles and the inductors are halved. The new values of the capacitors are 1.64pF and the inductors L_1,L_2 is 2.68nH and L_3 is 0.825nH calculated using **Eq. 3.7** and **Eq. 3.8** for the 5^{th} order Butterworth high pass filter prototype. The capacitors are again replaced with varactor diodes from MA-COM which were used in the previous prototype. Since the value of capacitors doubles, two of the

MH46HO70 diodes were used in parallel to get a total capacitance of 1.64pF. The schematic for a new phase shifter is shown in **Figure 3.56**.

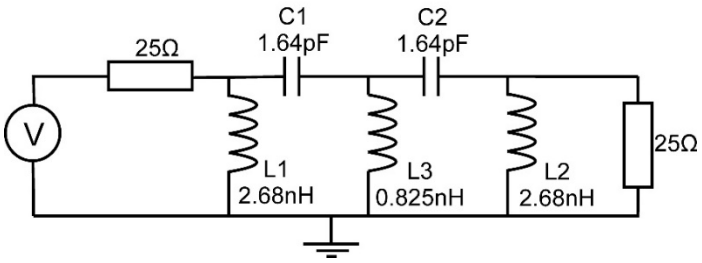

Figure 3.56: High pass filter prototype for a 25Ω system with a 2.28GHz cut off frequency.

L_1, L_2 and L_3 are the inductors which are now converted into tranmission lines using $j\omega l = jZ_0 tan(\beta l)$. The lengths *(l)* for the inductors are 5.39mm for L_1 and L_2 and 2.56mm for L_3 using a high impedance (85Ω) line with a width of 0.40mm using Rogers 4003C substrate. The quarter wavelength of the impedance transformer for a 35.35Ω line is ($\lambda_g/4$) 11.64mm to transform into a 25Ω system. The circuit diagram for a new phase shifter using the transmission line models for the inductors is shown in **Figure 3.57**.

The transmission lines were optimised in Momentum ADS and then the phase shifter was simulated for its frequency response. The frequency response for the high pass filter is shown in **Figure 3.58** with a cut off frequency of 2.4GHz. The simulated insertion loss at 3.8GHz was 0.88dB while the measured insertion loss *(S_{21})* was 1.45dB for a 10V control voltage as seen in **Figure 3.59**.

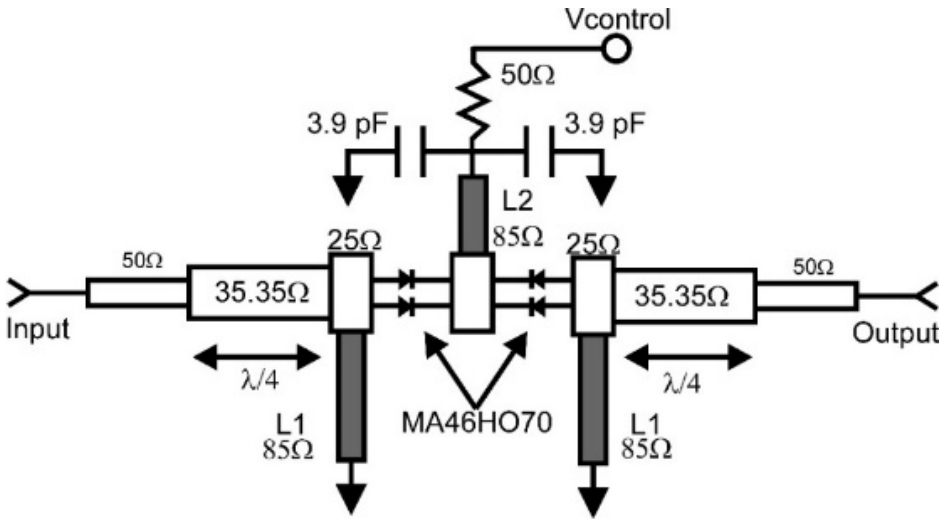

Figure 3.57: Electronic phase shifter using impedance transformer with the MH46HO70 varactor diodes.

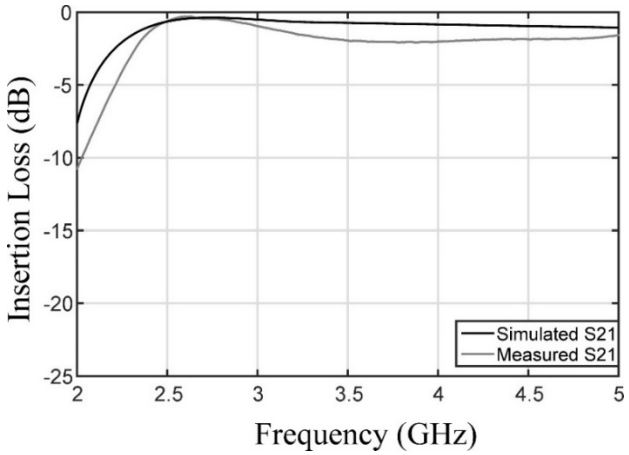

Figure 3.58: Comparison of the measurements and the simulation for the new modified electronic phase shifter.

Next, the measurement was performed to determine the variation of the insertion loss and the phase shift with respect to the control voltage. The simulation

suggests a constant insertion loss of about 0.3dB. The measured insertion loss (green line) varies by 0.3dB for 5V to 20V as shown in **Figure 3.59**. There is an almost a linear change in the phase shift (black line) from 5V to 20V providing 40° of phase shift. Measurements are accomplished using a network analyser to display the magnitude and phase of the forward transmission scattering parameter, *(S_{21})*. A variable DC power supply is used to provide the bias voltage.

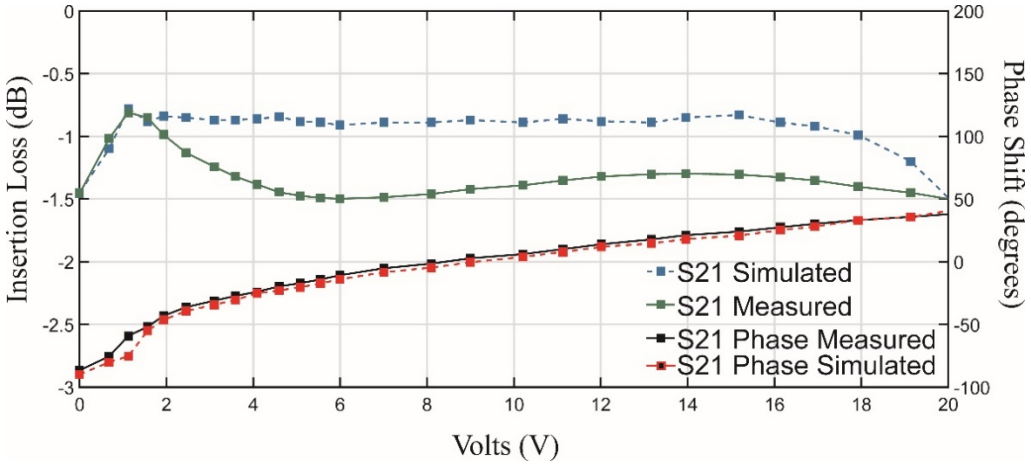

Figure 3.59: Simulated and measured Insertion Loss *(S_{21})* and phase shift (degrees) for the electronic phase shifter.

Next, two varactor diodes (one from each pair) was replaced by a fixed capacitor to see if there were any nonlinear effects on the phase shifter and the same set of measurements were conducted to see if the insertion loss remained constant over the voltage. As shown in **Figure 3.60** there is almost a constant insertion loss with respect to the control voltage from 5V to 20V for 0.8pF, 0.9pF, 1pF and 1.2pF. But the tuning ability of the phase shifter was reduced to 10° for the same control voltage when one of the varactor diodes was removed.

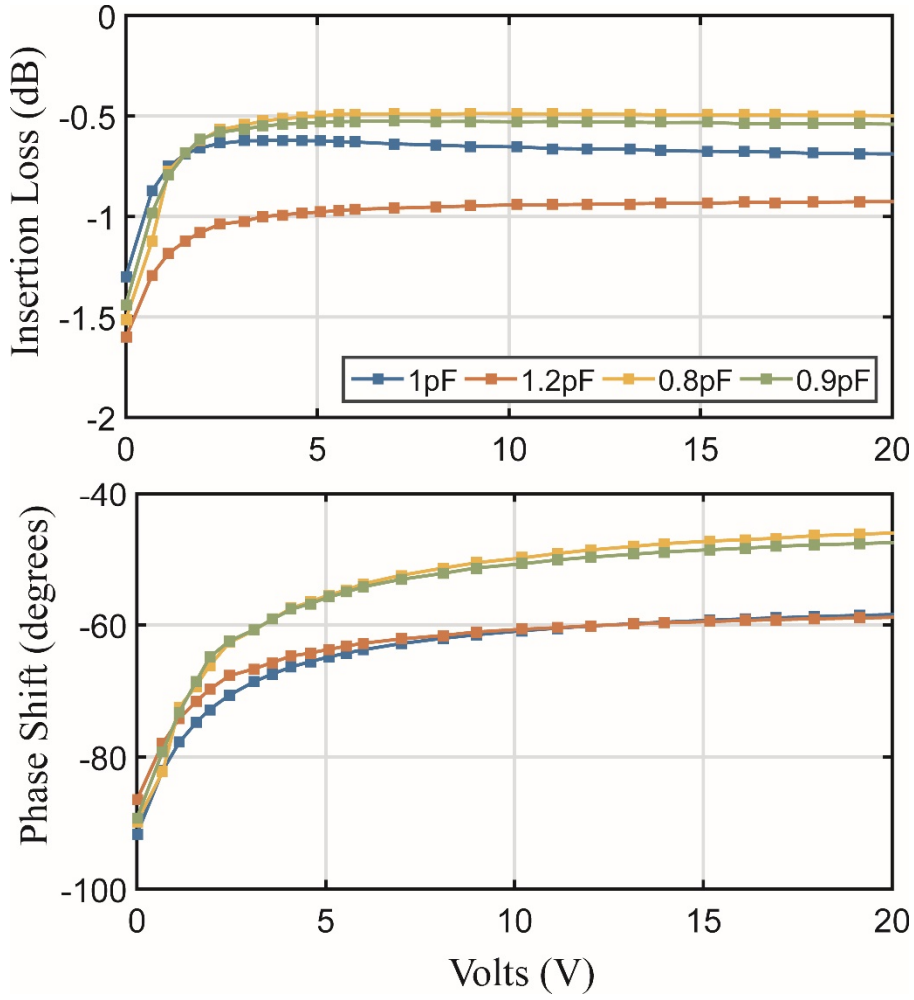

Figure 3.60: Measured Insertion Loss *(S_{21})* and Phase shift for various fixed value capacitors along with the varactor diode.

Finally, to see if there were any nonlinear effects on the phase shifter with respect to the input power, large signal measurements were done on the phase shifter. The input power was changed with a help of a tunable attenuator and the insertion loss and the phase shift were noted. The phase shifter did not exhibit any non-linearity with respect to the phase shift and the insertion loss up to maximum input power of 17dBm at 3.8GHz.

3.9.4 Multi Section Directional Coupler

In order to integrate external devices, a single layer multi section printed 10dB coupler has been designed and built similar to the design described in section **3.6**. The impedances were 58.88Ω and 50Ω and all the sections were (λg/4) and the spacing between the lines is 0.45 mm. The coupler demonstrated a loss of 0.6dB at the through port which connects to the resonator while the coupling was measured to be -9.9dB at 3.8GHz as shown in **Figure 3.61**.

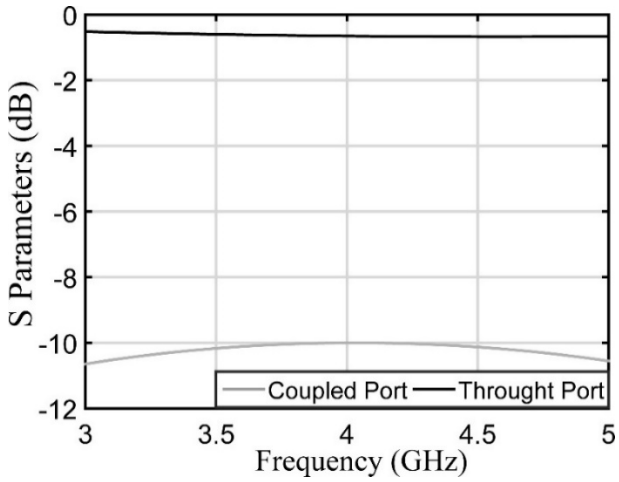

Figure 3.61: Measured Coupled and through port of the multi-section coupler for the 3.8GHz oscillator.

3.9.5 Mechanical Phase Shifter

The oscillator always oscillates at (N x 360°) and in the previous prototype the additional phase shift required was obtained by using semi rigid cables. However, the semi rigid cables increased the vibration sensitivity of the oscillators and added to the noise figure. Hence, in this prototype in order to get the phase shift correct in the loop, a compact mechanical phase shifter was developed. The design similar on

a compact mechanical phase shifter developed by Aeroflex [52]. The open loop phase shift is required to be accurate to <±1mm (10°/mm) for a Rogers 3006 with a ε_r =6.50 board [48] to achieve the required phase noise performance. The layout of the mechanical phase shifter consisting of the rotatable top section and the fixed bottom section is shown in **Figure 3.62**. Phase shift can be obtained just by rotating the top section and hence changing the length of the transmission lines. In the closed state, the top PCB board completely overlaps the bottom PCB providing a minimum phase shift and as we move the top PCB from a completely overlapped position, the length of the transmission line changes and hence the total phase shift. The top PCB which has a meander line has a total electrical length of 120°. A meander line was chosen for the top PCB board so that a screw can hold the PCB board onto a base plate and moved easily. The lengths of the lines were optimised using momentum in ADS to obtain a low insertion loss as well as the required phase shift.

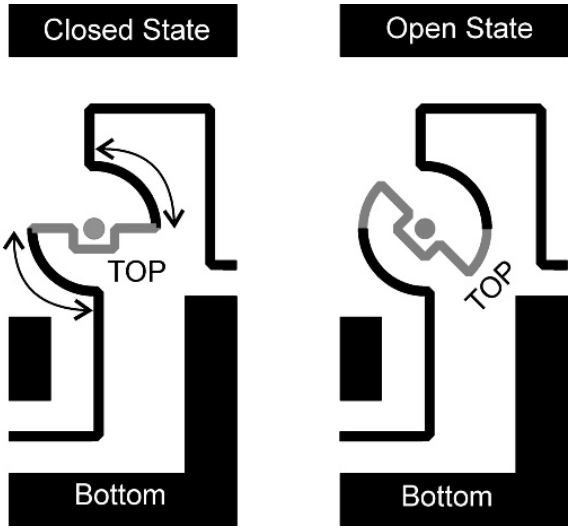

Figure 3.62: Illustrated layout of the mechanical phase shifter designed at 3.8GHz.

The top PCB board was rotated in steps of 10° and Agilent ADS Momentum was used to simulate for the entire structure for its total phase shift and the insertion

loss. The simulated insertion loss *(S_{21})* was 0.4dB at 3.8GHz for the closed state and 0.5dB for the open state while the total simulated phase shift was around 140° as shown in **Figure 3.63** while the total measured insertion loss varies from 0.4dB to 0.7dB from 3GHz to 5GHz.

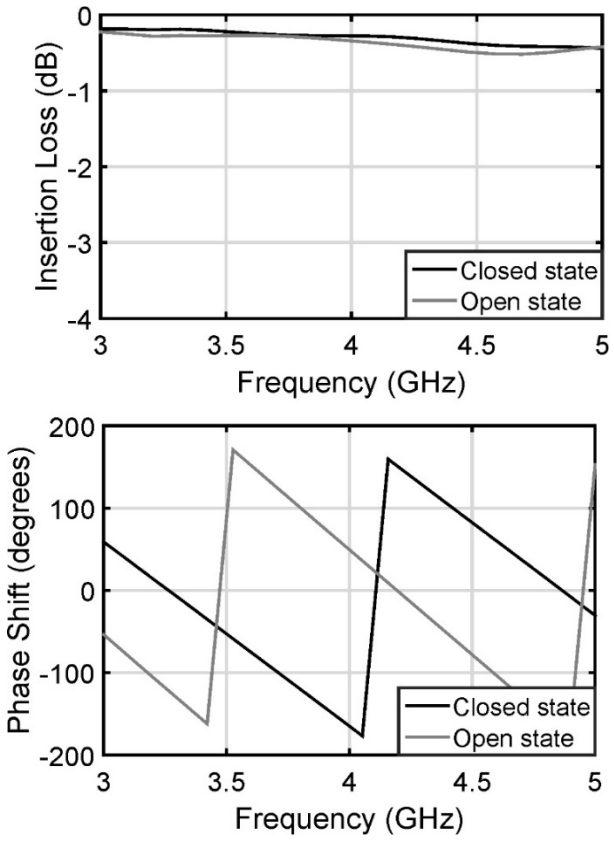

Figure 3.63: Momentum simulation of the insertion loss *(S_{21})* and the phase shift for the mechanical phase shifter for the closed and the open state.

The mechanical phase shifter consists of the top PCB and the bottom PCB board as shown in **Figure 3.64** and the two were connected using a nylon screw. The mechanical phase shifter was then tested for its insertion loss and the phase shift. The measured insertion loss *(S_{21})* varies from 0.7dB to 0.9dB from closed state to the open state providing a total phase shift of 116°.

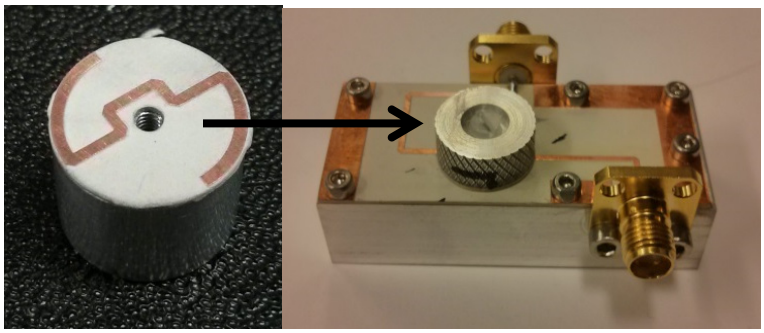

Figure 3.64: Compact low insertion loss mechanical phase shifter. The total phase shift measured was 116° at 3.8GHz.

3.9.6 Phase Noise Measurements

The first DRO made of these individual sections linked with each other were mounted on the baseplate which was enclosed in a screened metal box as shown in **Figure 3.65**. The second oscillator which also consisted of all the individual parts was linked with each other was fully enclosed in its own box as shown in **Figure 3.66**. It should be noted that all the individual parts can be measured separately making it a modular structure. Phase noise measurement is carried as described in section **3.7** using the beat frequency method. The two oscillators, DRO1 and DRO2 are mixed using a mixer; ZEM-4300MH. This produces a down converted signal of 1.9MHz. The phase noise of this signal was measured using a Symmetricom 5120A opt 01 phase noise analyser.

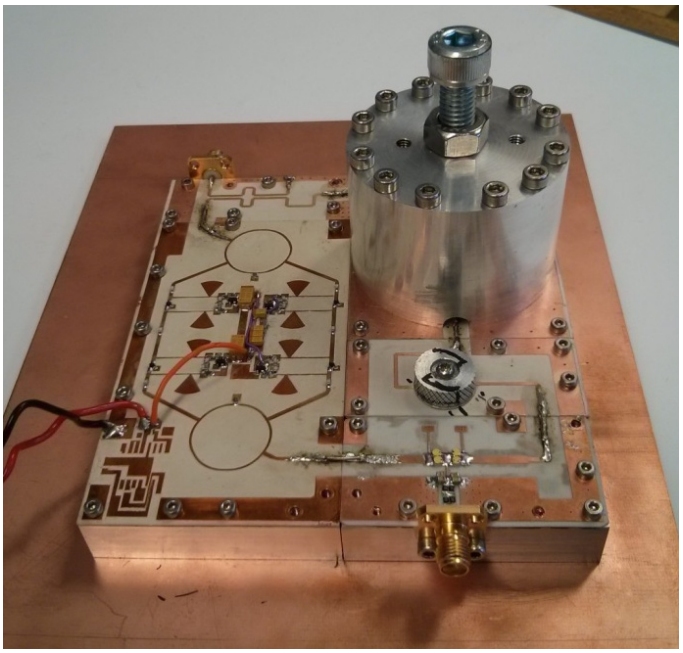

Figure 3.65: DRO 1 with individual sections linked with each other were mounted on the baseplate was enclosed in a screened metal box.

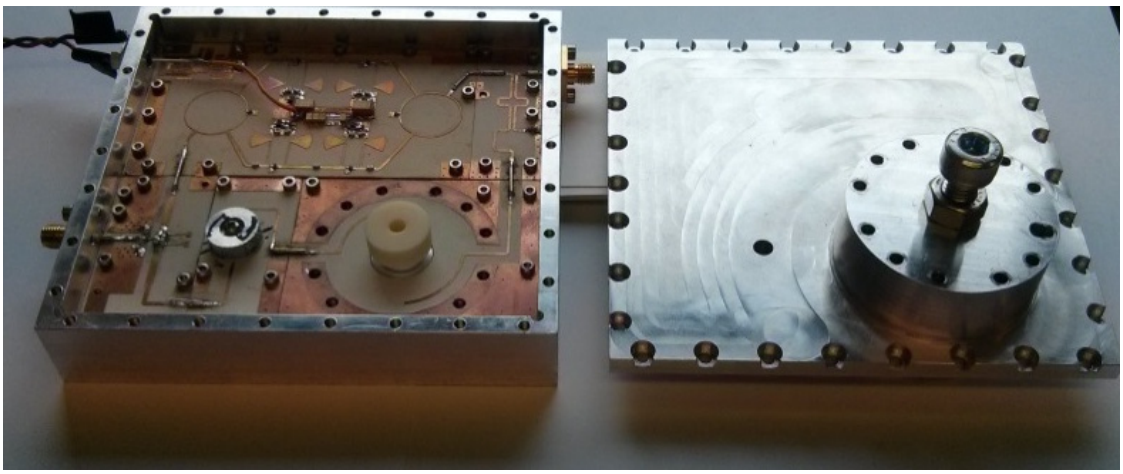

Figure 3.66: 3.8GHz oscillator with all the individual elements along with the enclosure on the right. The oscillator measures 120×110×35mm.

The phase noise equation for the oscillators is given by:

$$L(f) = 20\log_{10}\left[\frac{F_1 kT}{2C_0P_1} + \frac{F_A kT\left(1+\frac{f_c}{f}\right)}{2P_{AVO}}\left[\frac{1}{\left(1-\frac{Q_L}{Q_0}\right)^2}\right] + \frac{F_A kT}{8(Q_0)^2\left(\frac{Q_L}{Q_0}\right)^2\left(1-\frac{Q_L}{Q_0}\right)^2 P_{AVO}}\left(\frac{f_0}{f}\right)^2\left(1+\frac{f_c}{f}\right)\right] \quad \textbf{Eq. 3.19}$$

Where :

T: The room temperature in Kelvin T = 293 K

F_A*:* The total noise figure of the amplifier, phase shifter and the coupler, measured to be 5 dB. Note that the noise figure is shown to be 8dB under large signal conditions as explained in section 3.9.7

Q_L : Loaded Q of the resonator = 10,570

Q_0 : Un-loaded Q of the resonator = 19,660

P_{AVO}: Power available at the resonator = 19dBm

f_o: frequency of oscillation, 3.81GHz.

f_c: Flicker corner frequency, measured to be 12.7kHz.

Δf: Offset frequency

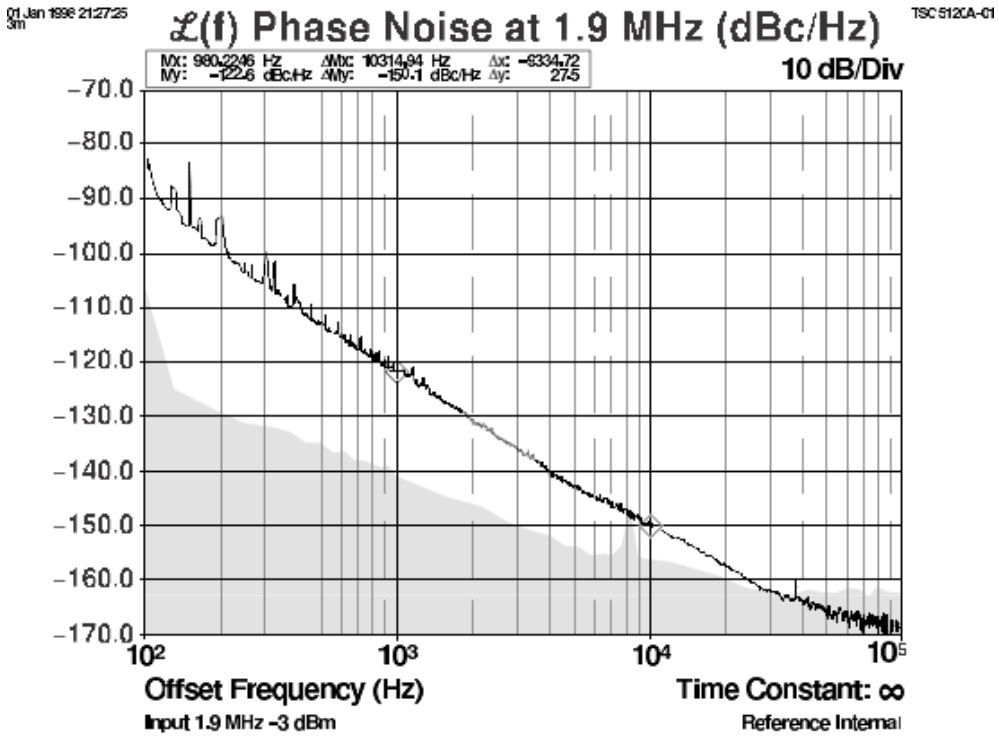

Figure 3.67: Phase Noise Plot of the 3.8 GHz oscillators. The phase noise measured was -150.1 dBc/Hz at 10kHz and -122.6 dBc/Hz at 1kHz offset.

It should be noted that the quoted value is 3dB lower than in the displayed on the plot in **Figure 3.67**. This is because two identical oscillators have been mixed together in order to produce the result and it is therefore necessary to subtract 3dB from the measured value.

Table 3.8: Comparison of the 3.8GHz oscillators theory with that of measurement for a noise figure of 4dB and a flicker noise corner of 20kHz (assumed).

Offset Frequency	Theory	Measured
1 kHz	-128.4 dBc/Hz	-125.6 dBc/Hz
10 kHz	-156.8 dBc/Hz	-153.1 dBc/Hz

The theoretical noise for the two oscillators was calculated to be -156.6 dBc/Hz at 10kHz and -128.4 dBc/Hz at 1kHz respectively as shown in **Table 3.8**. There is a deviation of 3dB in terms of the measured phase noise from that of the theory. If the noise figure of the amplifier was increased by 3dB under saturation, then the theoretical and the measured phase noise would tie in and hence residual noise measurements were performed to measure the noise figure of the amplifier under saturation.

3.9.7 Residual Phase Noise Measurements

Residual phase noise measurements of the active components are measured using the broadband York System which has recently been demonstrated to have a noise floor of -200dBc/Hz at L Band [14]. The block diagram of the residual phase noise measurement set up using the cross correlation technique is shown in **Figure 3.68**. The measurement system consists of two HP 11848A phase noise sets which have the phase detector, LNA and the anti-aliasing filters. These units exhibit a low single channel noise floor of below -180 dBc/Hz at carrier offsets greater than 10kHz [53].

The reference source is provided by a battery powered ultra-low phase noise dielectric resonator oscillator (DRO) developed in the previous prototype at 3.8GHz which had a phase noise of -153 dBc/Hz at 10kHz offset. When compared to a commercial signal generator this DRO has a much lower phase noise and believed to have a much lower AM noise too. A low level of AM noise is important when measuring the residual phase noise of the devices since the saturated double balanced mixers only offer up to 20 to 30 dB of AM noise suppression [53]. If the AM noise is not suppressed, then this can directly add to the residual phase noise and the measurements can be masked. Saturation of the mixers is required in order to make sure that any AM noise present at the input of the mixers can be suppressed. Also, double shielded microwave cables were used in order to reduce any external noise sources.

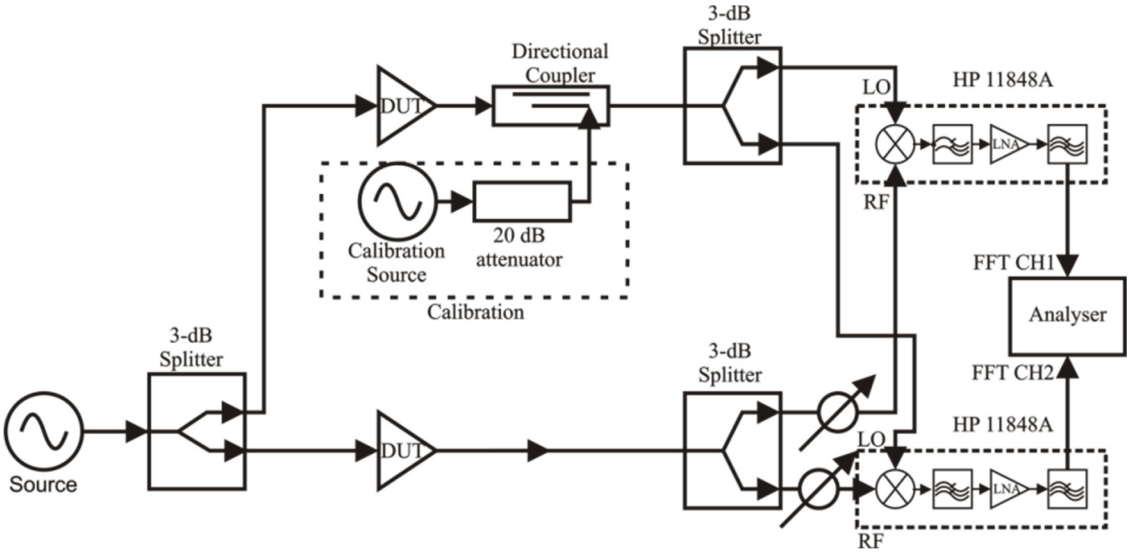

Figure 3.68: Cross Correlation measurement setup using two HP11848A phase noise test sets.

Single side band calibration was performed with the help of a signal which was injected into to measurement setup with the help of a directional coupler as

shown in **Figure 3.68**. An R&S SMB100A signal generator was used as a calibration source. This frequency now modulates the carrier signal present at the LO ports of the phase detector and hence any non-linear effects present in the mixer are taken into consideration. This calibration tone modulates the carrier signal present at the LO ports of both phase detectors and will therefore appear as a single side-band spur at the inputs to the cross spectrum analyser [53]. The primary advantage of calibrating the instrument in this way is that the calibration is performed under the actual measurement conditions with the device in place. It should also be noted that ideally a calibration spur should be injected at every measurement frequency of interest; however, the frequency response of the HP11848A units is sufficiently flat that this is not necessary. However, the downside of this technique is that, a second source and a directional coupler have to be added in the experimental setup.

The theoretical noise floor can be calculated using **Eq. 3.20**

$$\mathcal{L}(f) = -177 - P_{in} + NF \qquad \textbf{Eq. 3.20}$$

Where (NF) is the noise figure of the combined amplifier and attenuator and (P_{in}) is the power available at the input to the attenuator. In order to make sure that the measurement setup does not mask the actual residual noise measurements of the DUT, a phase noise floor of the measurement system was initially performed at same power conditions i.e the inputs power levels at the input of the mixer. The system noise floor was measured to be at -190dBc/Hz at offsets greater than 10kHz and below -180dBc/Hz around 1KHz. The input power to the amplifier was limited as the input power to the mixer of the single channel residual noise measurement system is limited to +10 dBm. Power at the input of the amplifier (P_{in}) was 8 dBm and a 10 dB attenuator was used after the amplifier (to protect the mixers from high power) which increased the noise figure (NF) by 1.2 dB. **Figure 3.69** shows a plot

of the amplifiers residual phase noise and at offsets above 10 kHz the residual phase noise is approximately -180.5 dBc/Hz which is in good agreement with the theoretical value of -180 dBc/Hz calculated using **Eq. 3.20** and the measured phase noise is -168 dBc/Hz at 1 kHz offset and -178 dBc/Hz at 10kHz offset as shown in **Figure 3.69** and the estimated flicker noise corner of 12.7 kHz. The white noise follows exactly the $(1/P_0)$ law up to 8 dBm input power. **Eq. 3.20** is valid when the amplifier is operated in the linear region. However, when the amplifier is operated in a non-linear or a saturation region, then noise figure (NF) may increase [27] [54] and hence the measurement was repeated for the amplifier at its 1dB compression point, it was observed that the noise figure increased from 4dB to 8dB which is likely the consequence of saturation in the intermediate stage of the amplifiers.

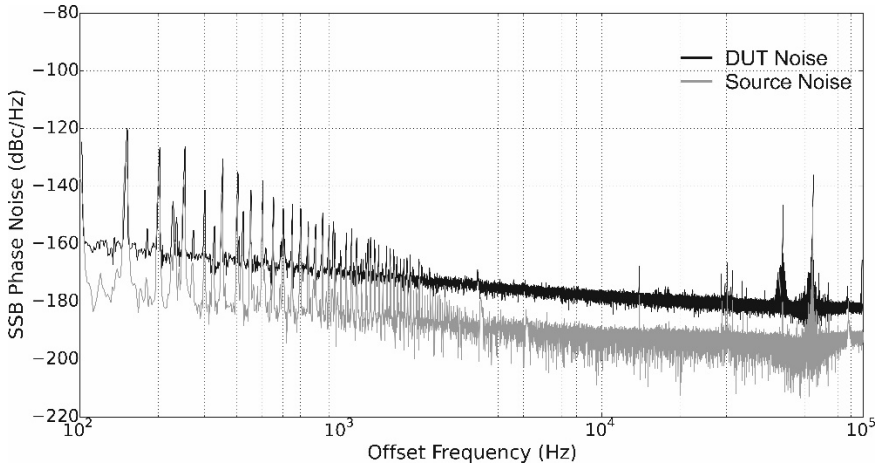

Figure 3.69: Residual phase noise measurements for the 3.8GHz amplifier with P_{in}= 8 dBm and N_A = 5.2 dB.

Hence for a new noise figure of 8dB and with a flicker noise corner of the amplifier estimated to be around 12.7kHz, the theoretical phase noise of the oscillators is -125.5dBc/Hz at 1kHz offset and -153.8dBc/Hz at 10kHz offset. This

shows that the theoretical phase noise using Everard's phase noise equation and the measurements are in very close agreement as shown in **Table 3.9**.

Table 3.9: Comparison of the 3.8GHz oscillators theory with that of measurement for a noise figure of 8dB and a flicker noise corner of 12.7kHz

Offset Frequency	Theory	Measured
1 kHz	-125.5 dBc/Hz	-125.6 dBc/Hz
10 kHz	-153.8 dBc/Hz	-153.1 dBc/Hz

Finally, measurement for the frequency tuning vs Bias voltage was made. This measurement has been performed in order to demonstrate the frequency tuning range which can be obtained using the voltage controlled phase shifter. The voltage controlled phase shifter is then adjusted in 1 volt increments and the frequency of the new peak recorded. A tuning range of 150 kHz with a constant output power can be shown in **Figure 3.70**. A 10-dB attenuator was used at the output of the oscillator to protect the spectrum analyser.

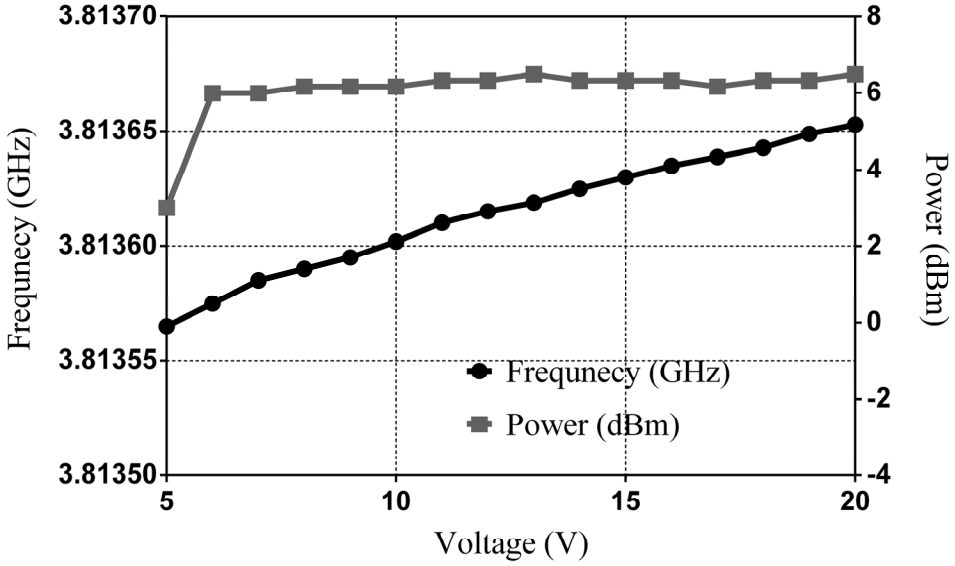

Figure 3.70: Tuning Characteristics of the 3.8GHz Oscillators using the control voltage of the electronic phase shifter.

It can be seen that the tuning response is more linear when compared to that in the previous prototype which was seen in **Figure 3.38**. This is due to the lower impedance which makes it capable of handling higher power levels.

3.10 Conclusions

The first prototype included vibration measurements with a reasonable phase noise measurements developed for Selex-ES. To enhance the phase noise performance, a modular design was later implemented independently enabling all the oscillator elements to be measured and optimised separately. Key additional features are low vibration sensitivity, low weight and low DC power consumption. The phase noise for the 3.8GHz oscillator is -117 dBc/Hz at 1kHz offset and -150 dBc/Hz at 10kHz offset. Two types of vibration sensitivity measurements were performed. One was the spot frequency measurements in the X, Y and Z axes of 0.2g at 100Hz, 500Hz &

1500Hz and second was the random vibration profile which was performed in all three axes at 0.7g rms from 10Hz to 2kHz. The vibration sensitivity (Γ_i) varied from 1.33×10^{-7} to 8.51×10^{-9} per g depending on the axis and the frequency of the vibration.

The second prototype was the improved modular yet compact oscillator was then developed which demonstrated a significantly improved phase noise performance of -125.6 dBc/Hz at 1kHz offset and -153 dBc/Hz at 10kHz offset which is the lowest noise reported in the literature in this frequency band using a dielectric resonator. The theoretical and the measured phase noise of these oscillators are within 0.5dB accuracy. The improved performance is mainly due to increase in the power level of the amplifier and the reduced noise figure. Finally, residual phase noise measurement of the amplifier was made using a broadband cross correlation phase noise measurement system developed at York. The flicker noise corner of the amplifier was estimated to be around 12.7kHz from the residual phase noise measurements.

.

CHAPTER 4

TUNABLE BRAGG RESONATOR

4.1 Introduction

Tunable oscillators are a fundamental element in almost all communication and measurement systems. In these systems high Q tunable resonators are required for low phase noise signal generation. This is because in an oscillator, the phase slope of the resonator (group delay & Q) causes any internal phase fluctuations, within the bandwidth of the resonator, to be transformed into frequency fluctuations and phase noise. Ideally, a tunable filter should have a high tuning range, high unloaded Q in a spurious free window with high power handling capability.

For a planar or a lumped element resonator, the quality factor is limited to a few hundreds and when loaded with a tuning element, the overall quality factor further drops. The maximum unloaded quality factor attainable from a dielectric resonator is defined by the loss tangent (tanδ) of the dielectric material. Modern dielectric resonators (DR) operating in the $TE_{01\delta}$ mode is capable of providing Q-factors of between 10,000 and 30,000 at 10GHz. Hence dielectric resonators are a good choice in oscillators due to a high quality factor. At higher frequencies, the dimensions of the dielectric puck can become small if it is operated in a TE or TM

hybrid mode and alternatively, a whispering gallery mode can be used where the field energy is confined to the outer edge of a ring of dielectric material [6].

When compared to a dielectric resonator, a distributed Bragg resonator can offer a significant increase in the quality factor. This is done by replacing the end walls by alternating layers of air and dielectric material which leads to partial reflection of the incident electromagnetic waves. When several such layers are combined more energy is reflected back into the central air section if kept away from the lossy end metal walls. The reflector section lengths in a Bragg resonator are typically one quarter of the guide wavelength ($\lambda g/4$) in thickness in order to maximize their reflectivity [55].

There are a number of authors who have demonstrated high Q fixed frequency Bragg resonators. The most common dielectric materials are Sapphire, Alumina, Quartz and Yttrium Iron Garnet (YIG). Maggiore et.al demonstrated a quality factor of 531,000 at 18.99GHz using a layered Sapphire resonator [56]. Flory and Taber measured a quality factor of 650,000 using Sapphire resonators at 9GHz [55] while Flory and Ko demonstrated a Q of 450,000 at 13.2GHz using a similar structure [57]. Krupka et.al used single crystal quartz as a dielectric material to build Bragg resonators at 39GHz which had a Q of 560,000 [58]. Spherical Bragg resonators were demonstrated Krupka et.al which were constructed from single crystal YAG and quartz. The resonator produced a Q-factor of 104,000 at 26.26 GHz while the YAG resonator produced a Q of 64,000 at 27.63 GHz [59]. Breeze, Krupka and Alford demonstrate that by utilising an aperiodic arrangement of dielectric plates that the energy losses within a Bragg resonator can be redistributed away from the lossy dielectric materials and into the lower air regions [60]. Simulations also suggest that a spherical Bragg resonator can be designed with a quality factor in excess 10^7 at

10GHz. An aperiodic sapphire resonator consisting of concentric dielectric rings separated by dielectric plates was demonstrated. The resonator had a Q factor of 600,000 at 30 GHz [61]. More recently, Bale and Everard demonstrated a fixed frequency aperiodic cylindrical Bragg resonator using alumina plates with an unloaded Q of 200,000 at 10GHz [15].

Several technologies are presented in the literature to realize the tuning elements in order to tune the centre frequency. Ferroelectric materials [62], Yttrium Iron Garnet (YIG) [63], piezoelectric, micro electromechanical systems (MEMS) [64] are the most common used tuning elements. However, in most of these systems the tuning range and the unloaded Q are very limited. All of these tuning elements degrade the quality factor as the tuning range is increased. Mechanical tuning of a dielectric resonator can be achieved by perturbing the magnetic field distribution around the resonator by moving a metallic or a dielectric object close to the dielectric puck. Initially, Wakino reported a mechanically tuned dielectric resonator in 1987 which use a piezoelectric actuator on the top of the dielectric resonator to tune the centre frequency. The actuator was controlled with a use of a DC voltage where a tuning range of up to 8% can be achieved using this technique [65] [66]. Dielectric resonator can also be tuned with the use of another dielectric material or a resonator with the same dielectric constant to perturb the field inside the original dielectric resonator [67] [68]. Dielectric resonator using MEMS based tuning element where MEMS actuators controlling the tuning disk are used (instead of the tuning screws) has been reported. At 4GHz a tuning range of 1.5% was demonstrated with an unloaded Q of 3730 [69]. Magnetically tuned dielectric resonators are the other form of tunable resonators where a low loss ferrite material is used to change the resonant frequency [70] [71]. The highest Q obtained using this technique was 4000 with a

tuning range of 1.3% at 2.3GHz. Tunable dielectric resonators using varactors were reported in [70] [72] [73] where the resonator consists of 2 varactors. The change in the resonant frequency was obtained by changing the boundary conditions on the metal ring which is located close to the resonator on the substrate. A maximum unloaded Q of 8000 was reported at 3.5GHz with a tuning range of 1.6%. YIG is a ferrite material which resonates when placed in a magnetic field and the frequency of response is directly proportional to the magnetic field. They are capable of having unloaded Q's of up to 10,000 at 10GHz [74] with low insertion loss and broad tuning ranges making them the best choices for tunable filters in communication systems [75]. **Table 4.1** shows the comparison of tuning range and unloaded Q dielectric resonators with different tuning elements.

Table 4.1: Comparison of tuning range and the quality factor of various tunable resonators present in the literarture.

	Type of the Resonator (Tuning Element)	Frequency (GHz)	Tuning Range	Maximum Unloaded Q
[65]	Dielectric (Dielectric Plugs)	1.965	10%	16,000
[76]	Dielectric (MEMS)	2	0.25%	12,000
[77]	Two pole dielectric filter (MEMS)	4	1.5%	3,730
[71]	Dielectric (Ferrite)	2.2	1.3%	4,000
[72]	Dielectric (Varactor)	3.5	1.6%	8,000
This work	**Dielectric (Mechanical)**	**10**	**1%**	**81,650**

In the work presented here, a tunable distributed aperiodic Bragg resonator is built which demonstrates a tuning range of 1% (100MHz) at 10GHz with a maximum unloaded Q of 81,650. In the following sections of the chapter the modelling of the resonator using an ABCD matrix along with the design and construction of the cavity with the tunable centre section has been described.

4.2 Resonator Modelling and Simulations

The performance of the Bragg resonator can be modelled by using ABCD parameters to describe the resonator as a cascaded set of waveguides as shown in **Figure 4.1** while the cross section of the aperiodic Bragg resonator is shown in **Figure 4.2** [15].

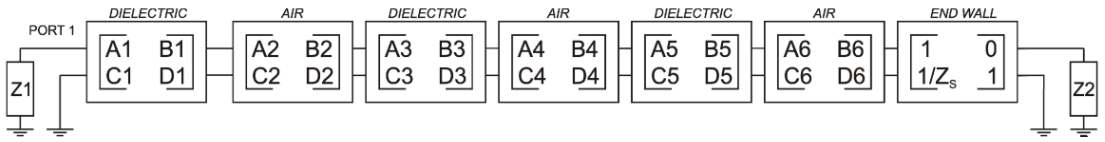

Figure 4.1: Model of the Bragg resonator using ABCD matrices for one half of the resonator [15].

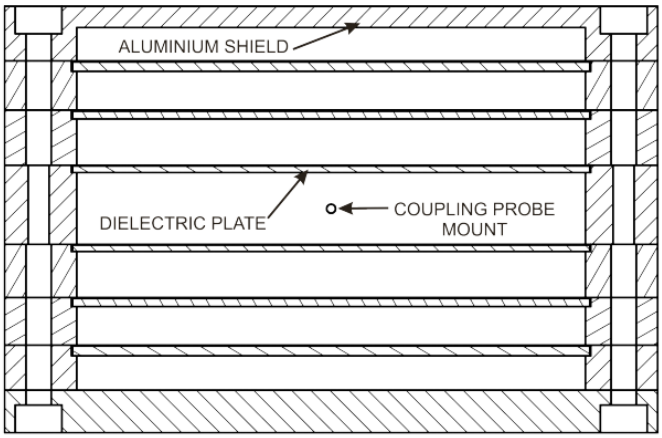

Figure 4.2: A cross section view of the six plate aperiodic Bragg resonator [15].

The advantage of using ABCD matrices is that the response of cascaded sections is just the product of the matrices. This is achieved through the definition

of the directions of the input and output currents. The resonator model must now contain ABCD matrices for the air sections, dielectric sections and for the end wall to form the Bragg Resonator as seen in **Figure 4.3**.

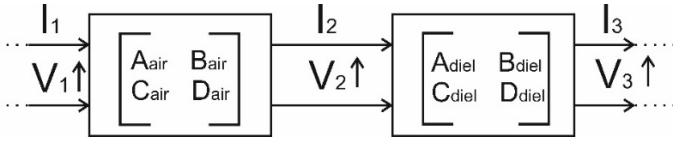

Figure 4.3: Cascaded connection of the 2 port using ABCD matrices.

The resulting matrix equation for a cascaded connection of an air and dielectric section is given by:

$$\begin{bmatrix} V_1 \\ I_1 \end{bmatrix} = \begin{bmatrix} A_{air} & B_{air} \\ C_{air} & D_{air} \end{bmatrix} \begin{bmatrix} A_{diel} & B_{diel} \\ C_{diel} & D_{diel} \end{bmatrix} \begin{bmatrix} V_3 \\ I_3 \end{bmatrix} \qquad \textbf{Eq. 4.1}$$

The ABCD matrix for a lossy transmission line of length l meters with complex propagation constant γ and characteristic impedance Z_o is shown in **Eq. 4.2**.

$$\begin{bmatrix} V_1 \\ I_1 \end{bmatrix} = \begin{bmatrix} Cosh(\gamma l) & Z_o Sinh(\gamma l) \\ \frac{1}{Z_o} Sinh(\gamma l) & Cosh(\gamma l) \end{bmatrix} \begin{bmatrix} V_2 \\ I_2 \end{bmatrix} \qquad \textbf{Eq. 4.2}$$

The complex propagation constant, γ, is defined as:

$$\gamma = \alpha + j\beta \qquad \textbf{Eq. 4.3}$$

Where α is the attenuation co-efficient (Npm^{-1}) and β is the phase constant ($rad\ m^{-1}$). The phase constant for the air and the dielectric sections can be found by using:

$$\beta = \sqrt{\omega^2 \mu\varepsilon - \left(\frac{\chi'_{mn}}{a}\right)^2} \qquad \textbf{Eq. 4.4}$$

where ε is the permittivity of the material filling the guide and ω is the angular frequency and a is the cavity radius. χ'_{mn} represents the n^{th} zero of the derivative of

the Bessel function of the first kind of order m. In the case of the TE_{01} mode the value of χ'_{mn}= 3.8318. The attenuation coefficients for the air and the dielectric sections of the Bragg resonator are now discussed.

4.2.1 Air Section

The loss in the air sections is due to the conductive side wall losses. This can be modelled as shown in **Eq. 4.5**. This equation represents the attenuation coefficient, in units of Npm^{-1}, for a transverse electric (TE) mode with circumferential mode number m and radial mode number n in a cylindrical waveguide of radius 'a' operating at frequency, f_c:

$$\alpha_{air} = \frac{R_s}{a\,\eta\sqrt{1-\left(\frac{f_c}{f}\right)^2}}\left[\left(\frac{f_c}{f}\right)^2 + \frac{m^2}{(\chi'_{mn})^2 - m^2}\right] \qquad \textbf{Eq. 4.5}$$

Where η, is the wave impedance for a plane wave inside an unbounded infinite medium, R_s is the surface loss resistance of the walls and f_c is the lower cut off frequency of the guide and η is the wave impedance inside an unbounded infinite medium with permittivity $\mathcal{E}$ and permeability μ is given by **Eq. 4.6**.

$$\eta = \sqrt{\frac{\mu}{\mathcal{E}}} \qquad \textbf{Eq. 4.6}$$

The Rs is the surface loss impedance is given by **Eq. 4.7** which is related to the wall conductivity (σ) while the lower cut off frequency (f_c) is given by **Eq. 4.8** [38].

$$R_s = \sqrt{\frac{\omega\mu}{2\sigma}} \qquad \textbf{Eq. 4.7}$$

$$f_c = \frac{\chi'_{mn}}{2\pi a\sqrt{\varepsilon\mu}} \qquad \textbf{Eq. 4.8}$$

4.2.2 Dielectric Section

The total loss in the dielectric sections, α_{total}, can be considered as the sum of the sidewall conducting loss, α_a and the dielectric losses, α_d

$$\alpha_{total} = \alpha_a + \alpha_d \cong \alpha_d \qquad \textbf{Eq. 4.9}$$

The conductive side wall losses can be calculated using **Eq. 4.5** but the loss in the dielectric must be treated differently. The attenuation due to the lossy dielectric α_d can be calculated from the complex propagation constant as shown in [4]. If the loss is small, then the phase constant in the dielectric section can be assumed to be constant. The attenuation due to dielectric loss is given by equation **Eq. 4.10** and the units are in Npm^{-1}.

$$\alpha_d = \frac{\omega^2 \mu \varepsilon tan\delta}{2\sqrt{\omega^2 \mu \varepsilon - \left(\frac{\chi_{mn}}{a}\right)^2}} \qquad \textbf{Eq. 4.10}$$

4.2.3 End Wall

The loss in the metal end walls of the cavity can be approximated by considering the complex propagation constant,γ, and intrinsic wave impedance, η, for a plane wave in a good conductor. The complex propagation constant inside a good conductor is given by **Eq. 4.11**.

$$\gamma = (1+j)\sqrt{\frac{\omega\mu\sigma}{2}} \qquad \textbf{Eq. 4.11}$$

The wave impedance inside a lossy medium is given by **Eq. 4.12**:

$$\eta = \frac{j\omega\mu}{\gamma} \qquad \textbf{Eq. 4.12}$$

The ABCD parameters for the end wall section can be written as **Eq. 4.13**

$$\begin{bmatrix} V_1 \\ I_1 \end{bmatrix} = \begin{bmatrix} 1 & 0 \\ 1/Z_s & 1 \end{bmatrix} \begin{bmatrix} V_2 \\ I_2 \end{bmatrix} \qquad \textbf{Eq. 4.13}$$

Where:

$$Z_S = (1 + j)\sqrt{\frac{\omega\mu}{2\sigma}} \qquad \textbf{Eq. 4.14}$$

Where σ is the electrical conductivity of cavity shield. The loss tangent (tan δ) of the dielectric material determines the maximum unloaded quality factor. The attenuation in the air and the dielectric sections along with the wall losses degrade the unloaded quality factor. Hence, to maximize the quality factor of the resonator, it is critical that wall and dielectric losses are minimized. The side wall loss can be reduced by using a high conductivity metal such as copper, silver or silver plated Aluminium. Therefore γ_{air} and $\gamma_{dielectric}$ [38] [78] have to be calculated in order to model the individual ABCD matrices of the air and the dielectric sections. **Table 4.2** summarises the various constants used in the ABCD model.

Table 4.2: Bragg resonator simulation parameters.

PARAMETER	SYMBOL	VALUE
Cavity radius	a	60 mm
Dielectric permittivity	ε_r	9.75
Dielectric loss tangent	$tan\delta$	2×10^{-5}
Wall conductivity (using silver)	σ	$6.173 \times 10^{7}\ Sm^{-1}$
Air-Phase constant	β_a	$199.68\ radm^{-1}$
Dielectric –Attenuation coefficient	α_d	$6.61 \times 10^{-3}\ Npm^{-1}$
Dielectric - Phase constant	β_d	$651.18\ radm^{-1}$

The parameters shown in **Table 4.2** were used in the ABCD model and an S-parameter simulation was performed for a periodic Bragg resonator. In a periodic Bragg resonator each of the dielectric plates and air sections are one quarter of the guide wavelength ($\lambda_g/4$) in thickness in order to maximize their reflectivity [55].

Once the dimensions of the air sections and the dielectric sections for a periodic Bragg resonator were obtained, the model was then split in two. The reflector section lengths were then optimised until the magnitude of the input reflection coefficient at port one (S_{11}) reached a maximum using the ABCD solver and a genetic algorithm. The phase response of the reflection was taken into account by adjusting the length of the centre section. This then produced an aperiodic Bragg resonator. The lengths are now dependent on the losses and dispersion in each section as well as the frequency of operation. The dimensions of the individual sections are given in **Table 4.3** where LD's are the lengths of the dielectric sections, LA's are the lengths of the air section and the LCental is the length of the central air section.

Table 4.3: Dielectric and air section reflector thicknesses for an optimised 6 plate Bragg resonator [15].

Section Identifier	Material	Length (mm)
LD1	Dielectric	1.512
LA2	Air	11.023
LD3	Dielectric	1.887
LA4	Air	9.300
LD5	Dielectric	2.253
LA6	Air	8.060
LCentral	Air	17.033

As stated earlier, tuning can be achieved by changing the length of the centre section, this is because the Bragg mirrors offer low loss high reflectivity over a broad frequency range, exceeding 10% of the centre frequency. This is illustrated by tuning the length of the centre section by $\pm$15%. Further, this model only considers the

wanted TE_{011} mode. The nominal length of the centre section (17.033mm) was tuned by $\pm$4 mm in 1 mm increments and the ABCD model was used to simulate the new unloaded Q and centre frequency for the TE_{011} mode. The plot of change in frequency and Unloaded Q vs change in length is shown in **Figure 4.4**.

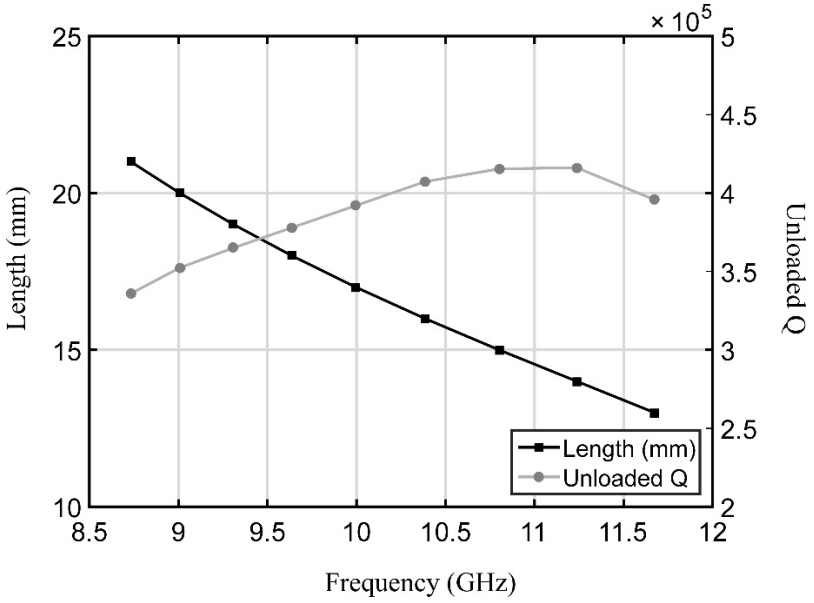

Figure 4.4: Simulation of the quality factor and resonant frequency as a function of the central section length for the TE_{011} mode.

4.3 Design and Construction

In the previous work at York, the tunable section was built with the use of concentric cylinders. However, when the resonator was assembled and tested, the required mode wasn't observed. This was believed due to the energy leakage from the cylinders [35]. The resonator developed in [15] was modified to incorporate a new tunable centre section which incorporated copper bellows. The following steps were used to construct the tunable centre section:

Step 1: The bellows were made up of two large copper rings and were etched with solder release groves (mask of the copper rings shown in appendix A.4) in order to control the position of the solder as shown in **Figure 4.5**. This controls the exact position of the solder within the bellows and also prevents it from flowing into the cavity which may degrade the Q. These rings also have a number of tabs around the outer edges which are folded shut to ensure the bellows remain soldered during the later processing stages. The copper rings were soldered with each other to form a bellow using unleaded solder.

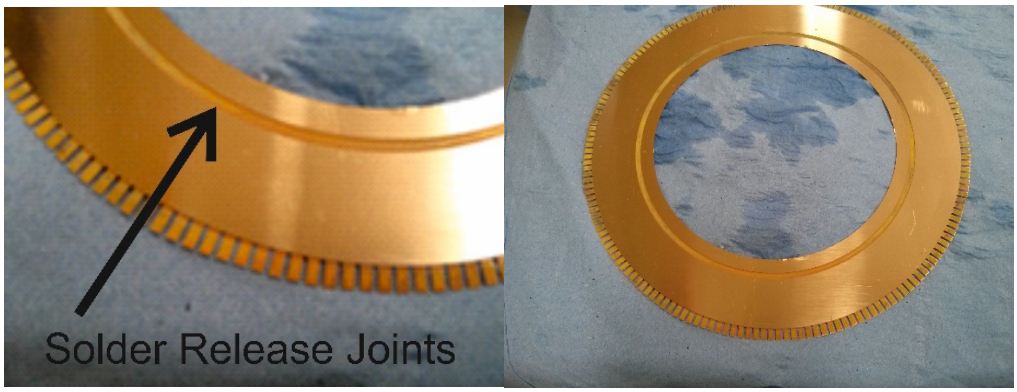

Figure 4.5: Copper sheets with etched solder release grooves in order to control the position of the solder.

Step 2: Once the bellows were constructed, one set of bellows were soldered to the middle section on a hot plate using unleaded solder.

Step 3: Finally, the second set of bellows were soldered on to the middle section but during this process, the bellows which were soldered in the previous step re-liquefied and disintegrated. Since the construction of the centre section was a complex technique which involved soldering of multiple plates together, it was believed that a number of different soldering operations have to be performed using two different

temperature solders. This would prevent the solder from reflowing when a new joint was produced.

Hence, experiments were conducted using different leaded and un-leaded solder which are at different temperatures. The left hand side is the leaded and the right hand side is the un-leaded solder paste at 50°C, 150°C and 200°C as shown in **Figure 4.6**. At 150°C, the leaded solder liquefies while the un-leaded solder only starts to liquefy at 200°C. Hence, the unleaded solder was used for the copper bellows (200°C) for step 2 and at the final stage of the construction the leaded solder (150°C) was used which was in step 3.

Figure 4.6: Leaded and un-leaded solders at 50°C, 150°C and 200°C.

To obtain the correct ratio of loaded to unloaded Q (Q_L/Q_0) and insertion loss for low noise oscillators [11] , the probes need to be placed in the middle of the centre section close to the cavity wall. The tunable centre section is shown in **Figure 4.7**. Micrometres were used to tune the length of the central section.

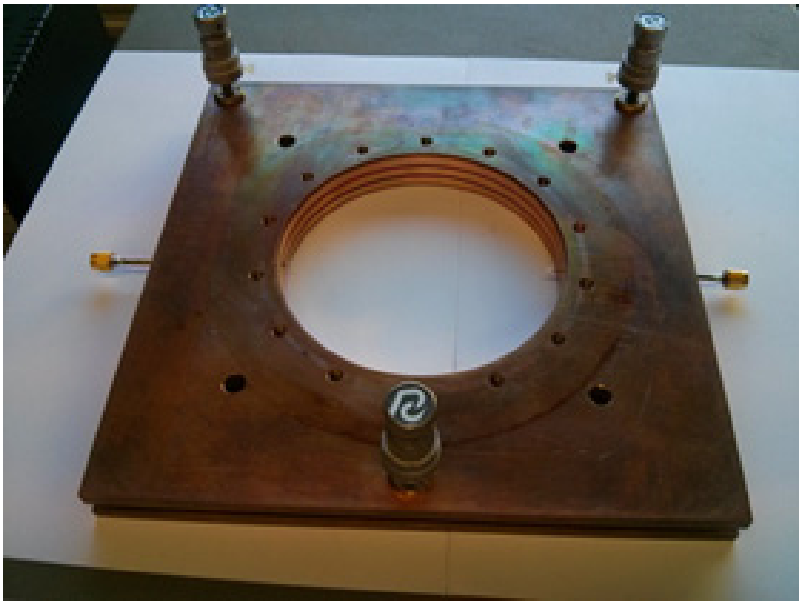

Figure 4.7: Centre section with the micrometers and the loop probes to couple energy into the cavity.

The cross section of the tunable Bragg resonator prototype (not to scale) is shown in **Figure 4.8**. The central tunable section now comprises an upper section, bottom section and a solid middle section for the probe placement with two bellows either side of the centre section. The air waveguide dimensions of the centre sections were optimised to incorporate the thickness of the copper sheets which form the tuning bellows.

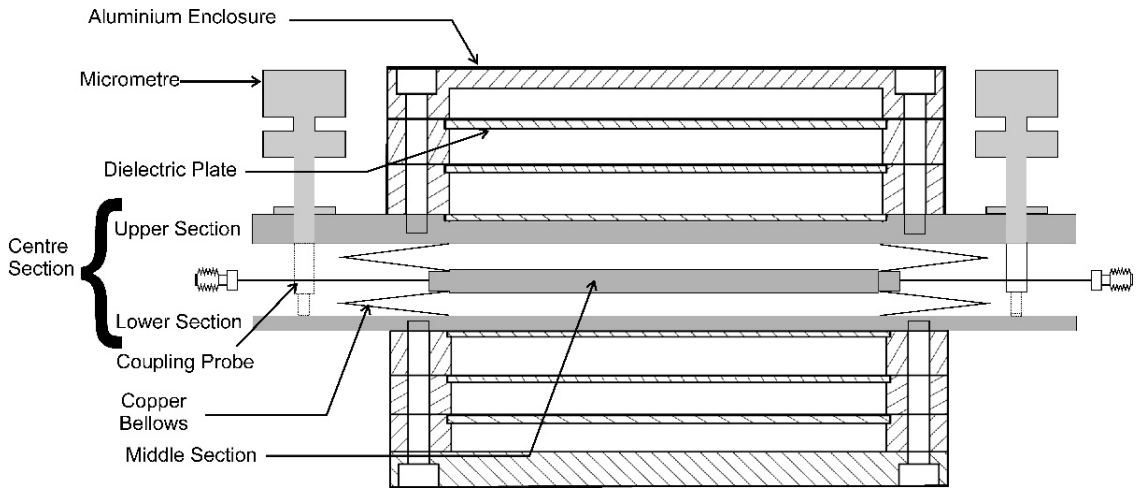

Figure 4.8: Cross section view of a 6 plate Tunable Aperiodic Bragg Resonator.

Tunable Bragg resonator which utilises an aperiodic arrangement of non ($\lambda_g/4$) low loss alumina plates mounted in a cylindrical waveguide is shown in **Figure 4.9** along with the micrometers which are used for tuning.

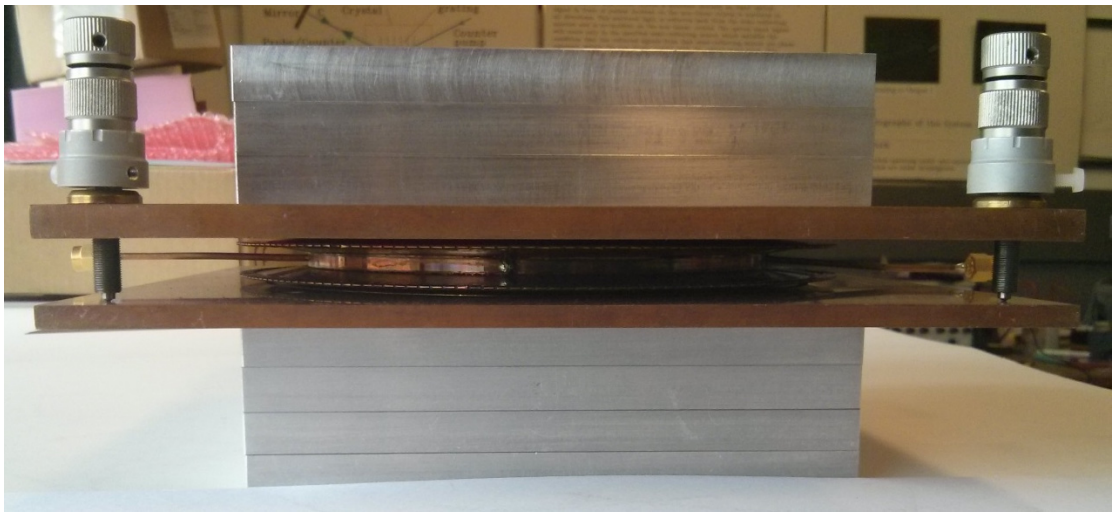

Figure 4.9: Tunable Bragg resonator showing the micrometres and upper and lower reflector sections.

4.4 Initial Results

Measurements of the tuning range were achieved by initially setting the micrometres to a maximum position so that the spacing between the upper section and the lower section was maximised. Micrometers were then used to tune the frequency of the cavity over 500 MHz (5% tuning range with degradation of unloaded Q) and the insertion loss and the loaded Q were measured on a network analyser. The change in the frequency was also noted and the highest unloaded Q obtained was 64,000. It was observed that the required TE_{011} mode passes through several low Q modes degrading the unloaded Q as shown in **Figure 4.10** where the insertion loss increases.

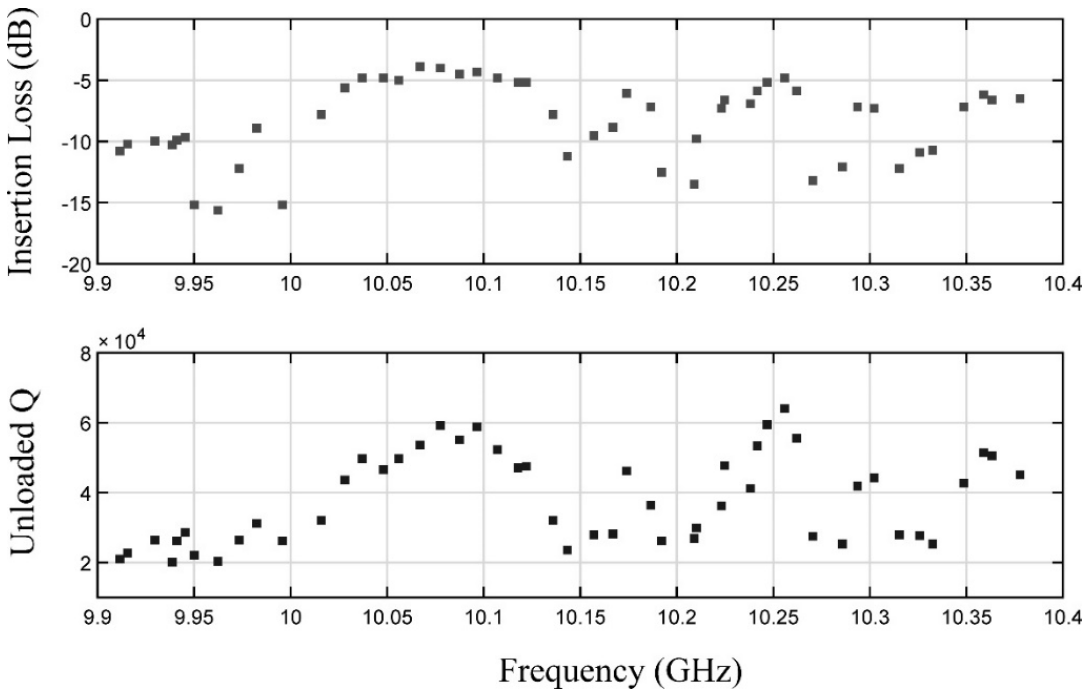

Figure 4.10: Plot of measured insertion loss and unloaded Q Vs Frequency with 500MHz span.

It was observed that for a span of 100MHz which is from 10.02GHz to 10.12GHz, the insertion loss of the wanted mode was almost the same without any degradation. The network analyser was re-calibrated at each centre frequency from 10.02GHz to 10.12GHz (1% tuning range) and insertion loss and the laoded Q were noted for a suprious free region with no unwanted modes. The insertion loss, S_{21}, varies from -5.6dB to -4dB while the loaded Q varied from 20,000 to 23,000. The unlaoded Q can be found by using **Eq. 4.15**.

$$Q_0 = \left(\frac{Q_L}{1 - |S_{21}|}\right) \qquad \textbf{Eq. 4.15}$$

Unloaded Q varies from 40,000 to 60,000 over the tuning range of (1%) 100MHz. The plot of insertion loss and unloaded Q Vs Frequency with a narrow 100MHz span is shown in **Figure 4.11**.

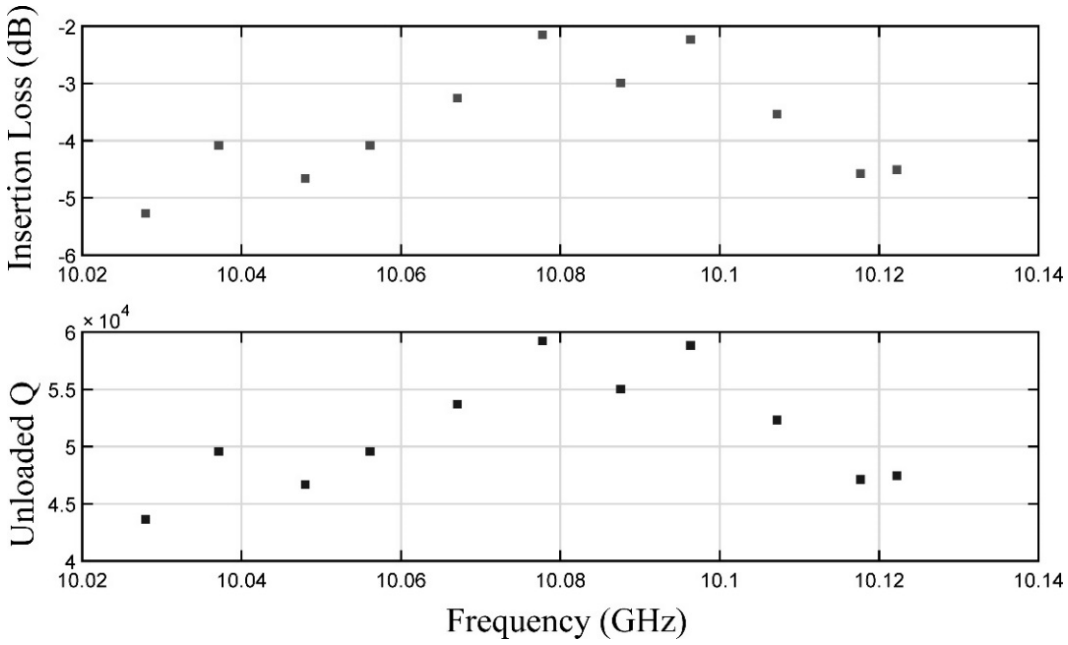

Figure 4.11: Plot of insertion loss (S_{21}) and unloaded Q Vs Frequency with a narrow 100MHz span with no unwanted modes.

4.5 New Prototype

The centre section was disassembled to construct a new section; it was observed that some of solder reflowed back into the centre of the cavity which is a high field region. It was also observed that the screws which were used to hold the top and the bottom sections of the resonator had penetrated into the copper bellows which could lead to energy leakage from these holes. All these factors affected the unloaded Q and hence a new middle section was constructed using the same upper and the lower sections from the previous prototype. The middle section was improved in order to incorporate a solder release ring which was similar to the ones included in the copper rings to control the position of the solder as shown in **Figure 4.12**. This stops the solder from entering the centre section of the resonator when put on a hot plate during the soldering procedure. A new middle section was constructed from copper plate for the same purpose which included the solder release rings. The entire central section was once again assembled using the same technique mentioned in the previous sections using different temperature solders for step 2 and step 3.

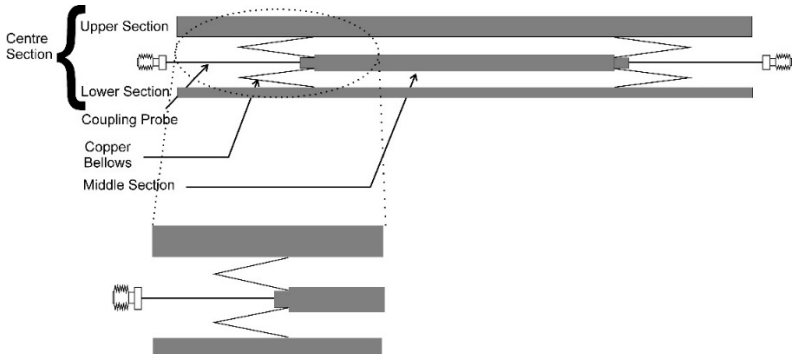

Figure 4.12: Modified middle section with solder release rings to control the position of the solder.

4.5.1 Measurement Results

Measurements of the tuning range were achieved by initially setting the micrometres to a maximum position so that the spacing between the upper section and the lower section was maximised which was similar to the previous prototype. The micrometres were then adjusted so that required TE_{011} mode was observed. The forward transmission coefficient scattering parameter (S_{21}) was measured on a network analyser for a frequency span of 1GHz as shown in **Figure 4.13**.

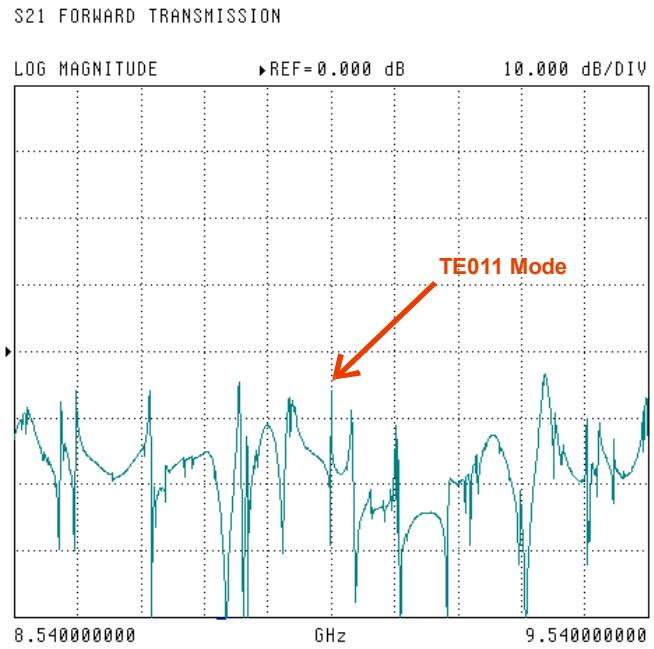

Figure 4.13: A plot of the forward transmission coefficient *(S_{21})* for the 6 plate aperiodic tunable Bragg resonator for a frequency span of 1GHz.

The wanted resonance can be clearly seen at the centre of **Figure 4.13**. at 9.04GHz. Several spurious modes which are close to the required mode are also clearly visible. The reduced centre frequency from 10.06 GHz to 9.02GHz in the second prototype can be explained due to the fact that a new middle section was

built and might have some uncertainties during the manufacturing process. Simulations suggest that length must have changed by 1.5-2mm in order to have the centre frequency at 9.0GHz. The total change in length might be due to this along with the thickness of the solder paste. Once the required mode was located, the micrometres were then slowly adjusted in order to tune the resonant frequency. A combined plot showing the tuning range of this mode is shown in **Figure 4.14**. Each trace shows a plot of S_{21} over a span of 100 MHz and the traces are cascaded left to right with increasing frequency. A spurious free tuning region of 1% i.e 100 MHz from 8.97 GHz to 9.07 GHz is observed. It should be noted that once the TE_{011} mode moves away from this spurious free tuning range, the required mode passes through several low Q modes degrading the unloaded quality factor. The length of the centre section determines the centre frequency. The reduction in the centre frequency when compared to the previous prototype could be explained due to the fact that a new middle section was constructed. A mm of change in the centre section would move the frequency by almost 450MHz as seen in **Figure 4.4**.

Figure 4.15 shows plots, with a 100 MHz span, of the TE_{011} resonance at the start (blue trace), middle (red trace) and end (black trace) of the tuning range. At the start of the tuning range (8.97GHz) the closest spurious mode is 20MHz lower in frequency than the wanted mode and as we tune the centre section, we move away from this spurious mode (blue trace). At the centre of the tuning range (red trace) which is 9.02GHz, the spurious modes are $\pm$41MHz above and below the centre frequency and at the end of the tuning range at 9.07GHz the closest spurious mode is 17 MHz higher in frequency (black trace).

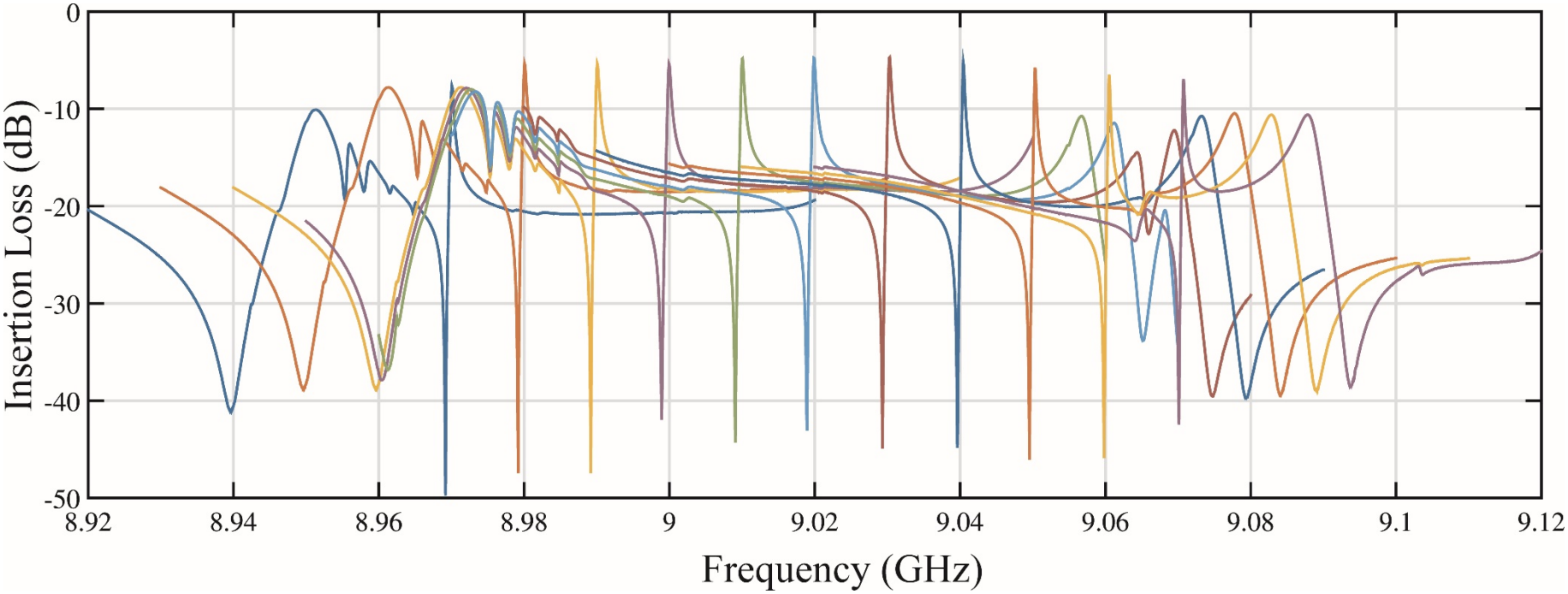

Figure 4.14: A plot of insertion loss vs Frequency over the tuning range. Each trace shows a plot of S_{21} over a span of 100MHz.

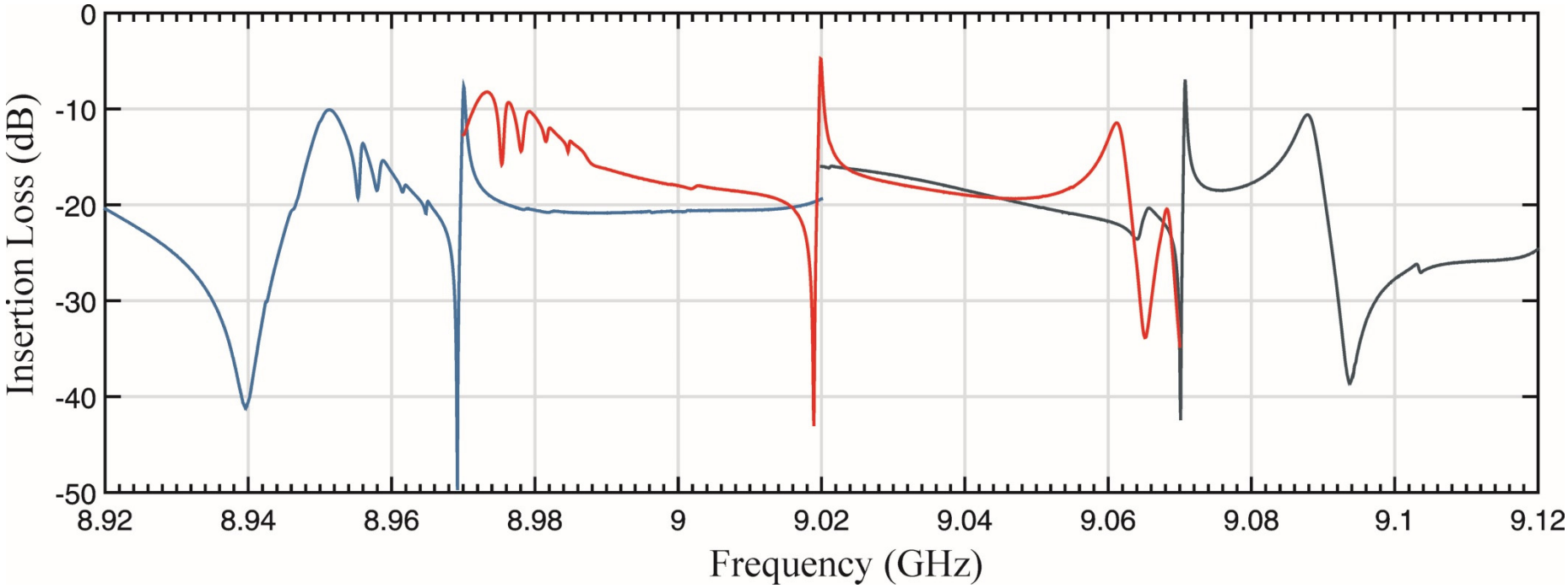

Figure 4.15: A plot of insertion loss vs frequency at the start, centre and end of the tuning range. The location of the closest spurious modes is visible.

The span was then reduced to 2MHz to get an accurate measurement of the insertion loss (S_{21}) and the loaded Q (Q_L) for the individual frequencies. The unloaded Q (Q_0) was calculated using **Eq. 4.15**. The results are shown in **Figure 4.16** where it can be seen that the maximum and minimum unloaded quality factors are 81,650 and 61,020 respectively over the spurious free tuning range i.e from 8.97GHz to 9.07GHz, a tuning range of 1%. The insertion loss (S_{21}) varies between -3.6 dB and -6.4 dB over this range.

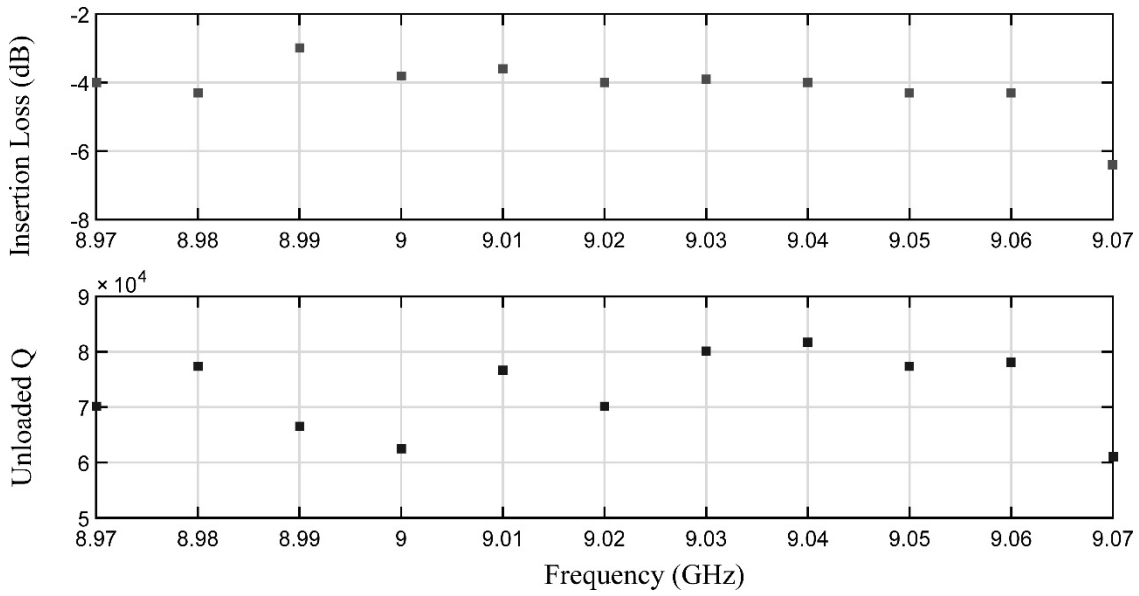

Figure 4.16: A Plot of the insertion loss (S_{21}) and unloaded quality factor (Q_0) for the tunable Bragg resonator. The cavity was tuned over a 100 MHz span.

A plot of insertion loss vs frequency with a narrow span of 2MHz with the 3dB points for the highest unloaded Q of 81,650 is shown in **Figure 4.17**. The insertion loss (S_{21}) was measured to be -4.307 dB and the unloaded Q was 81,650 using **Eq. 4.15**.

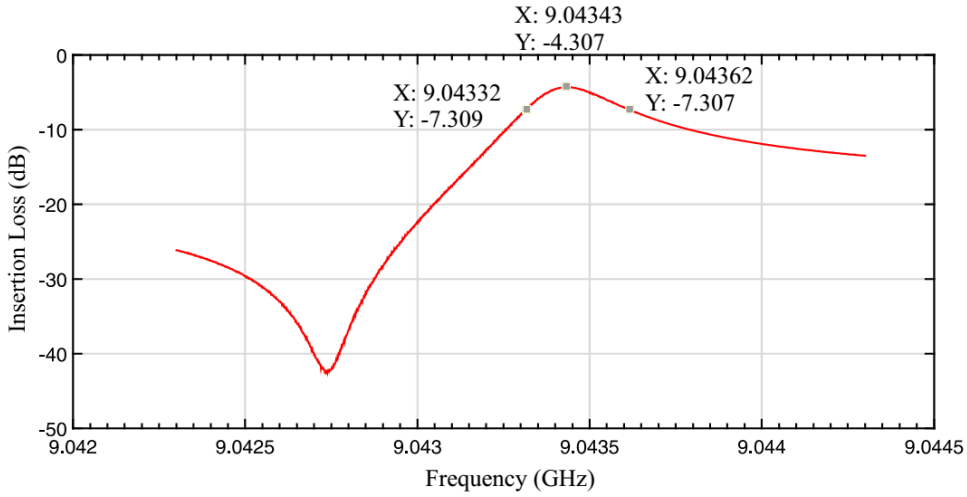

Figure 4.17: A plot of insertion loss and unloaded Q vs Frequency with a 2 MHz span for an unloaded Q of 81,650

The unloaded Q is lower than the numerical simulation results. This may be due to conductor losses in and around the bellows including losses in the solder as well as leakage and mode conversion due to the discontinuities in the structure. The loss tangent of the Alumina plates may have been larger than the manufacturer's specification resulting in increased dielectric losses. It is interesting to know that if the loss tangent is doubled, the unloaded Q halves.

4.6 Conclusions

In this chapter, the design and construction of a tunable Bragg resonator has been described. The best performance achieved was a spurious free tuning range of 1% at 9GHz with a maximum unloaded Q of 81,650. This is believed to be the best available high Q tunable resonator available at 10GHz present in the literature. The insertion loss varies from -3dB to -6.4dB while the unloaded Q varies from 61,020 to

81,650 over the tuning range. At the start of the tuning range (8.97GHz) the closest spurious mode is 20MHz lower in frequency than the wanted mode and as we tune the centre section, the resonant mode moves away from this spurious mode. At the centre of the tuning range which is 9.02GHz, the spurious modes are $\pm$ 41MHz above and below the centre frequency and at the end of the tuning range at 9.07 GHz the closest spurious mode is 17MHz higher in frequency.

CHAPTER 5

10GHz BRAGG RESONATOR OSCILLATOR

5.1 Introduction

The design, construction and measurement of an ultra-low phase noise 10GHz oscillator using an aperiodic Bragg resonator is presented in this chapter. Oscillators utilising dielectric resonators (DR) are mainly used at microwave frequencies since they offer Qs greater than 10000 at 10GHz. The other advantage of using a DR is that they have better power handling capability compared to crystal resonators. The exceptionally low loss-tangent of sapphire (Al_2O_3) allows very high-Q resonators at both cryogenic and room temperatures. The Q factor of almost 200,000 at 300K and can exceed 6 x 10^9 at 2K and 5 x 10^7 at 77K at 10GHz [79]. However oscillators utilising these resonators often use very sophisticated flicker noise reduction techniques [80]. A Bragg resonator built using low loss materials can offer a significant increase in quality factor when compared to the traditional dielectric resonator at room temperature. Qs up to 650,000 can be obtained using Sapphire resonators consisting of interpenetrating concentric rings and plates at 9.0GHz [55]. More recently, Bale and Everard demonstrated a fixed frequency aperiodic cylindrical Bragg resonator using alumina plates with an unloaded Q of 200,000 at 10GHz [15].

A number of oscillators have been built using dielectric and sapphire resonators at room temperatures but the best room temperature oscillators at 10GHz currently available use sapphire whispering-gallery mode resonators. Sallin et al. demonstrated a dielectric resonator oscillator (DRO) at 10GHz with an unloaded Q of 17,400 which had a phase noise of -135 dBc/Hz at 10kHz offset using a SiGe as an active device [34]. Gupta et al. demonstrated a phase noise of -145 dBc/Hz at 1kHz using an air filled cavity operating in higher TE_{023} modes. To achieve this phase noise performance, interferometric signal processing was used to suppress the carrier [81]. Furthermore, M.Tobar et al. demonstrated a low noise sapphire based oscillator at 9GHz with a high Q sapphire loaded cavity at room temperatures that initially resulted in a phase noise of -125 dBc/Hz at 1kHz offset [82]. Later they went on to demonstrate a phase noise of -150 dBc/Hz at 1kHz offset with the help of a phase noise reduction technique where the resonator is used as band pass filter as well in the oscillator as well as in a frequency discriminator [83]. Flory and Ko then used a sapphire distributed Bragg resonator at room temperature with an unloaded Q of 700,000 to demonstrate a phase noise of around -152 dBc/Hz at 10kHz offset using an HBT TC200 as an active device [57]. Recently, a phase noise of -148 dBc/Hz at 10kHz offset was demonstrated by Boudotet et.all by using a high Q whispering gallery mode sapphire resonator with an unloaded Q of $8x10^4$ at 9.5GHz [84]. Commercially available oscillators from PSI using a sapphire loaded cavity oscillator at 10.24GHz demonstrated a phase noise of -170 dBc/Hz at 10kHz offset [6]. The lowest available phase noise was reported by Ivanov et al. They demonstrated a phase noise of -160dBc/Hz at 1kHz using a high Q sapphire dielectric resonator [85]. Also, in cryogenic oscillators, the best phase noise of -162dBc/Hz at 1kHz offset with

a Q of 60 million was obtained at 80K using a liquid nitrogen sapphire loaded cavity operating at a whispering gallery mode [86].

In this work a 10GHz oscillator utilising an aperiodic Bragg resonator with an unloaded Q of 200,000 which achieves a phase noise of -123.6 dBc/Hz at 1kHz and -152.5 dBc/Hz at 10kHz offset is presented. The oscillator was built using the feedback topology as shown in **Figure 5.1**.

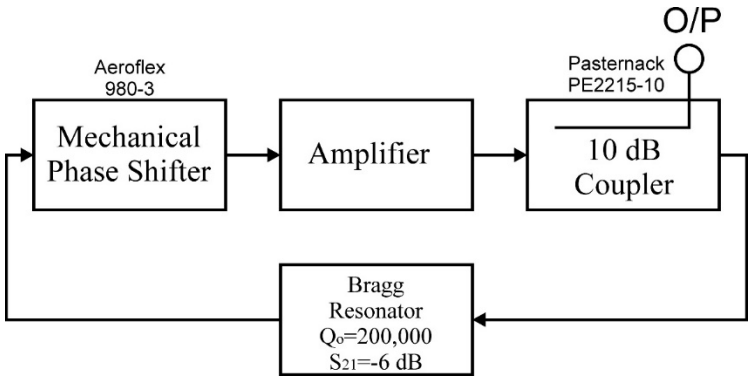

Figure 5.1: Block Diagram of the 10GHz Band Oscillator using the Bragg resonator.

A brief description of the main oscillator components is given below and more detailed description of these individual sections are explained in the following sections.

1. **Amplifier**: The amplifier should have a high output power compression point (P_1dBm), a low noise figure and a low flicker noise corner. The gain of the amplifier should be sufficient to cancel the insertion loss of the other elements and therefore guarantee oscillation under all operating conditions. Various SiGe and HBT amplifiers have been tested for their gain, noise figure and P_1dBm point. Residual phase noise measurements have also been made

using a cross correlation measurement system to estimate the flicker noise corner of the amplifiers. For the final oscillator prototype, amplifier using the NBB-402 from RFMD was used. The amplifier had a noise figure of 6dB and the output power compression point was P_1dBm measured at 11.5dBm. The flicker noise corner was estimated to be 26kHz at 3.8GHz.

2. **Resonator**: Two aperiodic Bragg resonators were built with the centre frequency of 9.95 GHz with an unloaded Q *(Q_0)* of 203,603 and a centre frequency of 9.945 GHz with an unloaded Q *(Q_0)* of 199,167.
3. **Mechanical phase shifter**: This was used to set the loop phase shift to N $\times$ 360°. A mechanical phase shifter Aeroflex 980-3 was used which is specified to work from DC-8GHz but still operates well at 10GHz. Semi rigid RG-402 cables were also used to connect the elements of the oscillator.
4. **Output Coupler**: In order to connect to an external device, a broadband 10dB directional coupler from Pasternack has been used which works from 2-18GHz.

In the following sections, the design of the Bragg resonator built in [15] is described. The simulations, design and measurements of various amplifiers using SiGe and HBT transistors operating at 10GHz are also discussed. Finally, the phase noise measurement setup with the phase noise performance has been described.

5.2 Resonator

Resonators at 10GHz are usually made up of dielectric materials such as alumina, sapphire or Barium Tetratitanate. Dielectric materials are usually the most common choice and the maximum unloaded quality factor attainable from a dielectric

resonator is defined by the loss tangent (tanδ) of the dielectric material and the Qxf which is usually a constant for dielectric resonator. Modern dielectric resonators (DR) operating in the TE_{01} mode are capable of providing Q-factors of between 10,000 and 30,000 at 10 GHz. The distributed Bragg resonator can offer a significant increase in quality factor when compared to the dielectric resonators at 10GHz. It is a structure formed by replacing the end and/or side walls of an empty metal cavity with alternating layers of air and dielectric material. The sudden change in dielectric constant at each air dielectric interface causes a partial reflection of the incident electromagnetic wave. If several air-dielectric layers are combined, then more of the energy is reflected back into the central air region of the cavity and kept away from the lossy metal end walls. The reflector section lengths in a Bragg resonator are typically one quarter of the guide wavelength ($\lambda_g/4$) in thickness in order to maximize their reflectivity [55]. The design of the Bragg resonator used in this work has been described in [15] which is a high Q aperiodic arrangement of non ($\lambda_g/4$) of low loss alumina plates with a relative permittivity of $\mathcal{E}_r$=9.5 and a loss tangent of $2x10^5$ at 5GHz. Simulations using the ABCD model suggested that the unloaded Q in a periodic Bragg resonator began to saturate as the number of dielectric plates were increased which led to the exponential decay of the electric field as the cavity end walls are approached and hence six dielectric plates were used for the initial porotype of the resonator. The dielectric plates were enclosed in an aluminum shield which demonstrated an insertion loss of -8.9 dB and a loaded Q (Q_L) 126,810 and the unloaded Q (Q_0) was calculated to be 196,797 with wire loops being used to couple the energy in and out of the cavity.

For the 10GHz oscillators, two aperiodic Bragg resonators were built to have a maximum unloaded Q and the insertion loss was set to 6dB for optimum phase

noise performance. Wire loops were used to couple the energy in and out of the cavity. Since the insertion loss and the Q were very sensitive to the position of the probes, the probes were clamped using a jig as shown in the **Figure 5.2**. A plot of insertion loss versus frequency with a 500 MHz span of the first resonator is shown in **Figure 5.3**. The closest spur is ±40MHz away from the required TE_{011} mode.

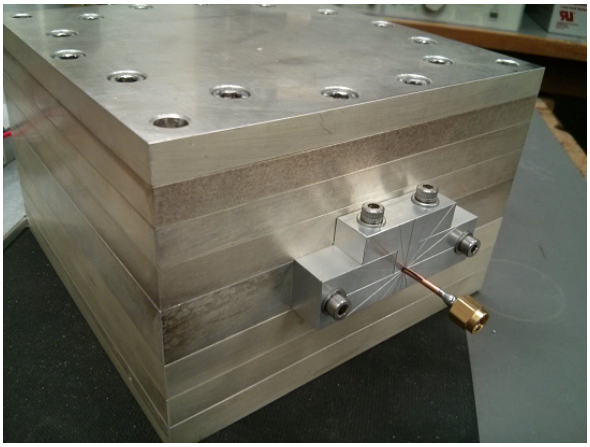

Figure 5.2: Aperiodic 6 plate Bragg Resonator with the clamping mechanism

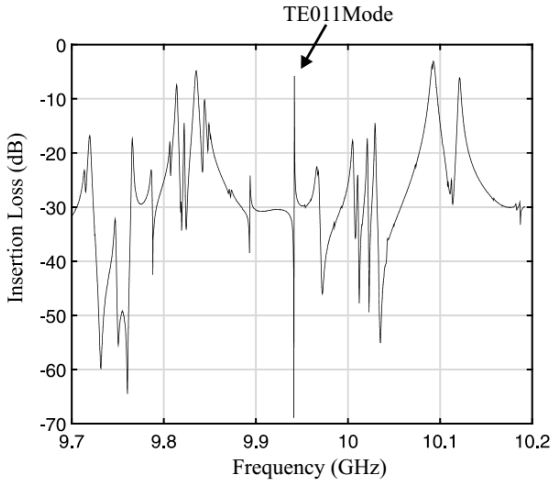

Figure 5.3: Measured Insertion Loss Vs Frequency for a 500MHz span with the required TE_{011} mode.

The span was then reduced to 100kHz to get a more accurate measurement of the insertion loss as shown **Figure 5.4**. The centre frequency can be seen at 9.95 GHz with the insertion loss *(S_{21})* of -6.18 dB with a loaded Q (Q_L) 103,653 and the unloaded Q was then calculated to be 203,603 using **Eq. 5.1**.

$$Q_0 = \left(\frac{Q_L}{1 - |S_{21}|}\right) \qquad \textbf{Eq. 5.1}$$

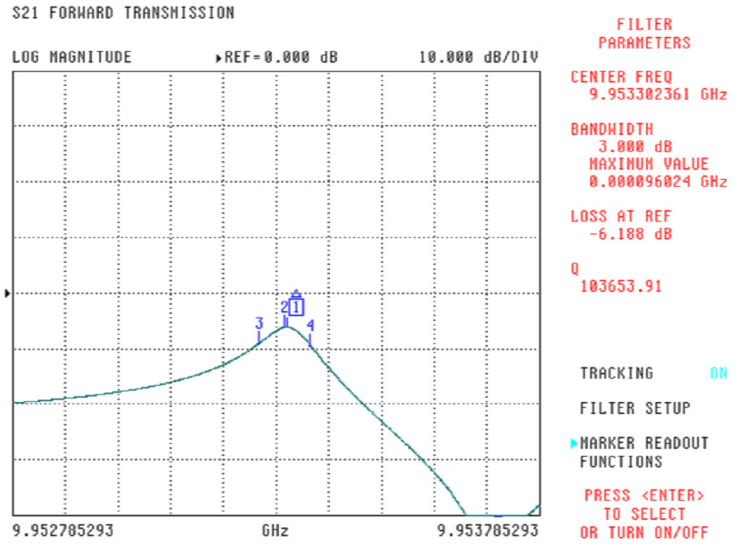

Figure 5.4: Plot of insertion loss (S_{21}) with a 100 kHz span with the loaded Q of 103,653.

Second Bragg resonator was built identical to the first one with a new set of dielectric plates. However, the second Bragg resonator cavity was silver plated with 10µm thickness silver in order to reduce the wall losses and hence increasing the Q. The author assembled the new Bragg resonator and optimised the probe in order to set the correct insertion loss and the loaded Q by adjusting the probes. The insertion loss on the second resonator with silver plated was set to -7.1 dB insertion loss with

a loaded Q (Q_L) of 111,221 as shown in **Figure 5.5** which resulted in a calculated unloaded Q (Q_0) of 199,167.

There are several factors accounting for a lower Q compared to that of the non-silver plated aluminum sections. Firstly, the loss tangent may be larger for the new set of plates. Simulations suggest that if the loss tangent is doubled, the unloaded Q of the resonator changes from 400,000 to 230,000 that suggest that any slight manufacture variation of the loss tangent of the dielectric plates has a significant effect on the unloaded Q. It has to be noted that the loss tangent of $1x10^{-5}$ from the manufacture's data sheet is measured at 5GHz. Secondly, it was also observed that the loaded Q was fairly dependent on the tightening of the screws which would lead in variation of unloaded Q. this might be due to the fact that any uneven metal cavity will have an effect on energy leakage. Any small gaps between the cavity plates will lead to degradation of Q. In addition, if the metal plates were uneven to begin with, the silver plating coating may be also uneven which could lead to energy potentially leak degrading the quality factor. There might be also mode suppression or any other physics effect and needs further investigation.

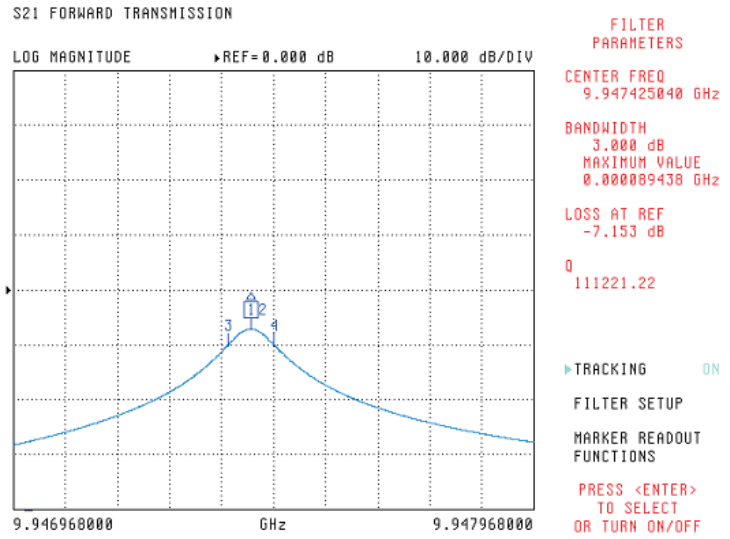

Figure 5.5: Plot of insertion loss (S_{21}) with a 100kHz span with the loaded Q of 111,221.

5.3 Amplifiers

A low noise amplifier with high power with sufficient gain is the requirements of an amplifier in the oscillator to obtain a low phase noise. Also, in the feedback topology of the oscillator, the phase noise performance is limited with the residual noise of the sustaining amplifier and hence it is critical to measure and reduce the residual phase noise of the sustaining amplifier. At microwave frequencies (above 6 GHz), the power available from Silicon or SiGe devices is quite low and hence GaN or GaAs transistors which have much higher output power are a more suitable choice. However they can exhibit high flicker noise corners and hence when used as an active device in an oscillator, the phase noise performance can be at least 30 dB worse due to the increased transposed flicker noise [35] [36] and hence SiGe and HBTs are usually a good choice when close in phase noise of the oscillator has to be improved. Also, a

more recent comparison of the phase noise of various commercial amplifiers which use HBT and SiGe transistors working at X band has been reported and found to have low residual phase noise [87].

Selections of SiGe and heterojunction bipolar transistors (HBTs) are available as seen in **Table 5.1** from a number of manufacturers at 10GHz. The devices are BFP-620F from Infineon Technologies, HBT's NBB-402 and NBB-312 from RFMD, a SiGe transistor BFU-730F from NXP Semiconductor devices and TC 200 from Keysight Technologies were chosen based on the gain, noise figure and power characteristics. Each of these amplifiers was tested for its gain, noise figure, output compression point (P_1dBm) and the flicker noise corner. The following sections discuss the simulations, design and the test of the various amplifiers.

Table 5.1: Transistors which were investigated by the author at 10GHz.

Manufacturer		**Part No**
Infineon Technologies	SiGe	BFP620F
RFMD	InGaP/GaAs MMIC HBT	NBB-402
RFMD	InGaP/GaAs MMIC HBT	NBB-312
NXP	SiGe	BFU-730F
Keysight Technologies	GaAs MMIC HBT	TC-200

5.3.1 Push-Pull Amplifier using the Infineon SiGe BFP620F transistors

From the data sheet, BFP620F transistors from Infineon are SiGe devices that have a gain of 6 dB at 10GHz for a collector current of I_C=50mA and V_{CE}=2V. It also has a noise figure of 1.3dB at 6GHz for a collector current of 5mA. Also, the P_1dBm is 14 dBm specified at 1.8GHz for a V_{CE}=2V and I_C=50mA.

A PSPICE model was imported in Agilent ADS in order to simulate the S parameter response over the required frequency range (6-12GHz). The single stage amplifier is shown in **Figure 5.6** which was designed in a common emitter configuration which incorporates compact bias tees with a shorter upper section. The printed Bias T's are used in order to present high impedance (open circuit) to the RF signal and low impedance at DC. The bias T's consists of a radial stub and an 85Ω ($\lambda_g/4$) element. An Infineon BCR400W active bias controller is used to bias the microwave transistor. This is a low voltage drop device capable of stabilising the bias current of an NPN transistor from 0.2mA to over 200mA and includes temperature compensation elements. The quiescent current is set by R_{EXT}.

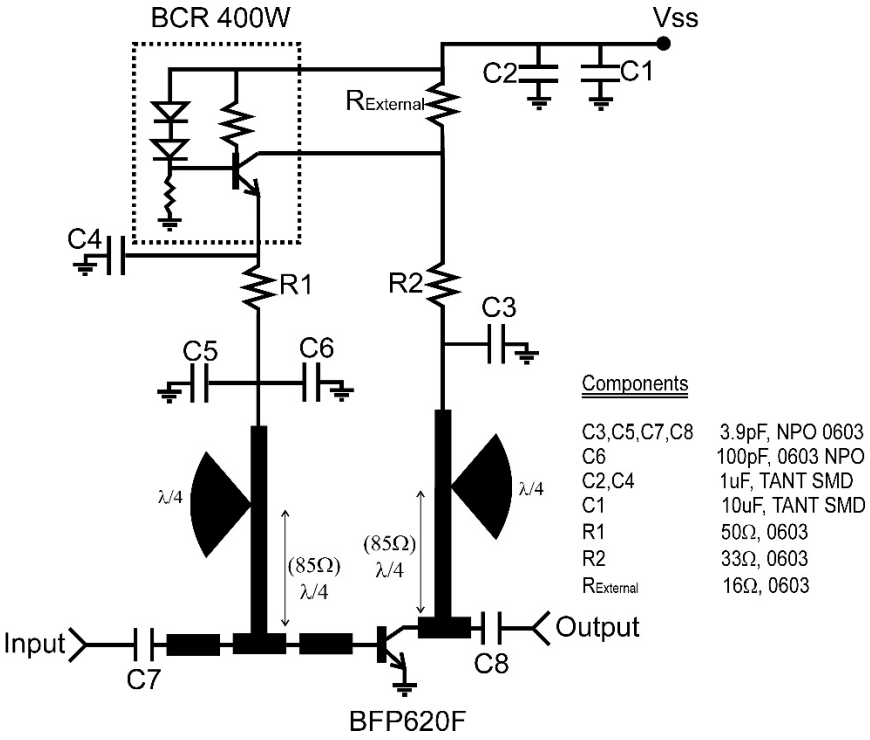

Figure 5.6: Single stage amplifier using BFP620F using the active bias BCR400W.

The amplifier was again simulated for its S parameter response in a series Push Pull configuration since they did not have enough gain at 10GHz. Each arm is then connected and a rat race coupler was used with balanced (180°) outputs. Four of these single stage amplifiers were then combined with the rat race couplers to produce the complete compact push pull amplifier as shown in **Figure 5.7**. The advantage of using a rat race coupler is that it provides better isolation at the input and the output of the amplifier and a 3 dB increase in the output power. Finally, the amplifier was tested for its stability using the K-Δ test as mentioned for the 3.8GHz amplifiers. The amplifiers were unconditionally stable upto 16GHz.

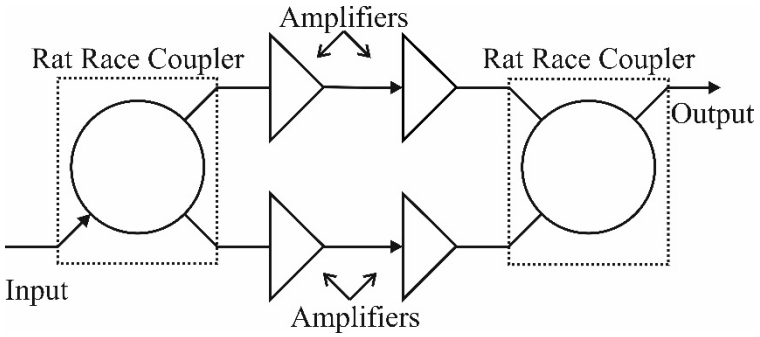

Figure 5.7: Push Pull amplifier configuration using BFP-620F transistors.

The boards were designed using Rogers 3006C PCB boards which have a εr=6.5 with a tanδ of 0.0020. The Push Pull amplifier was then tested for its gain which demonstrates a gain of 10dB at 10GHz with an input return loss of -12.5dB as shown in **Figure 5.8**. The dips in the simulated and measured gain responses are due to the bias tees. Next, the noise figure was measured using an HP8970B noise figure meter using the double side band technique. This instrument only operates up to 1.6GHz so it is necessary to down convert it using a mixer. The HP346B noise source operates up to 18GHz. The noise meter is set to measure the noise figure at

10MHz so this system measures the noise figure of the amplifier at ± 10MHz around the signal generator as shown in **Figure 5.9**. The signals are down converted using a MZ410CR mixer. The device is calibrated from the noise meter to the mixer since the mixer has a loss associated with it. The LO signal is provided by a HP8672A signal generator with a 10dBm output power. A noise figure of 6.2dB was measured at 10GHz using the double side band technique. Finally, the output power compression P_1dBm measurement was done on the Push Pull amplifier using the measurement set up as shown in **Figure 5.10**. A directional coupler was used in order to determine the input power available to the amplifier. Also, a 10dB attenuator was used to protect the power meter. The output compression point P_1dBm was measured to be 10dBm.

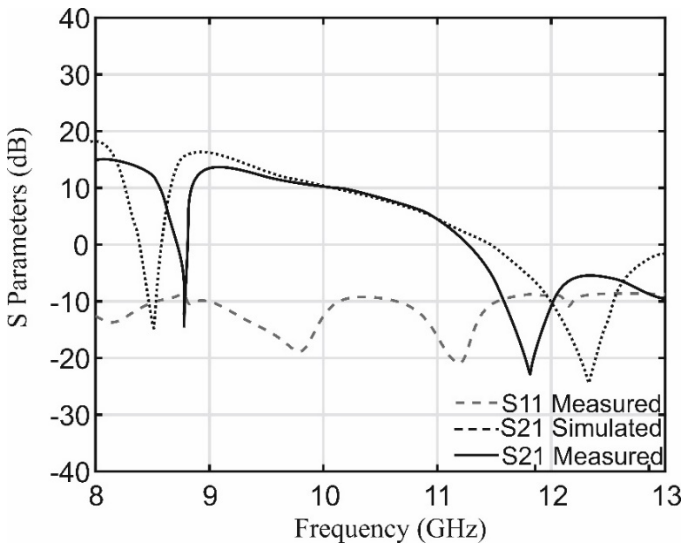

Figure 5.8: Measured S-Parameters for the Push Pull amplifier using SiGe 620F transistors.

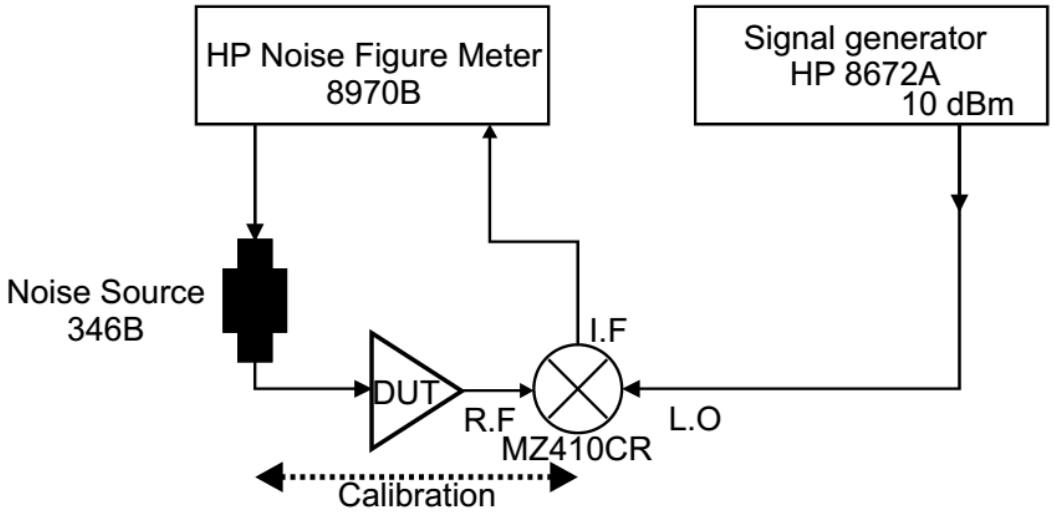

Figure 5.9: Measurement setup to measure the Noise Figure of the 10GHz amplifiers.

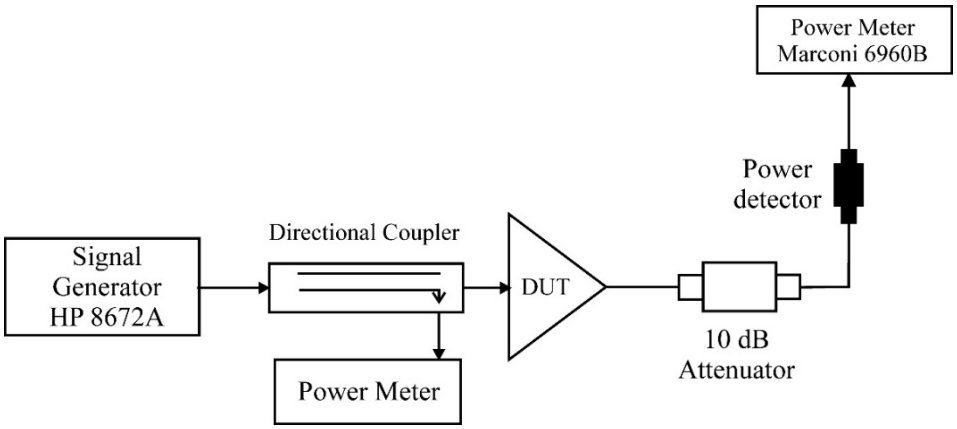

Figure 5.10: Power Measurement Setup for the Push Pull Amplifier at 10GHz.

Finally, a residual phase noise measurement was done on the BFP620F Push Pull amplifier using the cross correlation technique at 3.8GHz as explained in **Section 3.9.7**. Calibration was performed using the single side band method as described in [53] with the help of a directional coupler as shown in **Figure 3.68**. The primary advantage of this method is that non-linearity in both mixers is

accounted for and also the calibration conditions match the measurement conditions as closely as possible. A 3.8GHz oscillator built in the previous chapter which exhibited a phase noise of -153 dBc/Hz at 10kHz offset was used as a reference source since it offered a good low AM noise when compared to a commercial signal generator. This is important since the mixer can only offer about 20dB suppression when operated in a quadrature mode. The high level mixers which operate from 2-18GHz have a power limitation to a maximum of +10dBm in the LO port. Since the output power saturation P_1 dBm for the amplifiers were 10dBm, the power levels were enough to drive the mixers. As the amplifier operates in the saturation region in an oscillator, the residual phase noise measurements were performed at the saturation since the flicker corner is power dependent. For a given input power (P_{in}) and the noise figure (NF.) it is possible to determine the residual noise floor of the device using **Eq. 5.2** when the amplifier is in the linear region. However, the noise floor is likely to increase in case the amplifier is in the saturated region or have any nonlinear affects [54] [27].

$$L(f) = -177 - P_{in} + NF \qquad \textbf{Eq. 5.2}$$

Hence for a given input power level (P_{in}) of 2dBm which was the input saturation point and a noise figure (NF.) of 6dB, the noise floor is estimated to be -173 dBc/Hz using **Eq. 5.2**. The measured noise floor as observed in **Figure 5.11** is -170 dBc/Hz which suggests that the noise figure has been increased under saturation by 3dB. The residual phase noise of the amplifier was measured to be –160 dBc/Hz at 1 kHz offset and –168 dBc/Hz at 10 kHz offset as shown in **Figure 5.11** and the estimated flicker corner of the amplifier was found to be 36kHz.

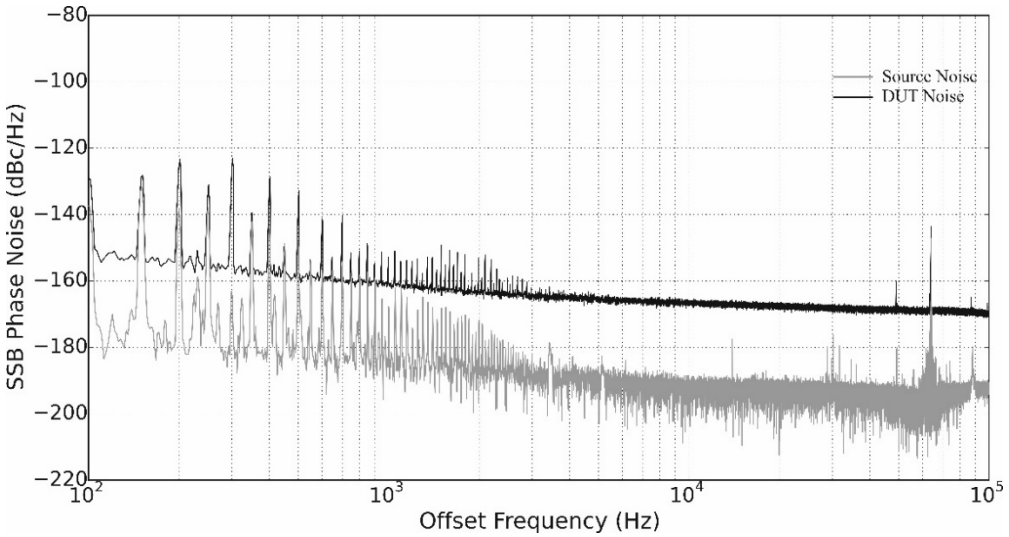

Figure 5.11: Flicker corner of 36kHz for an input power (P_{in}) of 2dBm and a noise figure (NF) of 6dB measured at 3.8GHz.

If these set of transistors were used to build the final oscillator operating at 10GHz, for an overall noise figure of 10dB including the cables, coupler and the mechanical phase shifter and a P_{AVO} of 10dBm, the theoretical phase noise performance would be as seen in **Table 5.2**:

Table 5.2: Predicted theoritical phase noise performance of an oscillator using the Push Pull Amplifier using BFP-620F for a NF=10dB , P_{AVO}=10dBm and Q_o=190,000

Offset Frequency	Theory
1kHz	-120.7 dBc/Hz
10kHz	-150.0 dBc/Hz

5.3.2 Broadband NBB-402 HBT Amplifier

According to the manufacturer's data sheet, NBB-402 from RFMD is a cascadable broadband InGaP/GaAs MMIC HBT amplifier which works upto DC-8GHz but offers sufficient gain of 10dB at 10GHz. It also has a high P_1 dBm point of +15.4dBm at 6GHz and a noise figure of 4.3dB at 3GHz which is desirable to work as an active device in a feedback topology oscillator. Hence amplifiers using NBB-402 transistors were investigated. The S parameters for the transistor at 10GHz is shown in **Table 5.3** which shows a gain of 11.3dB at 10GHz.

Biasing was achieved with the help of an external series resistor and choke inductor to V_{CC} as shown in **Figure 5.12**. This configuration uses a conical inductor as a choke to provide a high impedance at the operating frequency but very low impedance to the DC. The conical shape of the inductor makes it ultra-broad band in response with the ferrite material embedded in order to increase the total inductance [88]. BCL-232JL from Coilcraft which has an inductance of 2.35μH with a current handling upto 270mA was used.

Table 5.3: S-Paramteres for NBB-402 transistor.

S Parameter	Magnitude	Angle
S_{11}	-13.5012	-153.14
S_{21}	+13.5039	+38.78
S_{12}	-16.5228	-6.56
S_{22}	-27.9210	+17.51

The typical S_{21} frequency response is relatively flat and a return loss better than 20dB from 5MHz to 25GHz. Care was taken while soldering the conical inductor to the PCB boards in order not to introduce any parasitic or resonances in the

inductor performance. The V_{DEVICE} was set to 3.8V according to the data sheet and hence the resistor value is determined by **Eq. 5.3**. The collector current I_{CC} was set 52mA for 42Ω resistor in the collector with a 6V power supply.

$$R = \left(\frac{V_{CC} - V_{DEVICE}}{I_{CC}}\right) \qquad \textbf{Eq. 5.3}$$

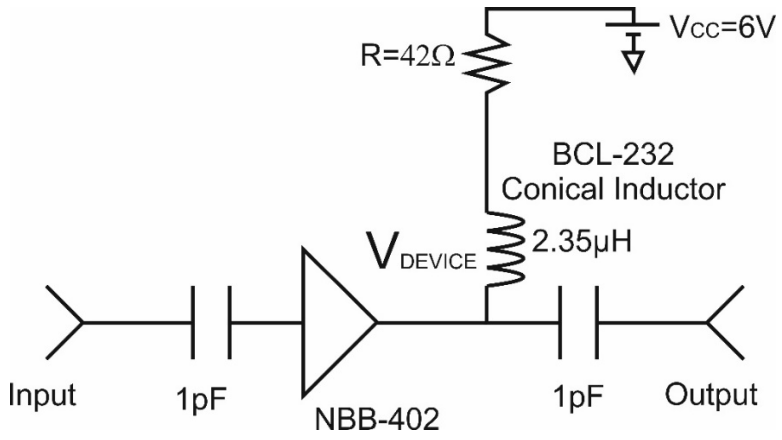

Figure 5.12: Circuit diagram for the NBB-402 amplifier for I_{CC}=52mA.

The circuit was simulated using the S Parameter files available for the transistor and the conical inductor provided by the manufacturer using Agilent ADS for its gain which demonstrated a gain of 10dB with an input return loss of 6dB. The amplifier was also simulated for its stability using the $K-\Delta$ test, which states that a transistor is unconditionally stable if Rollet's condition, K, is greater than unity and the auxiliary condition, $|\Delta|$, is less than unity. As $K>1$ and $|\Delta|<1$ the transistor is unconditionally stable upto 20GHz using **Eq. 3.3** and **Eq. 3.4**. A number of transistors and evaluation boards were obtained from RFMD to measure the gain, noise figure and power characteristics. When the evaluation boards were obtained, it was noticed that they did not have any biasing circuit on them. Hence

the evaluation boards were modified to incorporate a conical inductor and a resistor in order to set the collector current on the transistor as shown in **Figure 5.13**.

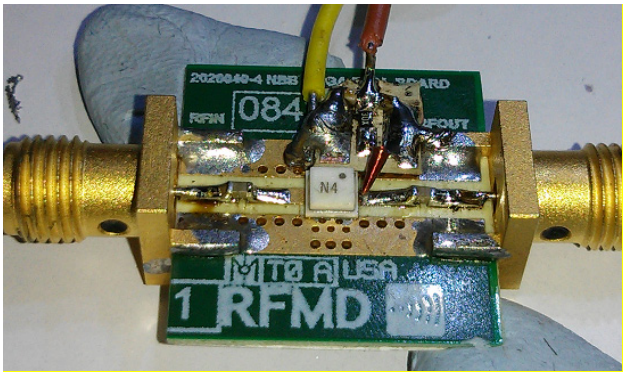

Figure 5.13: Modified evaluation boards using NBB-402 transistor along with a broadband conical inductor BCL-232JL.

The amplifier was tested for its gain, noise figure and output power compression P_1 dBm point at 10GHz. A comparison of the gain and the input return loss for the simulated and measured S-parameters is shown in **Figure 5.14.** A gain of 9.8dB at 10 GHz and an input return loss of -11.0dB were measured which are in close agreement with that of the simulations. Next, noise figure measurement was performed on these amplifiers. A noise figure of 4.9dB was measured at 10GHz using the double side band technique [39]. Finally, the output compression point P_1dBm point was measured to be 12.2dBm suing the same measurement setup used to measure the BFP-620F amplifier.

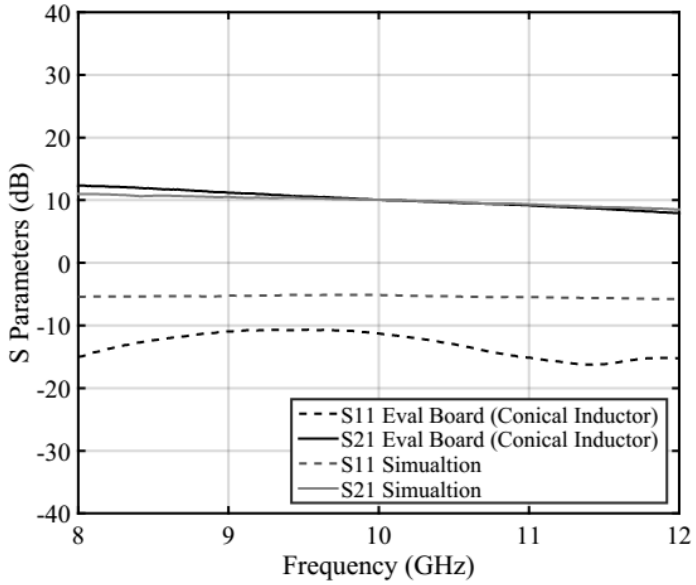

Figure 5.14: Comparison of the S-Parameters of the measured NBB-402 amplifier using the evaluation board to that of the s2p file by RFMD.

Next, a PCB board was designed and fabricated to incorporate the biasing circuit on it as shown in **Figure 5.15**. The amplifier was once again tested for its gain but the measurements agree with that of the evaluation boards with a gain of 9.8dB at 10GHz.

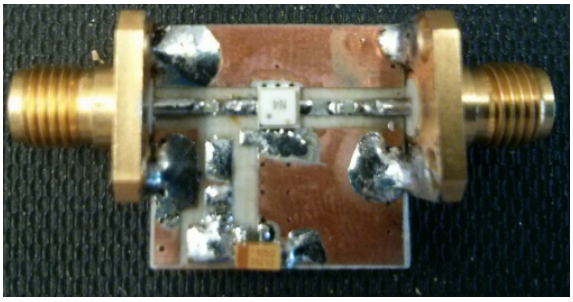

Figure 5.15: NBB-402 with the conical inductor and the biasing circuit.

Finally, boards from Keysight Technologies (Santa Clara) were obtained which used ferrite beads as a choke as shown in **Figure 5.16**. The amplifier was initially designed for a collector current I_C of 52mA with a supply voltage of 9V. The S parameters were measured for the amplifiers with the ferrite bead as shown in **Figure 5.17** and a dip in the gain was observed at 13GHz which was due to the ferrite bead. In order to have a more broadband design, the ferrite bead was replaced with a conical inductor BCL-232JL and the supply voltage was reduced to 6V since it can be operated using lead acid battery. This resulted in changing the resistor from 108.2Ω to 42Ω in order to set the collector current at 52mA.

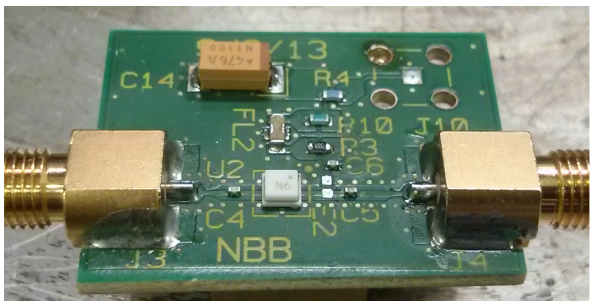

Figure 5.16: 10GHz amplifier NBB-402 transistor along with ferrite bead obtained from *Keysight Technologies, Santa Clara, USA*.

The S parameter comparison for ferrite bead and conical inductor is shown in **Figure 5.17**. The performance of the amplifier was improved with the help of a broadband conical inductor (solid black line) when compared to that of a ferrite bead (dotted grey line). Both set of amplifiers demonstrated similar gain of 10.2dB at 10GHz and a return loss of -8.9dB. The noise figure for the amplifiers was measured to be 4.9dB and the output compression point P_1 dBm of 12.4dBm.

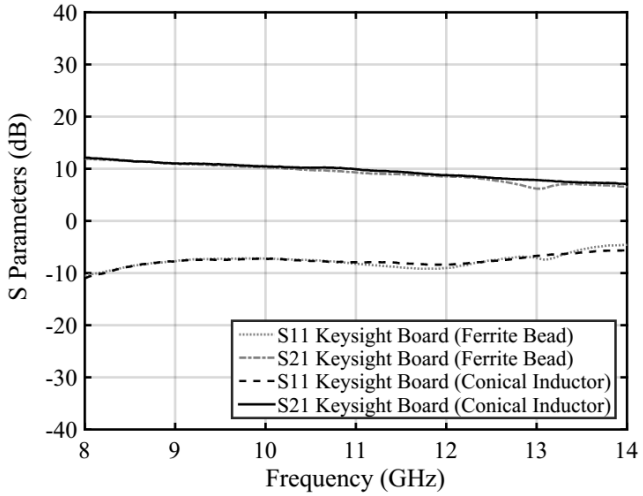

Figure 5.17: Comparison of the S Parameter response for NBB-402 using conical inductors and ferrite beads.

Residual phase noise measurement was performed on NBB-402 amplifiers at 3.8GHz. The noise floor for an input power (P_{in}) of 2dBm, which was the input power of its saturation and a noise figure (NF) of 5dB was estimated to be -174 dBc/Hz using **Eq. 5.2**. The measured residual phase noise is –159 dBc/Hz at 1 kHz offset and -168 dBc/Hz at 10kHz offset as shown in **Figure 5.18** and a flicker corner of 26kHz was estimated using a curve fitting algorithm. **Eq. 5.2** is valid when the amplifier is operated in the linear region and it should be noted that the noise figure is likely to increase when operated in a large signal regime where the amplifier is under saturation or has any nonlinear property [54] [27]. The 2dB increase in the noise floor indicates that the noise figure under saturation has been increased by 2dB as seen in **Figure 5.18**.

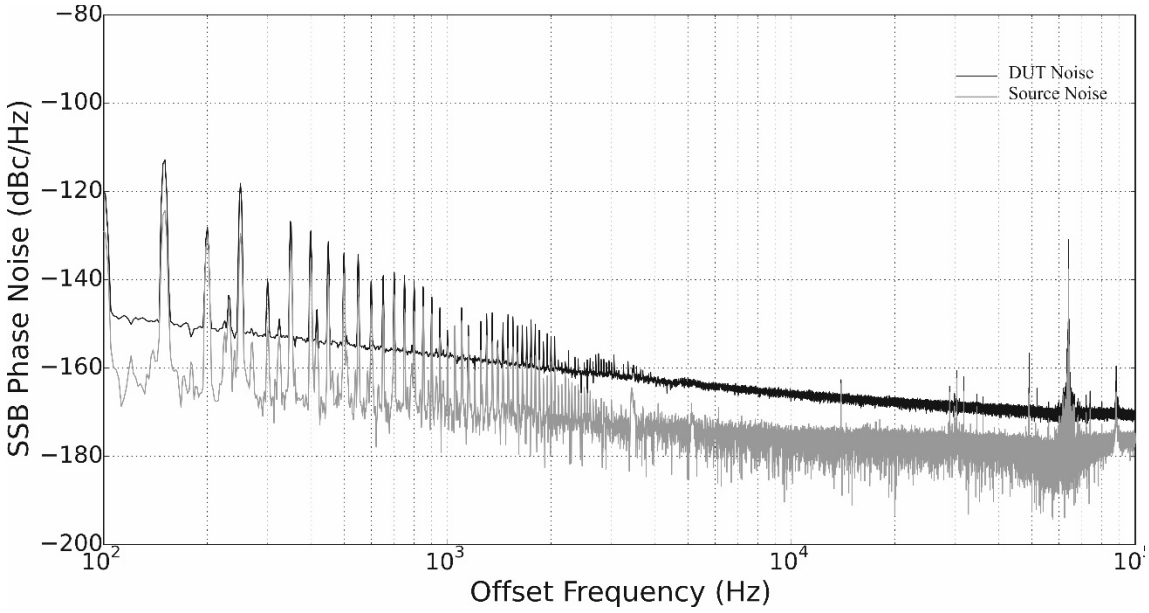

Figure 5.18: Flicker corner of 26kHz for an input power (P_{in}) of 5dBm and a noise figure (NF) of 5dB.

Also, if these transistors were used to build the final oscillator operating at 10GHz with a combined noise figure of the amplifier, mechanical phase shifter, the isolator, directional coupler measured to be 6dB and the P_{AVO} measured to be 12 dBm, the theoretical phase noise performance of the oscillators would be as seen in **Table 5.4**:

Table 5.4: Predicted theoritical phase noise performance of an oscillator using NBB-402 transistor for a NF=6dB, P_{AVO}=12.1dBm, f_c=26kHz and Q_o=190,000

Offset Frequency	Theory
1 kHz	-128.4 dBc/Hz
10 kHz	-156.8 dBc/Hz

5.3.3 Broadband NBB-312 HBT Amplifier

Next, NBB-312 which is also a cascadable broadband InGaP/GaAs MMIC HBT amplifier similar to NBB-402 was obtained from RFMD. It also has a high output compression point of +12dBm at 12GHz but a high noise figure of 4.9dB at 3GHz when compared to NBB-402. These devices were specified to have a gain of 9.7dB from 8-12GHz. Biasing was also similar to that of NBB-402 transistor. It is done with the help of an external series resistor and conical inductor connected to the V_{CC}. The voltage at the collector V_{DEVICE} was set to 4.6V according to the data sheet and hence the resistor value is determined by **Eq. 5.3**. The collector current I_{CC} was set 56mA for 25Ω resistor in the collector with a 6V power supply since it could be used with a lead acid battery as shown in **Figure 5.19**. The footprints of the NBB-302 transistors are similar to that of NBB-402 and hence the same PCB boards were used to test the devices.

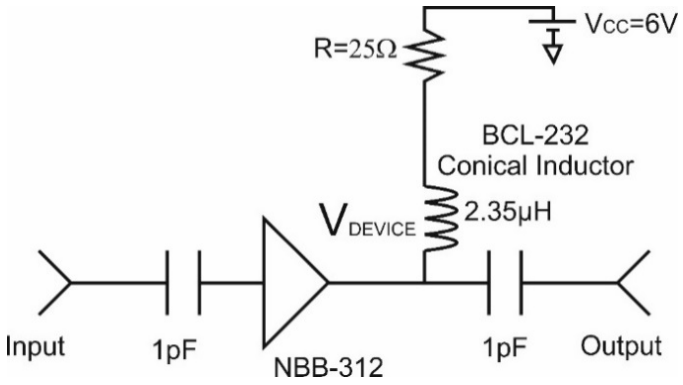

Figure 5.19: Circuit diagram for the NBB-312 amplifier for I_{CC} of 56mA.

These devices were again tested for its gain, noise figure and the output compression points. The comparison of the measured and the simulated S parameter response is shown in **Figure 5.20** and the amplifier demonstrated a gain of 10.3dB at 10GHz with an input return loss of -8.1dB. Finally, the noise figure (NF.) was

measured to be 5.8dB using the double side band method and the P_1dBm point was measured to be 10.1dBm for the NBB-312 amplifier.

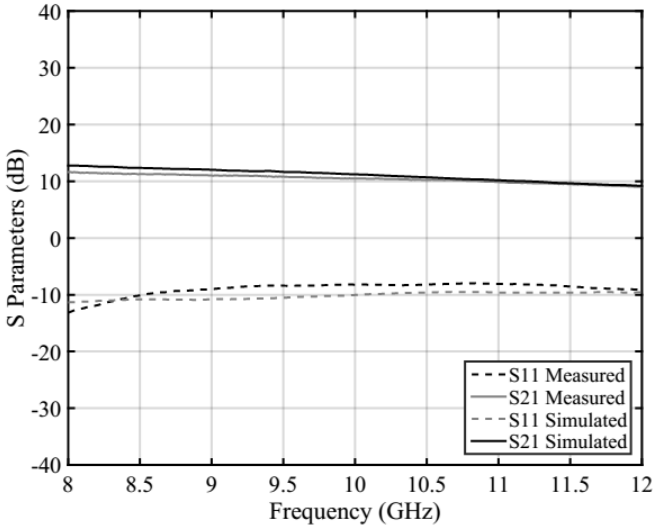

Figure 5.20: S-Parameter response of NBB-312 for *Icc* of 56mA.

If these set of transistors were used to build the final oscillator operating at 10GHz oscillator for a total noise figure for the amplifier, coupler and the mechanical phase shifter measured to be 7dB, the theoretical phase noise performance of the oscillator would be as seen in **Table 5.5**:

Table 5.5: Predicted phase Noise performance of an oscillator using NBB-312 transistor for a NF=7dB, P_{AVO}=10.1dBm and Q_o=190,000

Offset Frequency	Theory
1kHz	-125.4 dBc/Hz
10kHz	-153.6 dBc/Hz

5.3.4 Single Stage Amplifier using SiGe BFU-730F transistors

SiGe transistors from NXP semiconductor devices were investigated at 10GHz. They are NPN devices which are suitable as an active element in an oscillator since they have a low noise figure NF of 1.3dB at 12GHz for a collector voltage of V_{CE} =2V and collector current of I_C=5mA. Also the transistors have a P_1dBm of 12.5dBm at 5.8GHz for a collector voltage of V_{CE} =2.5V and collector current of I_C=15mA. Also, they have a gain of 11.7dB at 10GHz as shown in **Table 5.6**.

Table 5.6: S Parameters for BFU-730F for V_{CE} =2.5V and collector current of I_C=15mA operating at 10GHz.

S Parameters	Magnitude	Angle
S_{11}	0.48725	126.76
S_{21}	3.8559	17.00
S_{12}	0.098556	25.06
S_{22}	0.13962	-100.26

A SPICE model was imported in Agilent ADS and biasing was achieved with the help of a conical inductor BCL-232JL. The schematic of the single stage amplifier is shown in **Figure 5.21**. The collector current I_C is set to 15mA with V_{CE} at 2.5V with the help of the 150Ω and the 16Ω resistors in the collector path and the device was simulated for its gain, noise figure and P_1dBm characteristics. The picture of the amplifier using the conical inductors is shown in **Figure 5.22** using Rogers 4003C substrate with a εr=3.38 with a loss tangent (tanδ) of 0.0027, height of 0.508mm. The simulations suggest a noise figure of 1.9 dB at 10GHz with a P_1dBm at 12dBm. The amplifier was then tested for its gain, noise figure and its output compression point. The amplifier demonstrated a gain of about 9.8dB at 10GHz and an input return loss of 34.3dB as shown in **Figure 5.23**. The noise figure was measured using

the double side band technique described previously and the noise figure was measured to be 2.1dB at 10GHz, 1.9dB at 11GHz, 1.9dB at 12GHz and 2.0 at 13GHz using the double side band method. The P_1dBm measurement setup is similar to the one made to measure the SiGe transistors in section **5.3.1** and the output compression point was measured to be 8dBm at 10GHz.

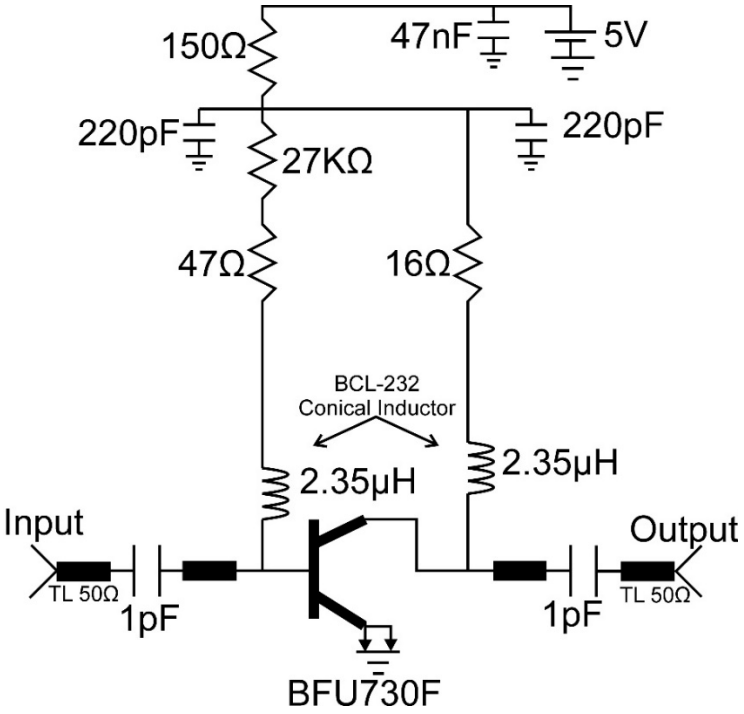

Figure 5.21: Schematic of the 10GHz amplifier using BFU730F transistor for I_c=15mA and V_{CE}=2.5V.

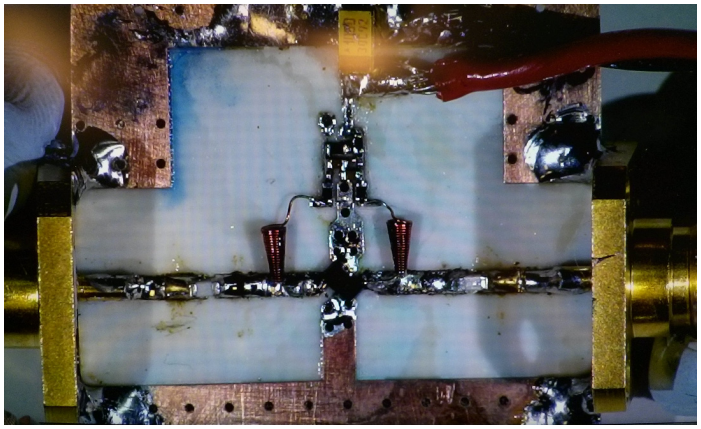

Figure 5.22: Picture of the amplifier with the BFU730F transistor with the BCL-232JL conical inductors for I_c=15mA and V_{CE}=2.5V.

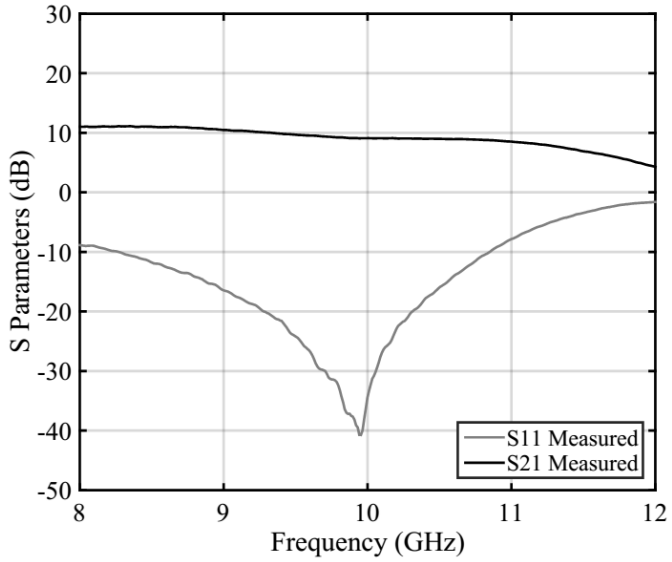

Figure 5.23: Measured S parameters 10GHz amplifier using BFU730F with conical inductors for V_{CE} =2.5V and collector current of I_C=15mA.

Next, residual phase noise measurement was performed on these set of amplifiers to determine the flicker noise at saturation power of 2dBm at 3.8GHz.

The noise floor for an input power (P_{in}) of 2dBm and a noise figure (NF) of 2dB was estimated to be -177 dBc/Hz using **Eq. 5.2**. The measured phase noise is -163 dBc/Hz at 1 kHz offset and -172 dBc/Hz at 10kHz offset as shown in **Figure 5.24** with a flicker corner of 20kHz but the noise floor observed is -175 dBc/Hz which indicates that the noise figure has increased by 2dB under saturation. Note that the noise floor is not quite flat yet so this number could change slightly.

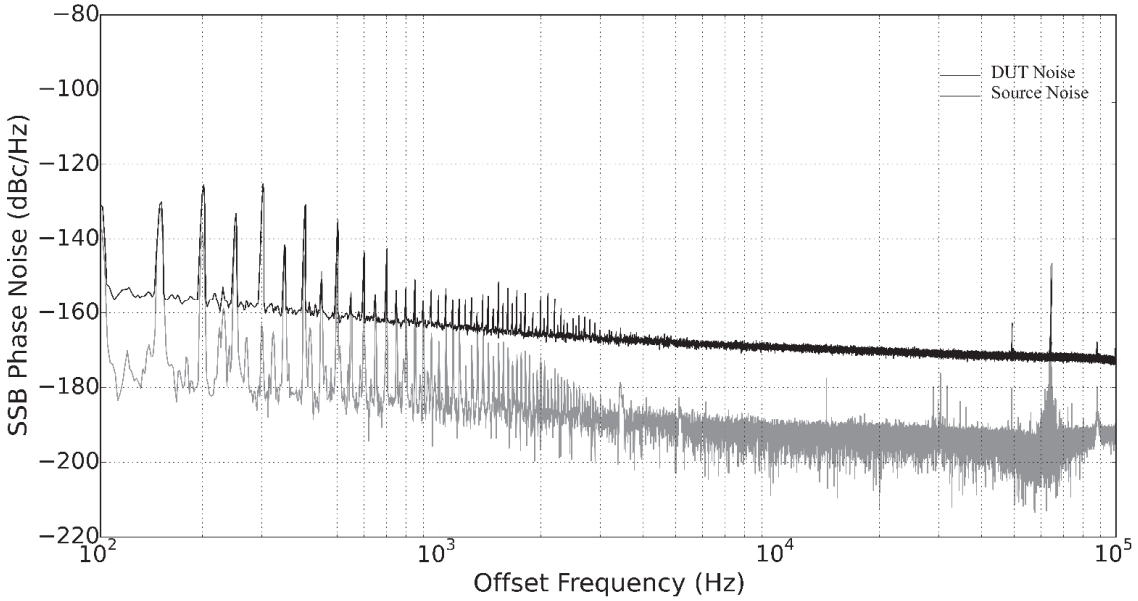

Figure 5.24: Flicker corner of 20kHz for an input power (P_{in}) of 2dBm and a noise figure (NF) of 2dB.

If these set of transistors were used to build the final oscillator operating at 10GHz oscillator for a total noise figure for the amplifier, coupler and the mechanical phase shifter to be 4dB, the theoretical phase noise performance of the oscillator with flicker corner f_c of 20kHz is shown in **Table 5.7**:

Table 5.7: Predicted theoritical phase noise performance of an oscillator using BFU730F transistor for a NF=4dB, P_{AVO}=7dBm and Q_o=190,000

Offset Frequency	Theory
1kHz	-120.9 dBc/Hz
10kHz	-150.6 dBc/Hz

5.3.5 TC200 Amplifier

The TC200 device/amplifier was obtained from Keysight Technologies which is an HBT feedback working from DC to 20 GHz which has a stated gain of 10.2dB at 10GHz with a noise figure of 7dB at 10GHz and P1dBm of 11.7dBm at 10GHz. The picture of the device is seen in **Figure 5.25**. The boards were modified to have a DC block at the input and the output of the amplifier. The Vsupply used was 5V and hence no biasing was used as mentioned in the data sheet.

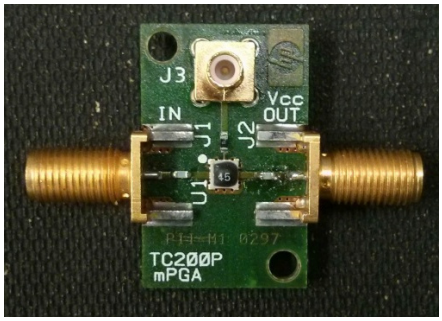

Figure 5.25: Picture of the TC200 Amplifier board obtained from Keysight.

The amplifier was tested for its gain, noise figure and its output compression point. The amplifier demonstrated a gain of about 8.1dB at 10GHz. The noise figure was measured using the double side band technique. The noise figure was measured

to be 7.9dB at 10GHz. The output 1dB compression point was measured to be 11.0dBm at 10GHz. The measured S parameters for the TC200 amplifier measured at York, are shown in **Figure 5.26** and the theoritical phase noise performance of the oscillators if these devices were used as an active lement is shown in **Table 5.8**.

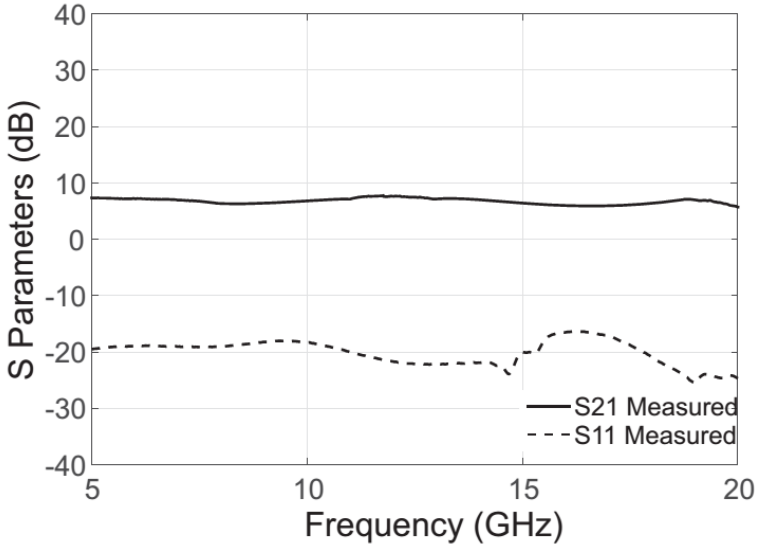

Figure 5.26: Measured S parameters using the TC200 amplifier at 5V power supply.

The residual phase noise measurements were not carried out this device since these devices were obtained very late from Keysight.

Table 5.8: Predicted theoritical phase noise performance of an oscillator using TC200 transistor for a NF=9dB, P_{AVO}=11dBm and Q_o=190,000

Offset Frequency	Theory
1kHz	-119.9 dBc/Hz
10kHz	-149.6 dBc/Hz

Table 5.9: Compariosn of various amplifiers with NF, P_1dBm points, residual phase noise of the amplifiers at 10kHz and the theroritical phase noise when used in the oscillators at 10kHz.

Transistors	Measured Gain at 10 GHz	Measured Noise Figure at 10GHz	Output compression point P_1(dBm)	Residual phase noise at 10kHz (dBc/Hz)	Predicted Theoretical Phase noise of the oscillator at 10kHz (dBc/Hz)
BFP620F	10	6.2	10	–168	-150.0
NBB-402	**9.8**	**4.9**	**12.2**	**-168**	**-156.8**
NBB-312	10.8	5.3	10.1	-165	-153.6
BFU-730F	9.8	2.1	8	-172	-150.6
TC200	8.1	7.9	11	Not Measured	-149.6

Table 5.9 summarises the various amplifiers built in this research work. It can be early seen that there are a number of SiGe and HBTs that offer can really low phase noise at X band frequencies. Based on the output compression point, noise figure and the flicker noise corners of the devices tested, the NBB-402 from RFMD was a suitable choice in an oscillator since the theoretical phase noise of the oscillators would be -156.8 dBc/Hz at 10kHz offset. This was the lowest possible noise that could be obtained from the available devices. Hence this was chosen to be an active element in the feedback topology oscillator.

5.4 Phase Noise Measurement of the 10GHz oscillators

The theoretical phase noise obtained using any of the above amplifiers in oscillators is significantly lower than any commercial phase noise measurement systems and hence it is therefore necessary to mix two oscillators and measure the low frequency beat signal. When comparing the various amplifiers designed above, the lowest theoretical phase noise was obtained was using the NBB-402 transistors and hence it was used as an active element in the oscillator. Phase noise measurement is carried as described in section 3.7 using the beat frequency method where the two oscillators, Oscillator 1 had a frequency of 9.95GHz and Oscillator 2 had a frequency of 9.945GHz are mixed using a mixer MZ410CR to produce a beat frequency of 4.6MHz. The LO drive level for the mixer is +10dBm. It is necessary to use the beat frequency since Symmetricom can only measure up to 30MHz. Since the output power from the oscillators was limited to 1.2dBm, a Push Pull amplifier built using the Infineon SiGe transistors BFP620F in **Section 5.3.1** was used as a pre amplifier to drive the mixer. The phase noise of this signal was measured using a Symmetricom 5120A opt 01 phase noise analyser as shown in **Figure 5.27**.

The theoretical phase noise was calculated using **Eq. 5.4** for two oscillators. Parameters values used for the calculation of the theoretical phase noise of the oscillator using the NBB-402 transistors are shown below:

T: The room temperature in Kelvin T=293 K

F_A*:* The combined noise figure of the amplifier, mechanical phase shifter and the directional coupler, measured to be 6.2dB.

Q_L: Loaded Q of the resonator=95,000

Q_0: Un-loaded Q of the resonator=190,000

P_{AVO}: Power measured at the input of the resonator=11.5dBm

f_o: frequency of oscillation, 10GHz

f_c: Flicker Frequency, measured to be 26kHz for the NBB-402 amplifier measured at 3.8GHz

Δf: Offset frequency

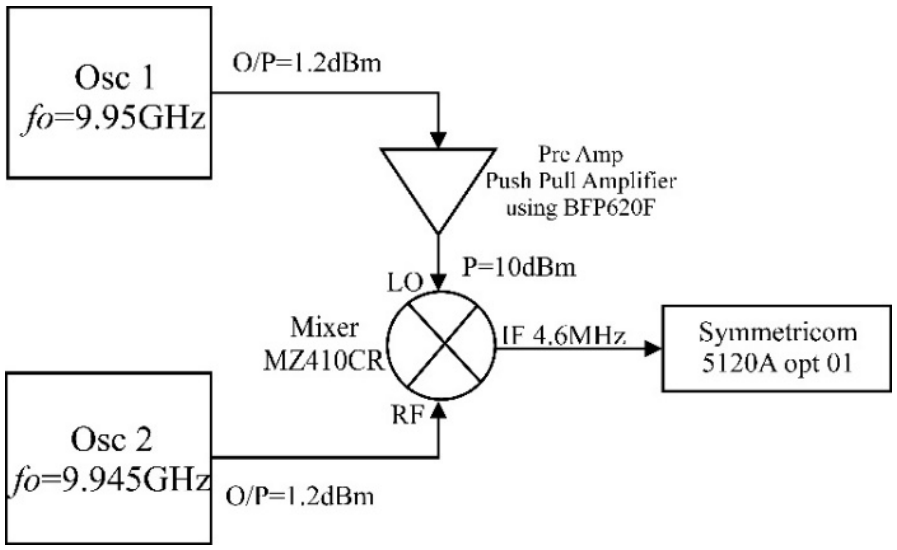

Figure 5.27: Block Diagram of the measurement setup for the 10GHz Bragg resonator oscillators.

$$L(f) = 20\log_{10}\left[\frac{F_1 kT}{2C_0P_1} + \frac{F_A kT}{2P_{AVO}}\left[\frac{1}{\left(1-\frac{Q_L}{Q_0}\right)^2}\right]\left(1+\frac{f_c}{f}\right) + \frac{F_A kT}{8(Q_0)^2\left(\frac{Q_L}{Q_0}\right)^2\left(1-\frac{Q_L}{Q_0}\right)^2 P_{AVO}}\left(\frac{f_0}{f}\right)^2\left(1+\frac{f_c}{f}\right)\right] \quad \textbf{Eq. 5.4}$$

The oscillators were enclosed in screened metal box to shield them against any electromagnetic interferences and also battery powered in order to remove any

spurs at lower frequencies. Initial phase noise of -121.7 dBc/Hz at 1kHz and -150.5 dBc/Hz at 10kHz was measured as shown in **Figure 5.28**. There are a large number of low frequency spurs. These are believed to be caused by the vibrations since the dielectric alumina plates just rest in the cavity under gravity and any vibrations have an effect on the frequency of operation.

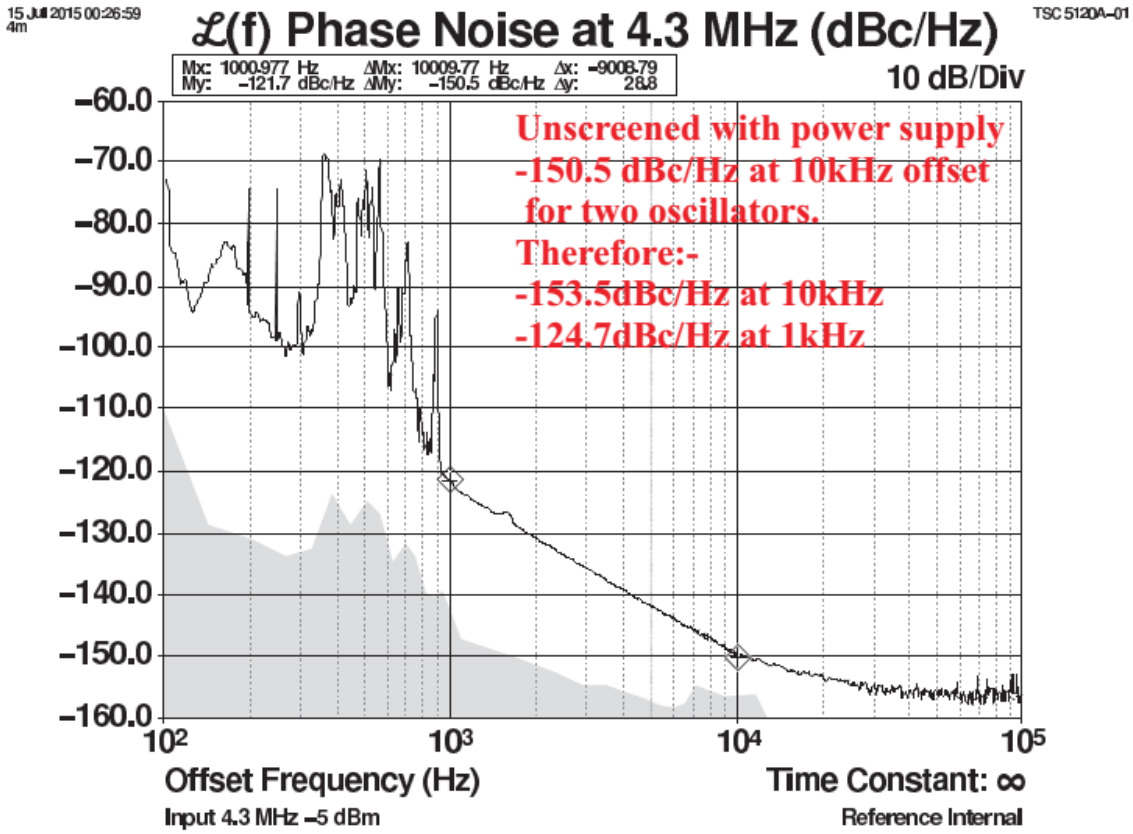

Figure 5.28: Initial Phase Noise measurement of the 10GHz oscillators.

Hence the oscillators were wrapped in bubble wrap and then the entire box was made to rests on inner inflated tubes in order to dampen any mechanical vibration as shown in **Figure 5.29**. Finally, the phase noise measurement was performed on these oscillators.

Figure 5.29: 10GHz battery operated oscillators screened in a metal box and resting on a set of tubes in order to dampen any mechanical vibrations.

A phase noise of -120.6 dBc/Hz at 1kHz and -149.5 dBc/Hz at 10kHz was measured as shown in **Figure 5.30**. It has to be noted that since the phase noise of two oscillators are being measured, it is therefore necessary to subtract 3 dB from the measured result. Hence a phase noise of -123.6 dBc/Hz at 1kHz and -152.5 dBc/Hz at 10kHz was measured for the oscillators operating at 10GHz. **Table 5.10** shows the comparison of the performance of the oscillators operating at 10GHz between the theory and the measurement.

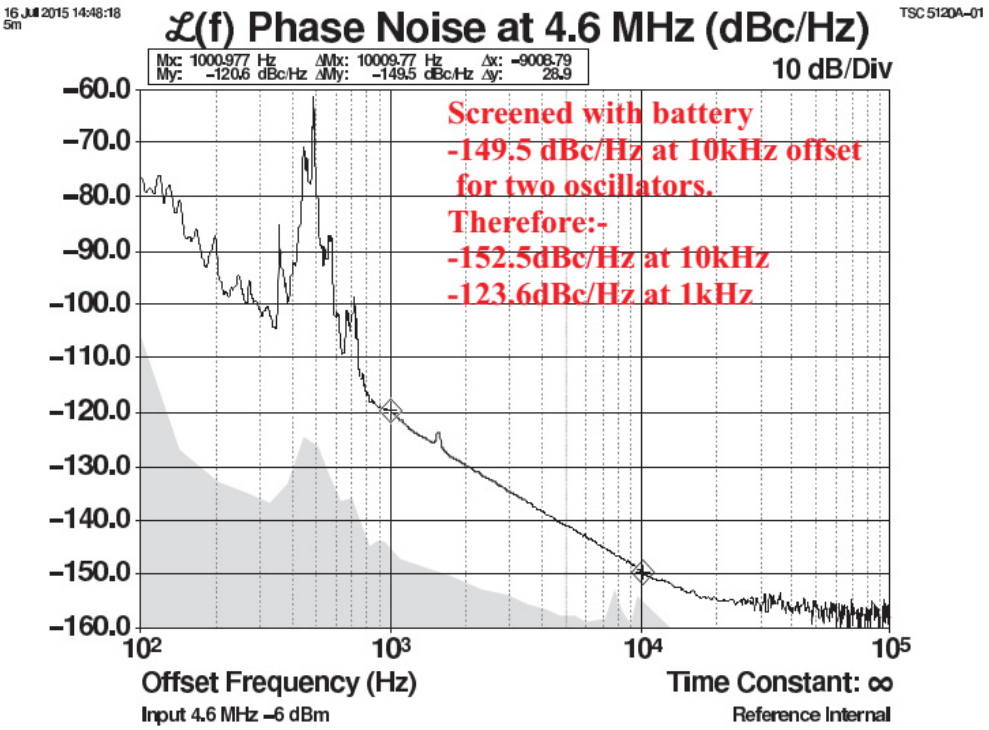

Figure 5.30: Phase Noise of the 10GHz band oscillator using NBB-402 transistors enclosed in a metal box to resting on the tubes to reduce the vibrations.

Table 5.10: Oscillator opearting at 10GHz comparison with the theory (flicker noise corner of 26kHz measured at 3.8GHz)

Offset Frequency	Theory	Measurement
1kHz	-127.4 dBc/Hz	-123.6 dBc/Hz
10kHz	-155.1 dBc/Hz	-152.5 dBc/Hz

The theoretical noise for the two oscillators was calculated to be -155.1 dBc/Hz at 10kHz and -127.4 dBc/Hz at 1kHz respectively. There is a deviation of 3-4dB in terms of the measured phase noise from that of the theory. This can be

explained due to the fact that the large signal noise figure of the amplifier was measured at 3.8GHz instead of 10GHz. If we assume the large signal noise figure of the amplifier under saturating conditions along with the phase shifter, cables and the mechanical shifter had increased by 3dB, then the measured phase noise of the oscillator would tie in with the theoretical phase noise. The other possibility is that if the flicker noise of the amplifier were increased from 26kHz measured at 3.8GHz to 50kHz at 10GHz, the theory would be -123.8 dBc/Hz at 1kHz offset and -153.6 dBc/Hz at 10kHz offset which be in perfect agreement with that of the measurements. In order to know which is accounting for the 3-4dB deviation in phase noise, residual phase noise measurements needs to be performed at X band frequencies with different power levels.

5.5 Conclusions

In this chapter, the design and construction of oscillators operating at 10GHz which uses a Bragg resonator with an unloaded Q of 190,000 is presented which used a NBB402 amplifier with a noise figure of 6dB and the amplifier output 1dB compression point of 12dBm which had a flicker noise corner of 26kHz at 3.8GHz. The amplifier had a residual phase noise of -159 dBc/Hz at 1 kHz offset and -168 dBc/Hz at 10kHz offset. A phase noise of -123.6 dBc/Hz at 1kHz and -152.5 dBc/Hz at 10kHz was measured at 10GHz using the NBB-402 devices. To achieve the low phase noise for the oscillator, several amplifiers were designed and tested for gain, noise figure, output 1dB compression points. In addition, residual phase noise measurements have been made using the cross correlation measurement system to determine the flicker noise corner for these amplifiers.

CHAPTER 6

CONCLUSIONS AND FUTURE WORK

The main objectives of this research have been to develop ultra-low noise oscillators at 3.8GHz and at 10GHz and high Q tunable Bragg resonators for oscillator applications. The current results and the suggestions for future research work are discussed in the following sub-sections.

6.1 3.8GHz Oscillator

The first prototype built for Selex-ES included vibration measurements with a reasonable phase noise. The phase noise for the first 3.8 GHz prototype oscillator was -117 dBc/Hz at 1kHz offset and -150 dBc/Hz at 10kHz offset. Two types of vibration sensitivity measurements were performed. Spot frequency measurements in the X, Y and Z axes of 0.2g at 100Hz, 500Hz & 1500Hz and random in all three axes at 0.7g rms from 10Hz to 2kHz were performed. The vibration sensitivity (Γ_i) varied from 1.33×10^{-7} to 8.51×10^{-9} per g depending on the axis and the frequency of the vibration. Perhaps, the mounting of the resonator on an alumina tube and the use of semi rigid cables were believed to had an effect on these measurements.

The second prototype was a modular compact oscillator was then developed which demonstrated a significantly improved phase noise performance of -125.6 dBc/Hz at 1kHz offset and -153 dBc/Hz at 10kHz offset. This is the lowest noise reported in the literature in this frequency band using a dielectric resonator built at University of York. A new electronic phase shifter was designed in order to handle higher power levels and a mechanical phase shifter was also incorporated in this prototype to eliminate the use of semi rigid cables. The improved performance is mainly due to increase in the power level of the amplifier and the overall reduced noise figure. Finally, residual phase noise measurement of the amplifier was made using a broadband cross correlation phase noise measurement system developed at University of York and the amplifier has a flicker noise corner of 12.7kHz. The theoretical and the measured phase noise of these oscillators are within 0.5dB accuracy.

The following recommendations are made for the future research on the 3.8GHz oscillators. The main area of research would be on amplifier design which involves increasing the output power, reducing the noise figure using SiGe transistors. The output of the amplifiers using SiGe transistors can be increased by using an 8-way splitter, which would potentially increase the output power by 9dB, ignoring the losses within the stages. A new family of SiGe transistors from NXP devices such as BFU690F, BFU730F SiGe devices are ideal choices for such applications. The noise figures of these devices are as low as 0.8dB and hence noise figure can be reduced to 1.5dB (amplifier plus other elements) by low noise matching if necessary, which would be an additional 4dB, which adds up to 10dB improvement in the total phase noise. A phase noise performance of -163 dBc/Hz at 10kHz is easily achievable for the same unloaded factor of 19,000. Also, these devices can be used in

single stage instead of series which potentially would reduce nonlinear effects on the amplifier when it is under saturation and 1/f residual noise of the amplifiers can also be improved by some feedforward techniques. A 10dB improvement in phase noise would produce the lowest phase noise of the oscillators in the 4GHz frequency band which would be comparable to oscillators incorporating sapphire resonators present in the literature.

6.2 Tunable High Q Bragg Resonator

The best performance achieved was a spurious free tuning range of 1% at 10GHz with a maximum unloaded Q of 81,650 after several iterations to the design of the cavity. The insertion loss varies from -3dB to -6.4dB while the unloaded Q varies from 61,020 to 81,650 over the tuning range and the spurious modes were 0.17%-0.41% away from the required mode.

One of the key challenges in tunable resonators would be to maintain a constant spurious free range with a reasonable high quality factors over the tuning range. Very few resonators in the literature have a constant bandwidth without degrading the quality factor and hence further research on designing resonators having spurious free responses is required. One such way that has been suggested is to reshape the conventional dielectric resonator by removing dielectric material in the region where the field strength is high for the spurious modes [13], this could then be potentially used for Bragg resonators. Also, in the current design, some of the soldered areas of the resonator are directly exposed to the high field regions degrading the quality factor. This can be further improved by new techniques in the construction of the cavity with a possibility of silver plated copper bellows along

with silver solder paste to reduce the end wall losses. Finally, tunable oscillators using these Bragg resonators could be built which would potentially demonstrate a phase noise in the range of -147dBc/Hz to -140dBc/Hz at 10 kHz offset for a tuning range of 1% at 10 GHz. These results would be start of the art for a tunable 10 GHz oscillator.

6.3 10GHz Bragg Resonator Oscillator

Low noise oscillators utilising Bragg resonators have been built at 10GHz. The oscillator demonstrates a phase noise of -123.6 dBc/Hz at 1kHz and -152.5 dBc/Hz at 10kHz. To achieve the low phase noise for the oscillator, several amplifiers utilising SiGe and HBTs transistors were simulated, designed and tested for gain, noise figure and output compression points. Also, residual phase noise measurements have been made using the cross correlation measurement system to determine the flicker noise corner for these amplifiers at 3.8GHz oscillator built in the chapter 3 since it had low AM and PM noise when compared to the commercially available signal generators at the time of measurements. Based on these measurements, NBB-402 from RFMD was used as an active device for the oscillator which has a flicker noise of 26kHz at 3.8 GHz. The residual phase noise of the amplifier was measured to be -159 dBc/Hz at 1kHz and -168 dBc/Hz at 10kHz. There is a 2-3dB deviation in the measured phase noise with that of the theory. However, while performing phase noise measurements it was observed that the oscillators were very sensitive to vibrations and hence had to be placed on tyre inner tubes filled with air in order to dampen the vibrations. It would be interesting to know that the phase noise measurements would tie in when the flicker noise is changed from 26kHz to 50kHz

The Author believes that the future research should concentrate on increasing the quality factor of Bragg resonators. A new resonator design in collaboration with Keyisght Technologies, Santa Clara is being implemented for the cavity. This cavity will be constructed using Oxygen Free Copper which exhibits a higher electrical conductivity than standard Copper. The dielectric plates which are the main reason for vibrations are held in position using Spira-Gasket both to provide an electromagnetic seal and to hold the plates in place with low vibration sensitivity. This material is typically used for EMC shielding and is constructed from Beryllium-Copper. Finally, an overall improvement in the amplifier design should be investigated by primarily concentrating on using various power combing techniques and in improving amplifiers noise figures. Also, residual phase noise measurements should be performed at 10 GHz in order to determine the flicker noise corner for these devices. Simulations suggests that a parallel amplifier which uses the 8-way splitter could be used for a 9dB improvement in phase noise at 10 GHz. This would be comparable to oscillators using cryostat sapphire resonators having a Q of few billions present in the literature.

APPENDIX A

A.1 Resonator Experiments

A.1.1 Curved Coupling Probes

A different set of probes were simulated for the same enclosure and the same set of simulations. The top view of the modelled resonator can be shown in the **Figure A.1**.

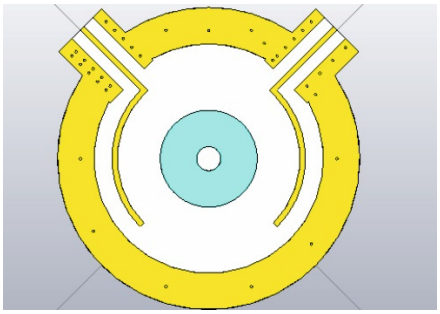

Figure A.1: CST model of the Curved transmission lines.

A new board was fabricated where the micro strip lines were curved instead of straight as shown in **Figure A.2**. They were initially 16mm in length. The insertion loss was measured using the network analyser and was found to be -4.632dB with a loaded Q of 7991. The unloaded Q was calculated to be 19,228. The probe lengths were further reduced by a 1 mm at a time to see the variation of the insertion loss and the loaded Q as seen in **Figure A.3**. The value decreases to be -12.783dB when they were cut 15mm from the initial lines.

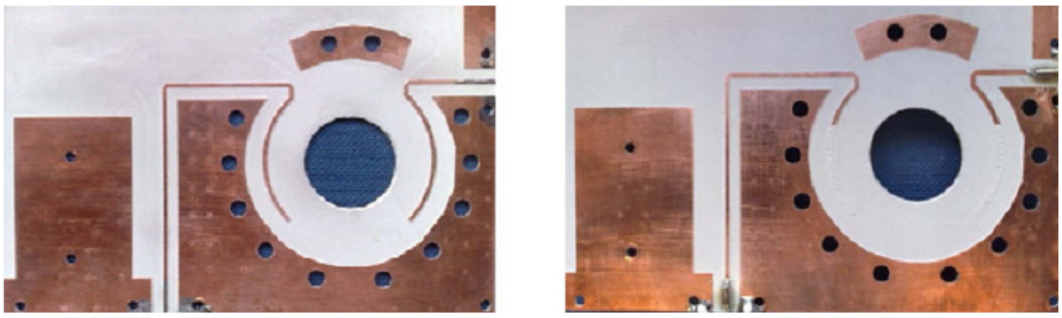

Figure A.2: Curved Micro Strip coupling lines for resonator.

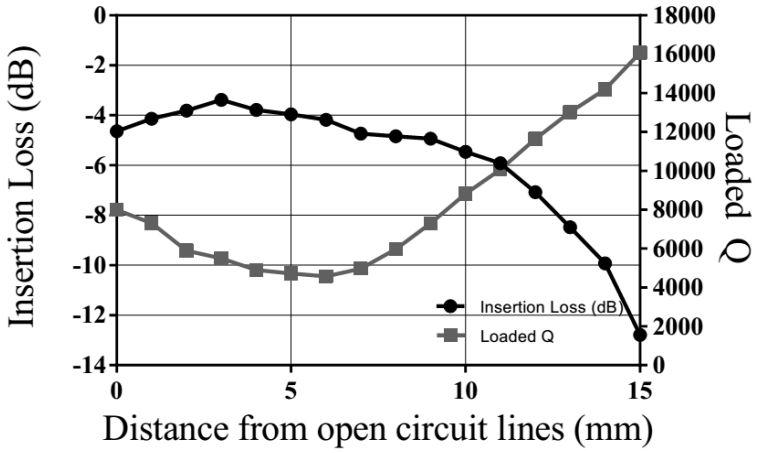

Figure A.3: Plot of Insertion Loss/Loaded Q vs Distance of the curved coupling transmission lines.

A.2 One Port Measurements

Figure A.4: Series LCR resonator circuit.

The impedance of a series LCR circuit is given by **Eq. A.1**:

$$Z = j\omega L + \frac{1}{j\omega C} + R \qquad \textbf{Eq. A.1}$$

The quality factor of the circuit is given by **Eq. A.2**:

$$Q = \frac{\omega L}{R}$$
$$R = \frac{\omega L}{Q} \qquad \textbf{Eq. A.2}$$

For the resonant frequency, the quality factor is given by **Eq. A.3**:

$$Q = \frac{1}{\omega_0 CR}$$
$$R = \frac{1}{\omega_0 CQ} \qquad \textbf{Eq. A.3}$$

When the impedance in **Eq. A.1** is normalized and using **Eq. A.2** and **Eq. A.3** we get:

$$\frac{Z}{R} = j\omega \frac{L}{R} + \frac{1}{j\omega CR} + 1 \qquad \textbf{Eq. A.4}$$

$$\frac{Z}{R} = j\omega \frac{LQ}{\omega_0 L} + \frac{\omega_0 CQ}{j\omega C} + 1 \qquad \textbf{Eq. A.5}$$

$$\frac{Z}{R} = jQ\left(\frac{\omega}{\omega_0} - \frac{\omega_0}{\omega}\right) + 1 \qquad \textbf{Eq. A.6}$$

As the frequency is changed, at the half power frequency, the absolute part of the reactance is resistive and hence:

$$\frac{Z}{R} = 1 + j \qquad \textbf{Eq. A.7}$$

Now the complex reflection coefficient is given by:

$$\begin{aligned}
\rho &= \left(\frac{\frac{Z}{R} - 1}{\frac{Z}{R} + 1}\right) \\
&= \left[\frac{(1+j) - 1}{(1-j) + 1}\right] \\
&= \frac{j}{2+j} \\
&= \left(\frac{j}{2+j}\right)\left(\frac{2-j}{2-j}\right) \\
&= \frac{2j - j^2}{5} \\
&= \frac{2j+1}{5} \\
&= 0.2 + j(0.4)
\end{aligned} \qquad \textbf{Eq. A.8}$$

The magnitude of the reflection coefficient is then:

$$|\rho| = 0.447$$

Hence return loss is given by: $R.L$=-20log($|\rho|$)=-7dB

The measured one port measurement for the dielectric resonator is shown in **Figure A.4**. The 7dB bandwidth is 206kHz which translated into an unloaded Q of 18,495 which is in agreement with the two port measurements.

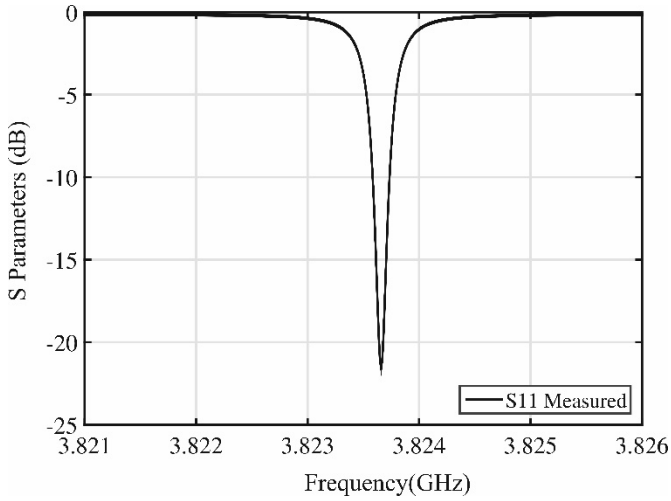

Figure A.5: Measured resonator response using one port.

A.3 Vibration Measurements

The FSUP spectrum analyser plots showing the induced sideband levels $L(f_v)$ caused by vibration on the X, Y and the Z axis at 100 Hz, 500 Hz, 1500 Hz: are shown in **Figure A.6**, **Figure A.7** and **Figure A.8** respectively.

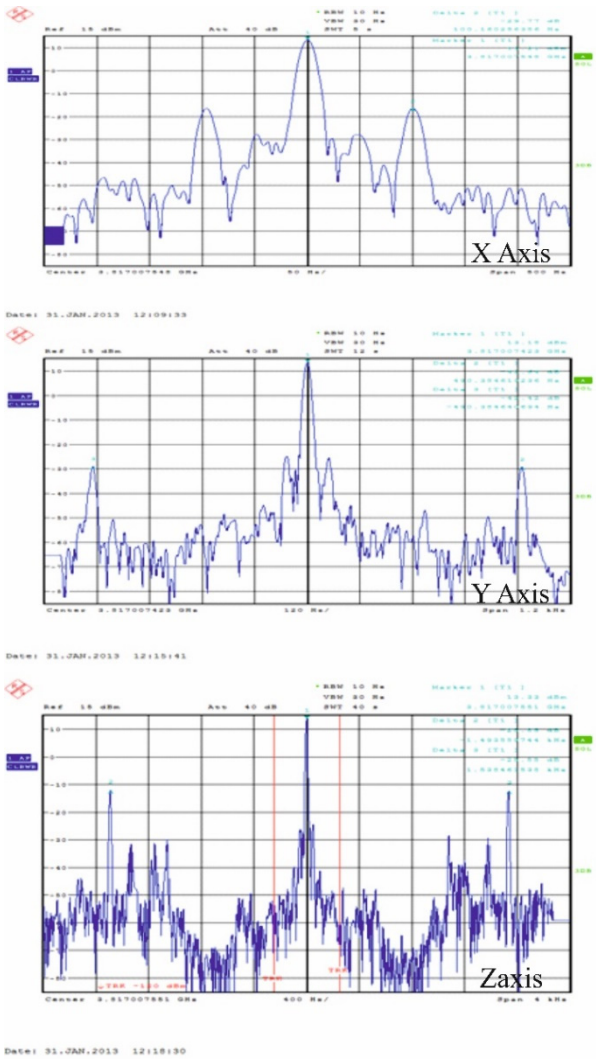

Figure A.6: Sideband levels $L(f_v)$ caused by vibration on X axis 100, 500 and 1500 Hz

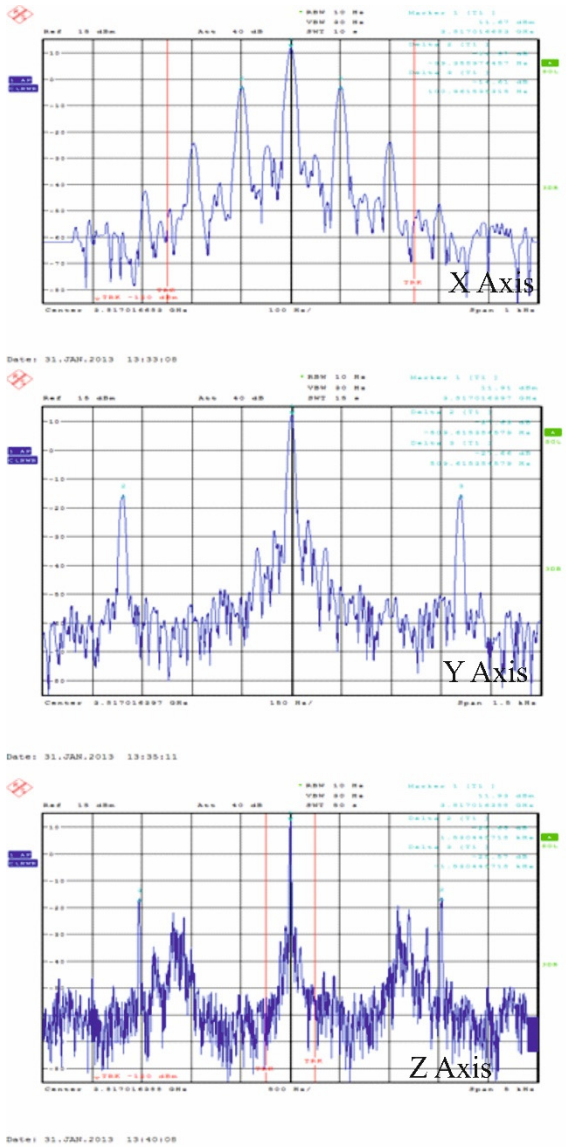

Figure A.7: Sideband levels $L(f_v)$ caused by vibration on Y axis 100, 500 and 1500 Hz.

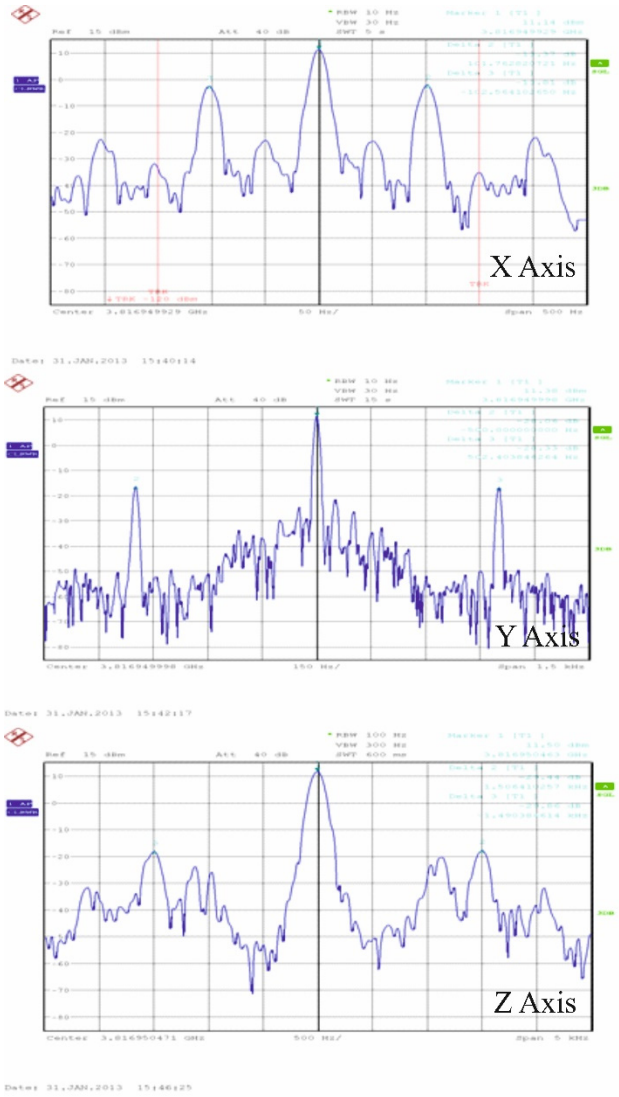

Figure A.8: Sideband levels $L(f_v)$ caused by vibration on Z axis 100, 500 and 1500 Hz.

A.4 Bellows Construction

Bottom Bellows:

The masks for the bellows which were used in order to construct the tuning section are shown in **Figure A.9** and **Figure A.10**.

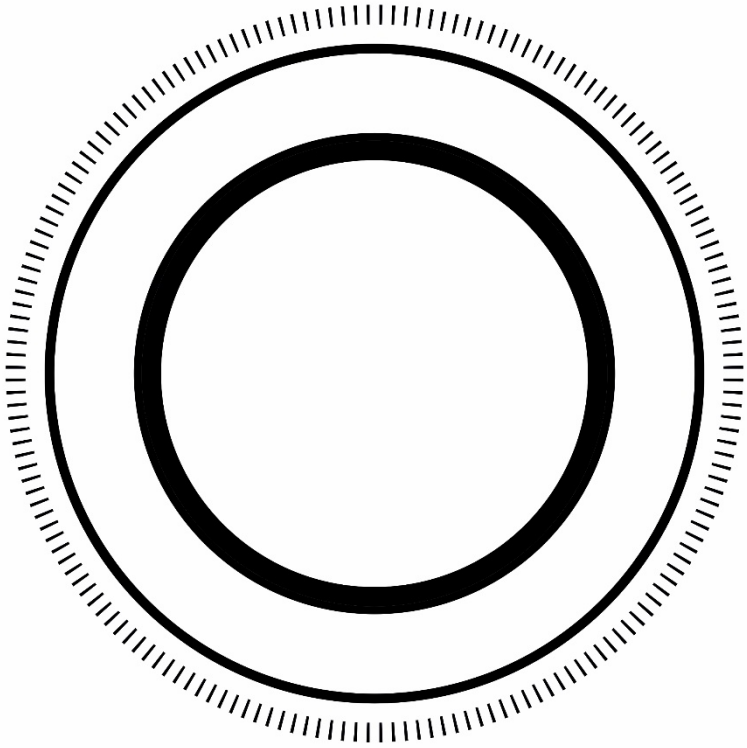

Figure A.9: Mask of the bottom rings used in the construction of the copper bellows.

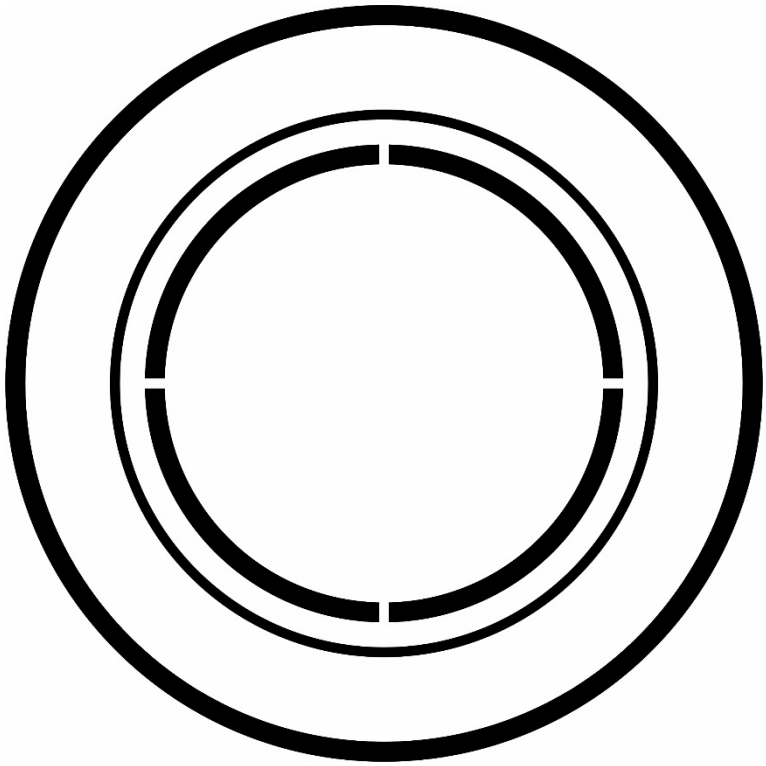

Figure A.10: Mask of the top rings used in the construction of the copper bellows.

BIBLIOGRAPHY

[1] W. P. Robins, "Phase noise in signal sources", Peter Peregrinus Ltd, 1984.

[2] T. Wallin, L. Josefsson and B. Lofter, "Phase noise performance of sapphire microwave oscillators in airborne radar systems," in *GigaHertz2003, Proceedings from the Seventh Symposium*, 2003.

[3] B. Harker and others, "Dynamic range enhancements in Radar Systems," in *2nd EMRS DTC Technical Conference, Edinburgh*, 2005.

[4] T. Wu, X. Tang and F. Xiao, "Reserch on the coherent phase noise of millimeter-wave doppler radar," *Progress In Electromagnetics Research Letters,* vol. 5, pp. 23-34, 2008.

[5] W. P. Robins, Phase noise in signal sources: theory and applications, vol. 9, IET, 1984.

[6] C. McNeilage, J. Searls, E. Ivanov, P. Stockwell, D. Green and M. Mossamaparast, "A review of sapphire whispering gallery-mode oscillators including technical progress and *future potential of the technology,"* in Frequency Control Symposium and Exposition*, 2004. Proceedings of the 2004 IEEE International*, 2004.

[7] U. L. Rohde, A. K. Poddar and G. Bock, The design of modern microwave oscillators for wireless applications: theory *and optimization, John Wiley \& Sons,* 2005.

[8] J. R. *Vig and T. R. Meeker, "The aging of bulk* acoustic wave resonators, filters and oscillators,*" in Frequency Control, 1991., Proceedings of the 45th Annual* Symposium on, 1991.

[9] E. Rubiola, Phase noise and frequency stability in oscillators Cambridge University Press*, November*, 2008.

[10] D. Leeson, "A simple model of feedback oscillator noise spectrum," Proceedings of the *IEEE,* vol. 54, no. 2, pp. 329-330, Feb 1966.

[11] J. Everard, Fundamentals of RF Circuit Design with Low Noise Oscillators, Wiley-Blackwell, 2000.

[12] R. J. Cameron, C. M. Kudsia and *R. R. Mansour,* Microwave filters for communication systems, Wiley-Interscience, 2007.

[13] R. Mansour, "High-Q tunable dielectric resonator filters," Microwave Magazine, IEEE, vol. 10, no. 6, pp. 84-98, Oct 2009.

[14] S. Bale, D. Adamson, B. Wakley and J. Everard, "Cross correlation residual phase noise measurements *using two HP3048A systems and a PC based dual channel* FFT spectrum analyser," in EFTF-2010 24th European Frequency and *Time Forum, 2010.*

[15] S. Bale and J. Everard, "High-Q X-band distributed Bragg resonator utilizing an aperiodic alumina plate *arrangement," Ultrasonics, Ferroelectrics, and* Frequency Control, IEEE Transactions on, vol. 57, no. 1, pp. 66-73, Jan 2010.

[16] F. Hooge, T. Kleinpenning and L. Vandamme, "Experimental studies *on 1/f noise,*" Reports on progress in Physics, vol. 44, no. 5, p. 479, 1981.

[17] A. Van Der Ziel, "Thermal noise at high frequencies," Journal of Applied Physics, vol. 21, no. 5, pp. 399-401, 1950.

[18] P. J. Fish, Electronic noise and low noise design, Macmillan Press, 1993.

[19] K. Theodoropoulos, "Residual phase noise modelling of silicon bipolar amplifiers and ultra low phase noise *ceramic dielectric resonator oscillators,*" 2009.

[20] M. Weissman, "1 f noise and other slow, nonexponential kinetics in condensed matter," Reviews of modern *physics, vol. 60, no. 2, p. 537, 1988.*

[21] A. Hati, C. Nelson and D. Howe, "Vibration-induced PM and AM *noise in microwave components," Ultrasonics, Ferroelectrics, and Frequency* Control, IEEE Transactions on, vol. 56, no. 10, pp. 2050-2059, October 2009.

[22] R. Filler, "The acceleration sensitivity of quartz crystal oscillators: a review," Ultrasonics, Ferroelectrics, and Frequency *Control, IEEE Transactions on, vol. 35, no. 3, pp. 297-305, May 1988.*

[23] M. Driscoll and J. Donovan, "Vibration-Induced Phase Noise: It Isn't Just About the Oscillator," in Frequency Control Symposium, 2007 *Joint with the 21st European Frequency and Time Forum. IEEE International, 2007.*

[24] A. Hati, C. Nelson and D. Howe, Vibration-induced PM Noise in Oscillators and its Suppression, INTECH Open Access Publisher, 2009.

[25] P. Stockwell, C. McNeilage, M. Mossammaparast, D. *Green and J. Searls, "3-axis vibration performance* of a compact sapphire microwave oscillator," in Frequency Control Symposium *and PDA Exhibition, 2001. Proceedings of the 2001 IEEE International, 2001.*

[26] H. Packard, "Phase noise characterization of microwave oscillators," product note 11729C-2 (Hewlett Packard, 1985), 1984.

[27] G. Cibiel, L. Escotte and O. Llopis, "A *study of the correlation between high-frequency noise and phase noise* in low-noise silicon-based transistors," Microwave *Theory and Techniques, IEEE Transactions on,* vol. 52, no. 1, pp. 183-190, Jan 2004.

[28] W. F. Walls, "Cross-correlation phase noise measurements," in Frequency *Control Symposium, 1992. 46th., Proceedings of the 1992* IEEE, 1992.

[29] E. Rubiola and F. Vernotte, "The cross-spectrum experimental method," arXiv preprint arXiv:*1003.0113,* 2010.

[30] J. Everard and K. Theodoropoulos, "Ultra-Low Phase Noise Ceramic based Dielectric Resonator Oscillators," in International Frequency Control Symposium and Exposition, 2006 IEEE, 2006.

[31] O. Llopis, G. Cibiel, Y. Kersale, M. Regis, M. Chaubet and V. Giordano, "Ultra low phase noise sapphire-SiGe HBT oscillator," Microwave and Wireless Components *Letters, IEEE,* vol. 12, no. 5, pp. 157-159, May 2002.

[32] G. Cibiel, M. Regis, O. Llopis, A. Rennane, L. Bary, R. Plana, Y. *Kersale and V. Giordano, "Optimization of an* ultra low-phase noise sapphire-SiGe HBT oscillator using nonlinear CAD," Ultrasonics*, Ferroelectrics, and Frequency Control, IEEE Transactions on,* vol. 51, no. 1, pp. 33-41, Jan 2004.

[33] L. Zhou, "Low Noise Dielectric Resonator Oscillators," 2004.

[34] M. Sallin, L. Zhou, C. Broomfield and J. Everard, "Broad tuning ultra low noise DROs at 10 GHZ utilising ceramic based resonators," in *Frequency Control Symposium and PDA Exhibition Jointly with the 17th European Frequency and Time Forum, 2003. Proceedings of the 2003 IEEE International*, 2003.

[35] S. J. Bale, " "Ultra High Q Resonaotrs and Very Low phase noise measurement systems for low noise oscilaltors"," *April 2012.*

[36] J. K. Everard and C. D. Broomfield, "Reduced transposed flicker noise in microwave oscillators using GaAs-based feedforward amplifiers," Ultrasonics, Ferroelectrics, *and Frequency Control, IEEE Transactions on, vol. 54, no.* 6, pp. 1108-1117, 2007.

[37] E. Ferre-Pikal, F. Walls and C. Nelson, "Design criteria for BJT amplifiers with low 1/f AM and PM noise," in Frequency Control Symposium, *1995. 49th., Proceedings of the 1995 IEEE International, 1995.*

[38] D. M. Pozar, Microwave engineering, John Wiley \& Sons, 2009.

[39] H. Packard and S. Rosa, "Fundamentals of RF and Microwave Noise Figure Measurements," *Appl.* Note, pp. 57-1, 1983.

[40] D. K. a. P. Guillon, "Dielectric resonators,", Artech house, 1986.

[41] K. Cheng and J. Everard, "Noise performance degradation in feedback oscillators with nonzero phase error," Microwave and Optical Technology Letters, vol. 4, no. 2, pp. 64-66, 1991.

[42] K. Miyaguchi, M. Hieda, K. Nakahara, H. Kurusu, M. Nii, M. Kasahara, T. Takagi and S. Urasaki, "An ultra-broad-band reflection-type phase-shifter

MMIC with series and *parallel* LC circuits," *Microwave Theory and Techniques, IEEE Transactions on,* vol. 49, no. 12, pp. 2446-2452, 2001.

[43] C.-S. Lin, S.-F. Chang, C.-C. Chang and Y.-H. Shu, "Design of a reflection-type *phase shifter with wide relative phase shift* and constant insertion loss," Microwave Theory and Techniques, IEEE Transactions on, vol. 55, no. 9, pp. 1862-1868, 2007.

[44] A. Keerti, J. Xiang and A.-V. Pham, "High power linearized RF phase shifter using anti-series diodes," Microwave and Wireless Components Letters, IEEE, vol. 16, no. 4, pp. 200-202, April 2006.

[45] J. Everard, "Low Phase Noise Ceramic Resonator Oscillators," in European Frequency and Time Forum (EFTF), Toulouse France,, April,. 2008.

[46] E. F. a. R.A.Zakarevicius, "Microwave Engineering using Microstrip Circuits", Prentice Hall, 1990.

[47] [Online]. Available: http://www.analog.com/media/en/technical-documentation/data-sheets/ADXL103_203.pdf. [Accessed 16 09 2015].

[48] [Online]. Available: https://www.rogerscorp.com/documents/722/acs/RO3000-Laminate-Data-Sheet-RO3003-RO3006-RO3010.pdf. [Accessed 03 09 2015].

[49] [Online]. Available: https://www.rogerscorp.com/documents/726/acm/RO4000-Laminates---Data-sheet.pdf. [Accessed 03 09 2015].

[50] F. Giannini and G. Leuzzi, Nonlinear Microwave Circuit Design, Wiley Online Library, 2004.

[51] A. Suarez and R. Melville, "Simulation-assisted design and analysis of varactor-based frequency multipliers and dividers," Microwave Theory and Techniques, *IEEE Transactions on*, vol. 54, no. 3, pp. 1166-1179, March 2006.

[52] [Online]. Available: http://ams.aeroflex.com/weinschel/pdfiles/wmod980.pdf. [Accessed 15 09 2015].

[53] H. Packard, HP 3048A phase noise measurement system reference manual, 1989.

[54] R. Boudot and E. Rubiola, "Phase noise in RF and microwave amplifiers," Ultrasonics, Ferroelectrics, and Frequency Control, IEEE Transactions on, vol. 59, no. 12, pp. 2613-2624, Dec 2012.

[55] C. A. Flory and R. C. Taber, "High performance distributed Bragg reflector microwave resonator," *Ultrasonics, Ferroelectrics, and Frequency Control, IEEE Transactions on,* vol. 44, no. 2, pp. 486-495, March 1997.

[56] C. J. Maggiore, A. M. Clogston, G. Spalek, W. C. Sailor and F. M. Mueller, "Low loss microwave cavity using layered dielectric materials," *Applied Physics Letters,* vol. 64, no. 11, pp. 1451-1453, 1994.

[57] C. A. Flory and H. Ko, "Microwave oscillators incorporating high performance distributed Bragg reflector microwave resonators," *Ultrasonics, Ferroelectrics, and Frequency Control, IEEE Transactions on,* vol. 45, no. 3, pp. 824-829, May 1998.

[58] J. Krupka, A. Cwikla, M. Mrozowski, R. Clarke and M. Tobar, "High Q-factor microwave Fabry-Perot resonator with distributed Bragg reflectors," *Ultrasonics, Ferroelectrics, and Frequency Control, IEEE Transactions on,* vol. 52, no. 9, pp. 1443-1451, Sept 2005.

[59] J. Krupka, M. Tobar, J. Hartnett, D. Cros and J.-M. le Floch, "Extremely high-Q factor dielectric resonators for millimeter-wave applications," *Microwave Theory and Techniques, IEEE Transactions on,* vol. 53, no. 2, pp. 702-712, Feb 2005.

[60] J. Breeze, J. Krupka and N. M. Alford, "Enhanced quality factors in aperiodic reflector resonators," *Applied Physics Letters,* vol. 91, no. 15, pp. -, 2007.

[61] J. Breeze, M. Oxborrow and N. McN Alford, "Better than Bragg: Optimizing the quality factor of resonators with aperiodic dielectric reflectors," *Applied Physics Letters,* vol. 99, no. 11, pp. -, 2011.

[62] A. Tombak, F. Ayguavives, J.-P. Maria, G. Stauf, A. Kingon and A. Mortazawi, "Tunable RF filters using thin film barium strontium titanate

based capacitors," in *Microwave Symposium Digest, 2001 IEEE MTT-S International*, 2001.

[63] M. Tsutsumi and K. Okubo, "On the YIG film filters," in *Microwave Symposium Digest, 1992., IEEE MTT-S International*, 1992.

[64] T.-Y. Yun and K. Chang, "Piezoelectric-transducer-controlled tunable microwave circuits," *Microwave Theory and Techniques, IEEE Transactions on,* vol. 50, no. 5, pp. 1303-1310, May 2002.

[65] H. T. a. Y. I. K. Wakino, "Dielectric resonator device". Patent U.S. Patent 4 692 712, Sept 1987.

[66] P. K. P. e. al., "Tuneable two pole one dielectric resonator," pp. 261-266, 2004.

[67] S.-W. Chen, K. Zaki and R. G. West, "Tunable, temperature-compensated dielectric resonators and filters," *Microwave Theory and Techniques, IEEE Transactions on,* vol. 38, no. 8, pp. 1046-1052, Aug 1990.

[68] C. Wang and W. D. Blair, "Tunable high-Q dielectric loaded resonator and filter," in *Radio and Wireless Conference, 2002. RAWCON 2002. IEEE*, 2002.

[69] H. Joshi, H. H. Sigmarsson, D. Peroulis and W. Chappell, "Highly Loaded Evanescent Cavities for Widely Tunable High-Q Filters," in *Microwave Symposium, 2007. IEEE/MTT-S International*, 2007.

[70] A. Farr, G. Blackie and D. Williams, "Novel Techniques for Electronic Tuning of Dielectric Resonators," in *Microwave Conference, 1983. 13th European*, 1983.

[71] J. Krupka, A. Abramowicz and K. Derzakowski, "Magnetically tunable filters for cellular communication terminals," *Microwave Theory and Techniques, IEEE Transactions on,* vol. 54, no. 6, pp. 2329-2335, June 2006.

[72] B. Virdee, "Effective technique for electronically tuning a dielectric resonator," *Electronics Letters,* vol. 33, no. 4, pp. 301-302, Feb 1997.

[73] B. Virdee, A. Virdee and L. Trinogga, "Novel invasive electronic tuning of dielectric resonators," in *Microwave Symposium Digest, 2003 IEEE MTT-S International*, 2003.

[74] W. Keane, "Narrow-band YIG filters aid wide-open receivers," Microwaves, vol. 17, pp. 50-54, 1978.

[75] Teledyne Microwave, [Online]. Available: http://www.teledynemicrowave.com/images/Brochures/Catalog_TMS%20YIG%20Filter%20Products%200507.pdf. [Accessed 25 11 *2015].*

[76] G. Panaitov, R. Ott and N. Klein, "Dielectric resonator with discrete electromechanical frequency tuning," Microwave Theory and Techniques, IEEE *Transactions on,* vol. 53, no. 11, pp. 3371-3377, Nov 2005.

[77] R. R. Mansour, Realization and Design of High-Q Tunable Filters, IEEE-IMS Workshop on Emerging Applications of RF MEMS, June 2009.

[78] C. Balanis, “Advanced Engineering Electromagnetics,”, Wiley, Ed., pp. pp. 485-488..

[79] V. e. Giordano, "Latest developments in ultra-stable microwave oscillators at Femto-ST Institute," in Frequency and Time Forum (EFTF), 2006 20th European, *2006.*

[80] E. Ivanov, M. Tobar and R. Woode, "Advanced phase noise suppression technique for next generation of ultra *low-noise microwave oscillators," in Frequency Control* Symposium, 1995. 49th., Proceedings of the 1995 IEEE International, 1995.

[81] A. Gupta, D. Howe, C. Nelson, A. Hati, F. Walls and J. Nava, "High-spectral-purity microwave oscillator: design using conventional air-dielectric cavity," in Frequency Control Symposium *and PDA Exhibition Jointly with* the 17th *European Frequency and Time Forum, 2003. Proceedings of the 2003 IEEE International*, 2003.

[82] M. Tobar, E. Ivanov, R. Woode and J. Searls, "Low noise microwave *oscillators based on high-Q temperature stabilized sapphire resonators,*" in Frequency

Control Symposium, 1994. 48th., Proceedings of the *1994 IEEE International*, 1994.

[83] E. Ivanov, M. Tobar and R. Woode, "Ultra-low-noise microwave oscillator with advanced phase noise suppression system," Microwave and Guided Wave Letters, IEEE*, vol. 6, no. 9, pp. 312-314, Sep 1996.*

[84] R. Boudot, S. Gribaldo, Y. Gruson, N. Bazin, E. Rubiola, O. Llopis and V. Giordano, "Development of *Ultra Low Phase Noise X-Band Oscillators*," in *International Frequency Control Symposium and Exposition, 2006 IEEE*, 2006.

[85] E. Ivanov and M. Tobar, "Low phase-noise microwave oscillators with interferometric signal processing," Microwave Theory and Techniques, IEEE Transactions on, vol. 54, no. 8, pp. 3284-3294, Aug 2006.

[86] R. Woode, M. Tobar and E. Ivanov, "An ultra-low noise microwave oscillator based on a high-Q liquid nitrogen cooled sapphire resonator," in Frequency Control Symposium, 1995. 49th., Proceedings of the 1995 IEEE *International*, 1995.

[87] M. Aramburo, E. Ferre-Pikal, F. Walls and H. Ascarrunz, "Comparison of 1/f PM noise in commercial amplifiers," in Frequency Control Symposium, 1997., Proceedings of the 1997 IEEE International, 1997.

[88] Piconics, [Online]. Available: 2015. [Online]. Available: http://www.piconics.com/wp-content/uploads/2012/05/A-Broadband-Microwave-Choke.pdf. [Accessed: 27- Oct- 2015].. [Accessed 27 10 2015].